

NORTHWESTERN UNIVERSITY

Airflow Sensing in the Vibrissal System:
Behavioral, Mechanical, and Neural Investigations

A DISSERTATION

SUBMITTED TO THE GRADUATE SCHOOL
IN PARTIAL FULFILLMENT OF THE REQUIREMENTS

for the degree

DOCTOR OF PHILOSOPHY

Field of Mechanical Engineering

By

Yan S.W. Yu

余炎

EVANSTON, ILLINOIS

December 2017

© Copyright by Yan S.W. Yu 2017

All Rights Reserved

ABSTRACT

Mechanisms for sensing fluid flow are well studied in arthropods and in some aquatic mammals, but we know very little about how terrestrial mammals detect and localize airflow (Chapter 1). In this thesis, I will describe a series of studies in rodents that investigate the behavioral, mechanical, and neural basis for vibrissal (whisker) based sensing of airflow.

First (Chapter 2), my colleagues and I performed experiments to demonstrate that whiskers provide important cues during airflow sensing behavior. Rats trained on a five-alternative forced-choice airflow localization task exhibited significant performance decrements after vibrissal removal. In addition, following vibrissal removal rats deviated more from the straight-line path to the air source, choosing sources further from the correct location. In contrast, vibrissal removal did not disrupt performance of control rats trained to localize a light source.

We next (Chapter 3) analyzed the whisker's mechanical response to airflow in order to reveal the physical cues that could underlie the rat's airflow sensing capability. Mechanical experiments showed that whiskers bend primarily in the direction of the airflow, they vibrate around their deflected position at frequencies near their resonance modes, and their bending and vibration magnitudes both scale with airflow speed. At low airspeed, whiskers vibrate parallel to the airflow direction, but, surprisingly, transition to perpendicular vibration at high airspeed.

Third (Chapter 4), to investigate the neural basis for vibrissal-based airflow sensing, we recorded from trigeminal ganglion (Vg) neurons in anesthetized rats during presentation of an airflow stimulus at different speeds and from different directions. The average firing rate of Vg neurons increases with airflow speed, and depends on airflow direction. Additionally, the firing patterns of Vg neurons are related to the intrinsic vibration modes of the whisker.

Together, these results demonstrate that the rodent vibrissal-trigeminal system, which has a well-established role in tactile detection and texture discrimination, also contributes significantly to airflow sensing and anemotaxis. Lastly (Chapter 5), we compare and contrast the whisker's mechanical response to airflow and touch, and compared the rat whiskers with arthropods flow-sensing hairs and pinniped whiskers, and suggest a potential role for rat whiskers in sensing airflow during olfactory search.

ACKNOWLEDGMENTS

I would like to express my first and sincere gratitude to my advisor, Dr. Mitra Hartmann, who provided support and guidance for this thesis in every aspect. As a scientist, she demonstrated her enthusiasm, depth of knowledge and strong dedication to my thesis projects, as well as many other projects in the lab, which continuously impressed me. As an advisor, she exhibited inspiration, kindness, fairness, and patience, and presented good care for the wellbeing of her students. Besides learning much from her in this thesis, I received her tremendous amount of encouragement and helpful advice in my career development. I am fortunate to work with such a great advisor for the past five years.

I would also like to thank Dr. Neelesh Patankar – my committee member and collaborator of this thesis projects, Dr. Malcolm MacIver – my committee member, and Dr. Venkatesh Gopal – my committee and collaborator of this thesis projects. Thanks for sharing their encouragement, insightful comments and expertise for the improvement of my thesis. I would again thank Dr. Patankar, as well as Dr. Wei Chen, for giving me support in my career development.

My next thanks go to my lab mates in the Sensory and Neural Systems Engineering (SeNSE) group of the Neuroscience and Robotics (NxR) lab: Ian Abraham, Hayley Belli, Chris Bresee, Nicholas Bush, James Ellis, Hannah Emmett, Dr. Matthew Graff, Chase Gunderud, Dr. Jennifer Hobbs, Dr. Lucie Huet, Pravin Kumarappan, Yan Man, Admir Resulaj, Mike Salvato, Dr. Chris Schroeder, Anne Yang, Nadina Zweifel, for their hard work, knowledge sharing and camaraderie. It's been a

great experience to work with a group of intelligent and supportive people. I would like to particularly thank Dr. Graff, Chris Bresee, Nicholas Bush, and Yan Man for their significant collaborative contributions in this thesis.

I thank Dr. H. Philip Zeigler, Dr. Leslie Kay and Dr. Thomas Bozza for their critical comments that improved the behavior work (Chapter 2), and I also thank all the undergraduate and other master's students who assisted in the behavioral project: Hector Castillo, Kristine Werling, Derek Oung. I thank Hayley Belli and Brian Quist for assisting in the mechanical work (Chapter 3), and I thank Pravin Kumarappan for assisting the neural work (Chapter 4).

Last but not the least, I thank my family: my parents and my sisters, for giving me an education, and their continuous, full support of my career. I thank my wife Sunny for standing by my side throughout graduate school. She made tremendous efforts to make my life easier.

This work was financially supported by National Science Foundation awards CRCNS-IIS-1208118, CAREER IOS-0846088 and EFRI-0938007, and National Institutes of Health award R01-NS093585. I would like to thank these funding sources.

This dissertation is dedicated to my beloved wife.

Love is patient, love is kind.

Table of Contents

ABSTRACT.....	3
ACKNOWLEDGMENTS	5
Table of Contents	8
List of Tables	14
List of Figures.....	15
Chapter 1	18
Introduction.....	18
1.1 Motivation.....	18
1.1.1 Arthropod hairs are very sensitive to airflow	18
1.1.2 Pinniped use their whiskers to sense water wakes.....	19
1.1.3 Sensing airflow is important to olfactory search	20
1.2 Background.....	20
1.2.1 Rat whisker array	21
1.2.2 Rat whisker sensory pathway.....	22
1.3 Approach and Contribution.....	24
1.3.1 Do rats use their whiskers to sense airflow?.....	24
1.3.2 What mechanical information can rat whiskers provide about airflow?	25
1.3.3 What are the activities of primary sensory neurons in the vibrissotrigeminal system in response to airflow?	26
1.3.4 Conclusions, review and future work	26

Chapter 2	28
Whiskers Aid Sensing Airflow in Rats.....	28
2.1 Abstract.....	28
2.2 Introduction.....	28
2.3 Materials and Methods.....	30
2.3.1 Experimental setup.....	30
2.3.2 Behavioral shaping.....	33
2.3.3 Reward criteria.....	35
2.3.4 Video recording and rat tracking	38
2.3.5 Average deviation	39
2.3.6 Airflow maps	39
2.3.7 Localization threshold experiment.....	40
2.4 Results.....	42
2.4.1 Performance dropped significantly after trimming whiskers.....	42
2.4.2 Rats with higher airspeed threshold exhibited higher accuracy decrement.....	45
2.4.3 Rats deviated more for the incorrect trials after trimming whiskers	46
2.5 Summary	48
Chapter 3	50
Mechanical Responses of Rat Whisker to Airflow.....	50
3.1 Abstract.....	50
3.2 Introduction.....	51
3.3 Materials and Methods.....	52

	10
3.3.1 Experimental setup.....	53
3.3.2 Orientation of the whisker relative to the airflow and quantification of airflow speed	54
3.3.3 Tracking the whisker’s three dimensional shape	56
3.3.4 Quantifying whisker mass, length, diameter, volume, density, and taper	58
3.3.5 Quantifying bending direction and bending magnitude.....	58
3.3.6 Quantifying vibration frequency	61
3.3.7 Quantifying vibration magnitude.....	63
3.3.8 Quantifying vibration direction.....	63
3.4 Results.....	65
3.4.1 The whisker primarily bends in the direction of the airflow and oscillates about that new position	65
3.4.2 Bending direction is independent of airflow speed and orientation of the whisker relative to the airflow	67
3.4.3 Bending magnitude increases along the whisker and depends on airflow speed, orientation, and whisker geometry.....	69
3.4.4 The whisker vibrates at frequencies correlated with its resonance modes	72
3.4.5 Computing mechanical responses to airflow across the entire vibrissal array	76
3.4.6 The effect of head pitch and whisking motions on the response of vibrissae across the array	80

3.4.7	Vibration magnitude increases along the whisker length and depends strongly on airflow speed and the ratio of whisker's arc length to its base diameter, but only weakly on the whisker's orientation relative to airflow.	84
3.4.8	The vibration magnitude scales linearly with the bending magnitude.	88
3.4.9	At low airspeed, whiskers vibrate parallel to the airflow direction, transitioning to perpendicular vibration at high airspeed.	89
3.5	Summary	92
Chapter 4	94
Responses of Primary Sensory Neurons in the Vibrissotrigeminal System to Airflow		94
4.1	Abstract	94
4.2	Introduction.....	95
4.3	Materials and Methods.....	96
4.3.1	Surgical procedures.....	96
4.3.2	Airflow stimulation.....	97
4.3.2	Airflow stimulus calibration	98
4.3.4	Quantifying whiskers' resonances	100
4.4	Results.....	101
4.4.1	Neurons adapt over the course of a sustained airflow stimulus.....	101
4.4.2	All neurons increase firing rate with airspeed	104
4.4.3	Firing rate depends on airflow direction.....	105
4.4.4	Single unit firing periodicities are close to whiskers' resonances.	107

	12
4.4.5 A toy model of the mechanical stimulus: the change of vibration direction with airspeed adds complexity into the coding mechanism of Vg neurons.....	109
4.5 Summary	111
Chapter 5	114
Conclusions, review and future work.....	114
5.1 The vibrissae are multimodal sensors, responsive to both touch and airflow	114
5.2 The mechanics of rat whiskers in response to airflow <i>versus</i> touch.....	116
5.2.1 The mechanical responses of rat whiskers to airflow	117
5.2.2 The mechanical response of a rat whisker to airflow compared to touch.....	118
5.3 Comparison with tactile and flow-sensing hairs of arthropods	122
5.3.1 Different from bending that occurs in arthropod tactile hairs and rat vibrissae, arthropod flow-sensing hairs rotate as a rigid body in airflow	123
5.3.2 Arthropod hair shaft-socket <i>versus</i> rat vibrissae shaft-follicle	125
5.3.3 Rich mechanical responses give rise to a variety of functions between arthropod flow- sensing hairs and rat vibrissae.....	127
5.4 Comparison of vibrissae in pinniped and rodent	129
5.4.1 Morphology and properties of vibrissae in pinniped <i>versus</i> rodent.....	131
5.4.2 Active touch of vibrissae in pinniped <i>versus</i> rodent.....	134
5.4.3 Fluid flow sensation of vibrissae in pinniped <i>versus</i> rodent.....	136
5.5 Role in olfactory search	139
5.5.1 Sensing airflow aid olfactory search in a patchy odor plume	140
5.5.2 Whisking and sniffing.....	143

	13
5.6 Future work.....	145
References.....	146
Appendices.....	167
Supplemental information for Chapter 2.....	167
Supplemental information for Chapter 3.....	173

List of Tables

Table 3.1 Geometric parameters of the whiskers and values of λ_n used to predict resonant frequencies for the fixed-free conical beam.....	56
Table 5.1 A comparison of the mechanics involved with airflow and touch on the vibrissa.	119
Table 5.2 Comparison of vibrissae in pinniped and rodent	130
Table S2.1 Descriptive statistics for locomotion.	167
Table S2.2 Median values of the performance and deviation data.	168
Table S2.3 Completion criteria for the localization threshold experiment vary by rat.....	169

List of Figures

Figure 1.1 Schematic illustration of rat whisker sensory pathway.	23
Figure 2.1 Rats were trained to localize airflow or light.	31
Figure 2.2 Rats learned to perform the task through a series of behavioral shaping stages.	33
Figure 2.3 Reward delivery was contingent on performance.	37
Figure 2.4 Path length deviation was quantified based on the rat's trajectory.	40
Figure 2.5 Vibrissal removal degrades performance in airflow but not light localization.	44
Figure 2.6 For incorrect trials, vibrissal removal causes rats localizing airflow to deviate more from the straight-line path to an airflow source but not a light source.	47
Figure 2.7 Vibrissal removal does not affect the rats' ability to find a light source.	48
Figure 3.1 The experimental setup allowed airflow speed and the orientation of the vibrissa's intrinsic curvature relative to the airflow to be varied independently.	53
Figure 3.2 Schematic of bending magnitude (θ), quantified as the angular displacement of each node from rest to its position in the presence of airflow.	60
Figure 3.3 A whisker will mostly bend in the direction of airflow, and will exhibit vibration about its new mean position.	66
Figure 3.4 Bending direction does not vary systematically with orientation angle or airflow speed.	68
Figure 3.5 Bending magnitude depends on airflow speed, orientation angle of the whisker, and the whisker's arc-length to base diameter (S/D) ratio.	70
Figure 3.6 The vibration frequencies of a whisker are correlated with its resonance modes.	75

Figure 3.7 Parameters used to calculate bending magnitude and vibration frequency in response to airflow.	76
Figure 3.8 Bending magnitude and vibration frequency in response to airflow predicted across the full array of whiskers.	79
Figure 3.9 The effect of head pitch and whisking motions on the bending magnitude of vibrissae across the array.	82
Figure 3.10 Vibration magnitude varies with airspeed and whisker geometry, but only weakly on the orientation of the whisker relative to airflow.	86
Figure 3.11 Vibration magnitude scales with bending magnitude.	88
Figure 3.12 Vibration direction tends to be parallel with the airflow direction at low airspeed, and perpendicular to the airflow direction at high airspeed.	91
Figure 3.13 Mechanics of whiskers in airflow represent airflow information.	93
Figure 4.1 Airflow stimulus calibration.	99
Figure 4.2 Firing rates of Vg neurons during presentation of sustained airflow stimuli.	102
Figure 4.3 Firing rate increases with airspeed.	104
Figure 4.4 Firing rate changes with airflow direction.	106
Figure 4.5 Neurons' firing periodicities correspond to whiskers' resonances.	107
Figure 4.6 The simplified component forces acting on mechanoreceptors in the whisker follicle at different airspeeds.	111
Figure 4.7 Relationships between the whisker's mechanical response, the physical parameters of airflow, and the responses of primary sensory neurons in the trigeminal ganglion.	112
Figure 5.1 The mechanics of rat whiskers in response to airflow.	120

Figure 5.2 Spider flow-sensing hair and tactile hair.....	124
Figure 5.3 Undulated shape of vibrissae suppresses vortices.....	129
Figure 5.4 Photograph of a patchy odor plume in water.....	140
Figure S2.1 Fan speed was adjusted to determine rat localization thresholds.....	170

Chapter 1

Introduction

1.1 Motivation

All animals are immersed in fluids – whether air or water – and oftentimes sensing fluid flow is critical to their survival. Three different behavioral strategies illustrate the importance of sensing fluid flow and motivate this work. Crickets' escape response is particularly supported by their cercal system to detect possible predator-generated air puffs (Jacobs, 1995; Shimozawa et al., 2003; Magal et al., 2006; Dangles et al., 2007). Seals' predation largely relies on their whiskers to sense water wakes created by fishes. (Dehnhardt et al., 1998; Dehnhardt et al., 2001; Marshall et al., 2006). Animals' olfactory search for preys, predators, or conspecifics benefits from their fluid flow sensibility because odor is carried by fluid flow (Murlis et al., 1992; Vickers, 2000; Grasso and Basil, 2002). Although sensing airflow is important for a variety of behaviors, we know little about how terrestrial animals sense airflow.

1.1.1 Arthropod hairs are very sensitive to airflow

Arthropod hairs and rat whiskers are both hair-like structures. A small portion of the hair shaft lies beneath the skin or exoskeleton and the long external part of the hair is immersed in environmental water or air. Arthropod hairs are functionally segregated, with some responding to touch and some responding to fluid flow (Barth, 2004; Dechant et al., 2006). These two types of hairs share a

similar biological structure but exhibit different responses to mechanical stimuli. The flow-sensing hairs respond to particular fluid motion amplitudes and frequencies generated by other animals (Humphrey and Barth, 2007). Two airflow-sensing hairs, trichobothria of wandering spider (*Cupiennius salei*) and cercal filiform hair of cricket (*Gryllus bimaculatus*), have been extensively studied for their morphology, mechanical properties, response characteristics, and innervation pattern (Blickhan and Barth, 1985; Brecht et al., 1997; Albert et al., 2001; Dechant et al., 2001; Barth, 2004; Magal et al., 2006; Humphrey and Barth, 2007; Casas et al., 2010; Bathellier et al., 2012; Guadanucci, 2012). A brief review of arthropod hairs and a comparison with rat vibrissae will be introduced in Section 5.3.

1.1.2 Pinniped use their whiskers to sense water wakes

The finding that pinnipeds use their whiskers to sense water wakes was quite recent. Dehnhardt et al. first found that harbor seals use their whiskers to detect water movements (Dehnhardt et al., 1998), and the lab later demonstrated that the whisker array is the critical sensory organ for harbor seals to track hydrodynamic trails in the absence of vision (Dehnhardt et al., 2001). This function was also tested in California sea lions (Glaser et al., 2011). Because pinniped seek food in deep and murky water, it is broadly recognized that hunting in such an environment with little or no light they must rely heavily on whiskers. Unsurprisingly, investigations also reveal that pinnipeds are able to use their whiskers to distinguish object shape and size by direct touch like rodents (Dehnhardt, 1990, 1994; Dehnhardt and Kaminski, 1995; Dehnhardt and Ducker, 1996). Pinniped whiskers and rodent whiskers share many similarities in their functions, but some key differences

were found in their shape, size, and even movement largely due to their living environment – pinniped stay in water and rodent commonly live on land. Section 5.4 will describe the comparisons of the whiskers in these two species.

1.1.3 Sensing airflow is important to olfactory search

The movement of odor is dominated by fluid flow because odor particles are naturally carried by the fluid medium. Many species use flow to track odor. For example, a cockroach will move upwind when it detects a sex pheromone in the airflow, but move downwind in the absence of this odor (Rust and Bell, 1976); a fruit moth downwind can find an odor source easier with than without airflow (Baker and Kuenen, 1982). In a patchy odor plume, animals including many insects and rats exhibit casting movement – likely exploiting flow information – in olfactory search (Murlis et al., 1992; Vickers, 2000; Reidenbach and Koehl, 2011; van Breugel and Dickinson, 2014).

These examples illustrate that flow sensation closely correlate to olfactory search in many species. On the other hand, recent finding that whisking and sniffing behaviors are synchronized in rats preBötzing nucleus allow us to seek a linkage of olfaction with anemotaxis functioned by nostril and whisker (Moore et al., 2013; Kleinfeld et al., 2016). This possibility will be discussed in Section 5.5.

1.2 Background

Rats are nocturnal rodents with poor visual acuity, and they mainly live on land. They rely heavily on their whiskers to navigate their world. Their whiskers, also called vibrissae, have been studied as direct tactile sensors for over a century (Vincent, 1912). The morphology, mechanics, and neural representation of whiskers in the context of tactile perception and sensorimotor integration have been investigated extensively. This section present some background information about rat whiskers.

1.2.1 Rat whisker array

Rat whiskers are a type of hair, but they have relatively higher stiffness, and are larger in size (diameter and length) than fur or other hairs. They taper from base to tip and have a characteristic intrinsic curvature. There are approximately 30 macrovibrissae protruding from each side of the rat's cheek, called the mystacial pad. A slightly larger number of microvibrissae are found mostly in the rostral region of the animal (Welker, 1964; Brecht et al., 1997). Rat whiskers are organized in five rows (A-E) on each mystacial pad, each row containing five to nine vibrissae (Fig. 1.1A). Other macrovibrissae of rats include the supraorbital, genal, and the mental (whisker trident).

Whiskers are seen in almost all mammals. One of the prominent features of rodents , different from other animals (e.g., carnivores such as cats and dogs), is that they can rhythmically move their whiskers back and forth at frequencies between 5-25 Hz (Welker, 1964; Carvell and Simons, 1990). Rat whiskers are oriented concave forward in the rostral regions of the whisker array,

transitioning to concave downward in the caudal regions. When rats protract their whiskers, these orientations change accordingly.

1.2.2 Rat whisker sensory pathway

Whiskers have no sensors along their length. However, each whisker base is embedded in a structure called a follicle-sinus complex, where many mechanoreceptors densely innervate the whisker base. Each follicle is innervated by the peripheral branches of about 200-300 primary sensory neurons of the trigeminal ganglion (Crissman et al., 1991). In the peripheral nervous system, shown in Fig. 1.1B, a deflected whisker generates mechanical energy, which is transmitted to the nerve terminal surrounding the whisker base in the follicle. This mechanical energy is converted into action potentials (also called “spikes”) by the nerve terminal. These afferent signals travel along the nerve fiber of the trigeminal ganglion neuron and continue along the central branch of this neuron. In the vibrissal central nervous system shown in Fig. 1.1C, signals from the trigeminal ganglion is in turn projected up to the trigeminal nuclei of the brainstem, the thalamic somatosensory nuclei of the thalamus and the barrel region of the primary somatosensory cortex (Diamond et al., 2008).

Importantly, the sensory input from the trigeminal ganglion not only ascends to barrel cortex, but also projects to multiple brainstem feedback loops (Sherman et al., 2013; Bellavance et al., 2017; McElvain et al., 2017). Brainstem loops allow rapid, reflexive control of whisking behavior, while cortical feedback presumably allows the rat voluntary control of whisking. The interplay between

reflexive and voluntary control is another reason why whisker is a good model to study sensorimotor integration and active sensing behaviors.

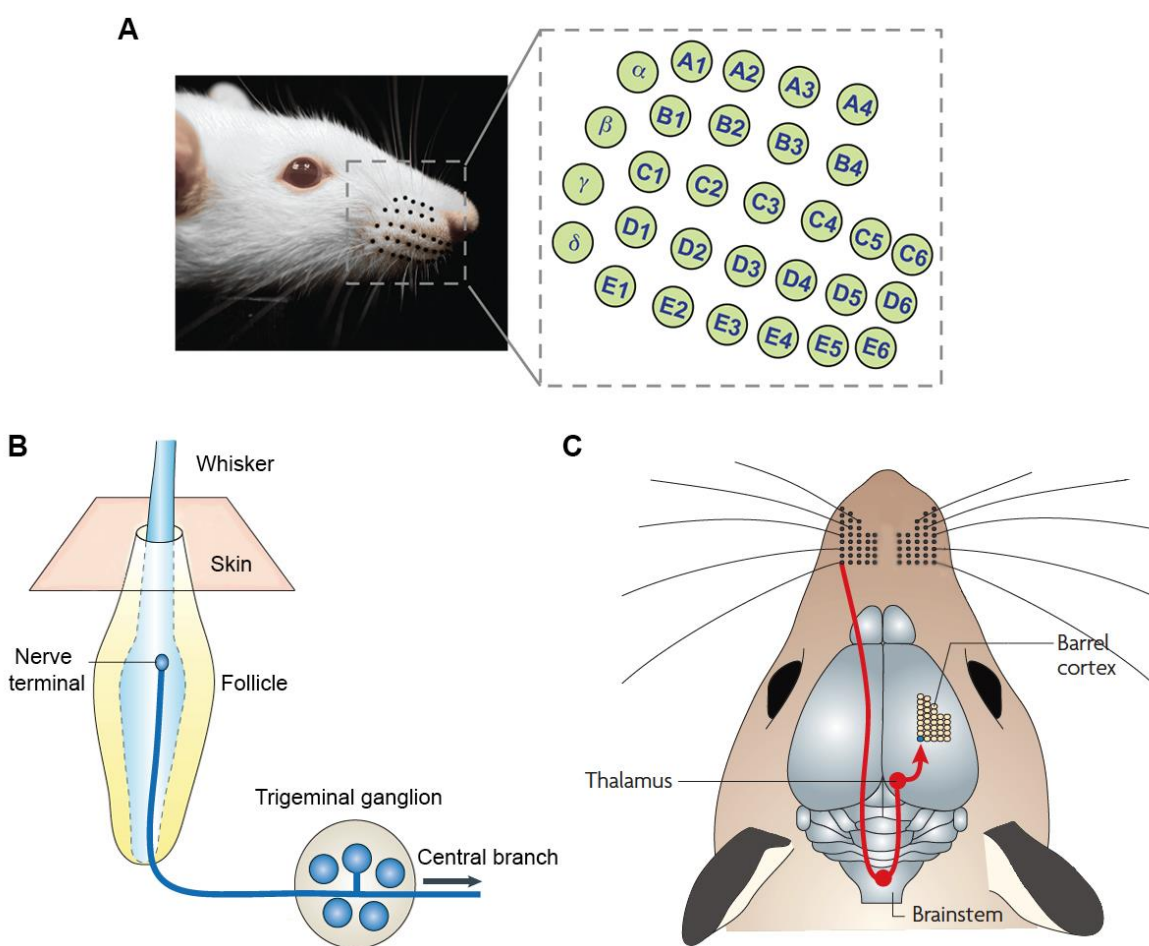


Figure 1.1 Schematic illustration of rat whisker sensory pathway. **(A)** The vibrissae are organized in five rows on each side of the snout, each row containing five to seven (or up to nine) whiskers. **(B)** The peripheral part of the whisker sensory pathway. The base of the whisker in the follicle is innervated by mechanoreceptor terminals. One example terminal is shown. The mechanical stimuli are transduced into an electrical signal by the nerve terminal. The neural signal travels along the trigeminal nerve to the trigeminal nuclei in the brainstem (black arrow). **(C)** The central part of the whisker sensory pathway. The neural signal from the trigeminal ganglion projects to the trigeminal nuclei of the brainstem, the thalamic somatosensory nuclei of the thalamus, and the barrel cortex of the primary somatosensory cortex. Axons of the second-order neurons cross the midline after synapsing in the brainstem (see inset). Subplot (A) is adopted from Yu et al., 2016b. Subplots (B) and (C) are modified from Diamond et al., 2008.

1.3 Approach and Contribution

The sections above have shown that (1) Ethologically, hairs and whisker-like sensors are critical for escape responses (crickets) and wake tracking (seals). (2) From an engineering standpoint, whiskers convey rich mechanical signals. (3) In the field of neuroscience, the vibrissal-trigeminal system is a widely-used model to study sensorimotor integration. Given the broad research significance of whiskers across scientific disciplines, this thesis combined *behavioral, mechanical, and neural* approaches to investigate whether and how whiskers may allow terrestrial mammals to sense airflow.

1.3.1 Do rats use their whiskers to sense airflow?

This thesis begins by first answering the primary question of whether whiskers are used in sensing airflow (Chapter 2). To answer this question, we designed a behavioral experiment to assess how the rat's ability to localize an airflow source changed before and after whisker removal. A group of five rats with intact whiskers were trained to localize an airflow source in a circular arena. A five-alternative forced-choice airflow localization task was used to evaluate their performances. After the rats' performance stabilized for at least 10 consecutive days at ~60% accuracy, their whiskers were cut to a length of ≤ 2 mm and the same task continued for another 10 days. Results indicated that after whisker cutting not only did the rats' accuracies drop significantly (~20% decrement), but also their trajectories deviated more from the straight-line path to the correct airflow source. In contrast, a control group of three rats trained to localized a light source did not

display significant changes either in accuracy or in trajectory deviation. These observations demonstrate that rats do use their whiskers as one of the mechanisms to sense airflow. This discovery presents a new and important function – anemotaxis – for the rat whisker array which has long been neglected.

1.3.2 What mechanical information can rat whiskers provide about airflow?

After confirming that rats use their whiskers during anemotaxis, we were interested in uncovering the mechanism by which the whiskers aided in airflow sensing. As a first step, we wondered what mechanical information rat whiskers could provide about airflow. To investigate the mechanical response of the rat whisker to airflow, as will be described in detail in Chapter 3, we plucked out five whiskers from a rat and clamped them rigidly to a metal post. Airflow provided by a fan was directed towards each whisker and its three-dimensional (3D) shape and position were recorded by two high-speed cameras. The mechanical responses of these whiskers were then quantified.

Results indicated that the whisker primarily bends in the direction of the airflow and vibrates around the deflected position at frequencies close to its resonances. The bending and vibration magnitudes correlate with airspeed. Vibration direction is affected by both airflow direction and airspeed. These results begin to help us construct a “map” linking the mechanics of the whisker and the decomposed airflow stimuli (Fig. 3.14).

1.3.3 What are the activities of primary sensory neurons in the vibrissotrigeminal system in response to airflow?

The second step required to reveal the mechanism for whisker-based airflow sensing involves the nervous system. As will be described in Chapter 4, we recorded from the primary sensory neurons (Vg neurons) in the vibrissotrigeminal system to investigate their activity in the presence of airflow. Activity from eight single neurons from five anesthetized rats were recorded in response to sustained airflow stimulation at three different speeds (1 m/s, 3 m/s and 5 m/s), coming from three different directions. Results indicate that these neurons fire strongly in response to an airflow stimulus. The firing rate clearly increases with airspeed, and the firing periodicity occurs close to the resonances of the whisker that neuron innervates. Moreover, the neural response is affected by airflow direction. Those neurons exhibited direction tuning, in that they responded most strongly (had the highest firing rate) to airflow coming from a particular direction. In 2 of those 8 neurons, the preferred airflow direction changed with airspeed. In another 4 of those neurons, the direction modulation depth weakens as the airspeed increases. These observations work in concert with the mechanical finding that that vibration direction changed with airspeed. We propose a possible neural coding mechanism for airflow information which is strongly dominated by the mechanics of the whisker in the airflow (Fig. 4.8).

1.3.4 Conclusions, review and future work

In Chapter 5, I summarize the contributions of this thesis towards behavioral, mechanical and neural investigations of the rat whisker system's role in sensing airflow. This chapter conceptually compares the mechanical response of rat whiskers to airflow with their response to direct touch. In addition, I review and compare rat whiskers, arthropod hairs, and pinniped whiskers, and suggest a potential role of rat whisker for sensing airflow in olfactory search. At last, I suggest future mechanical, behavioral and neural research directions.

Chapter 2

Whiskers Aid Sensing Airflow in Rats

This chapter was adapted from the publication:

Yu, Y.S.W.*, Graff, M.M.*, Bresee S.C., Man., Y.B. and Hartmann, M.J.Z., Whiskers aid anemotaxis in rats. *Science Advances*, **2**, e1600716 (2016a). *Equal contributions.

2.1 Abstract

Observation of terrestrial mammals suggests they can follow the wind (anemotaxis), but the sensory cues underlying this ability have not been studied. Here we identify a significant contribution to anemotaxis mediated by the whiskers (vibrissae), a modality previously only studied in the context of direct tactile contact. Five rats trained on a five-alternative forced-choice airflow localization task exhibited significant performance decrements after vibrissal removal. In contrast, vibrissal removal did not disrupt performance of control animals trained to localize a light source. Importantly, the performance decrement of individual rats was related to their airspeed threshold for successful localization: animals that found the task more challenging relied more on the vibrissae for localization cues. Following vibrissal removal rats deviated more from the straight-line path to the air source, choosing sources further from the correct location. Results indicate that rats can perform anemotaxis and that whiskers greatly facilitate this ability.

2.2 Introduction

The sensory cues that underlie anemotaxis in terrestrial mammals have not been studied. Studies in multiple other species, however, implicate hair and hair-like appendages in flow sensing behaviors. The antennae of arthropods, the sensory hairs of insects and bats, and the whiskers (vibrissae) of pinnipeds are all used as flow sensors, mediating flight maneuvers (Budick et al., 2007; Sane et al., 2007; Casas and Dangles, 2010; Marshall et al., 2015), escape responses (Casas and Dangles, 2010), wake tracking (Dehnhardt et al., 1998; Dehnhardt et al., 2001), and contributing anemotaxic or rheotaxic information during olfactory search (Rust and Bell, 1976; Baker and Kuenen, 1982; Zimmerfaust et al., 1995; Vickers, 2000; Koehl, 2006; van Breugel and Dickinson, 2014). In analogy to these systems, the vibrissae of the terrestrial mammals would be a prime candidate to serve as flow-sensors.

Two additional lines of evidence suggest a role for vibrissae in flow sensing. First, the mechanical response of a rat vibrissa to airflow contains information about both flow direction and magnitude (Yu et al., 2016b). A vibrissa bends in the direction of airflow, with an average bending amplitude that correlates with airspeed, and then vibrates around its new deflected position (Yu et al., 2016b). Second, whisking and sniffing behaviors are synchronized by activity from the PreBötzing nucleus (Moore et al., 2013), conferring a degree of temporal precision that could align anemotaxic information from the vibrissae with odorant information during olfactory search. Together, these findings suggest that anemotaxic information from the vibrissae may be of high behavioral salience even when multiple anemotaxic cues are available (e.g., from glabrous skin or pelage hairs). We therefore tested the hypothesis that the vibrissae contribute significantly to the ability of rats to localize airflow.

2.3 Materials and Methods

All procedures were approved in advance by Northwestern University's Animal Care and Use Committee.

2.3.1 Experimental setup

Five computer fans (Cooler Master, Blade Master 80) were placed radially around the edge of a 1.83 m (6 ft) diameter circular table (Fig. 2.1A). Each fan was inserted into a 12.70x7.62x7.62 cm (5x3x3 in) enclosure that helped direct the airflow forward. Each fan and enclosure was supported by a free-standing base that was weighted to the floor with heavy iron plates. No part of the fan or the enclosure touched the table. Fan vibrations were barely detectable when the fan enclosure was directly touched with a finger. Although we were not able to directly quantify the magnitude of these tiny vibrations, it is unlikely they influenced the behavior of the rat, as they would have had to have traveled from the fan, through the heavy iron base, through the cement laboratory floor, and back up through the table. The distance between each fan and the entrance door into the arena ranged from 1.41 to 1.56 m (55.5 to 61.25 in), ensuring that airflow speeds at the entrance differed by no more than 0.2 m/s. All airflow speeds were measured using a hot wire anemometer (Omega, model HHF42, resolution = 0.1m/s). The left and right edges of the table, outside of the fence, were removed to ensure that the entire area of the table was visible in the overhead camera frame.

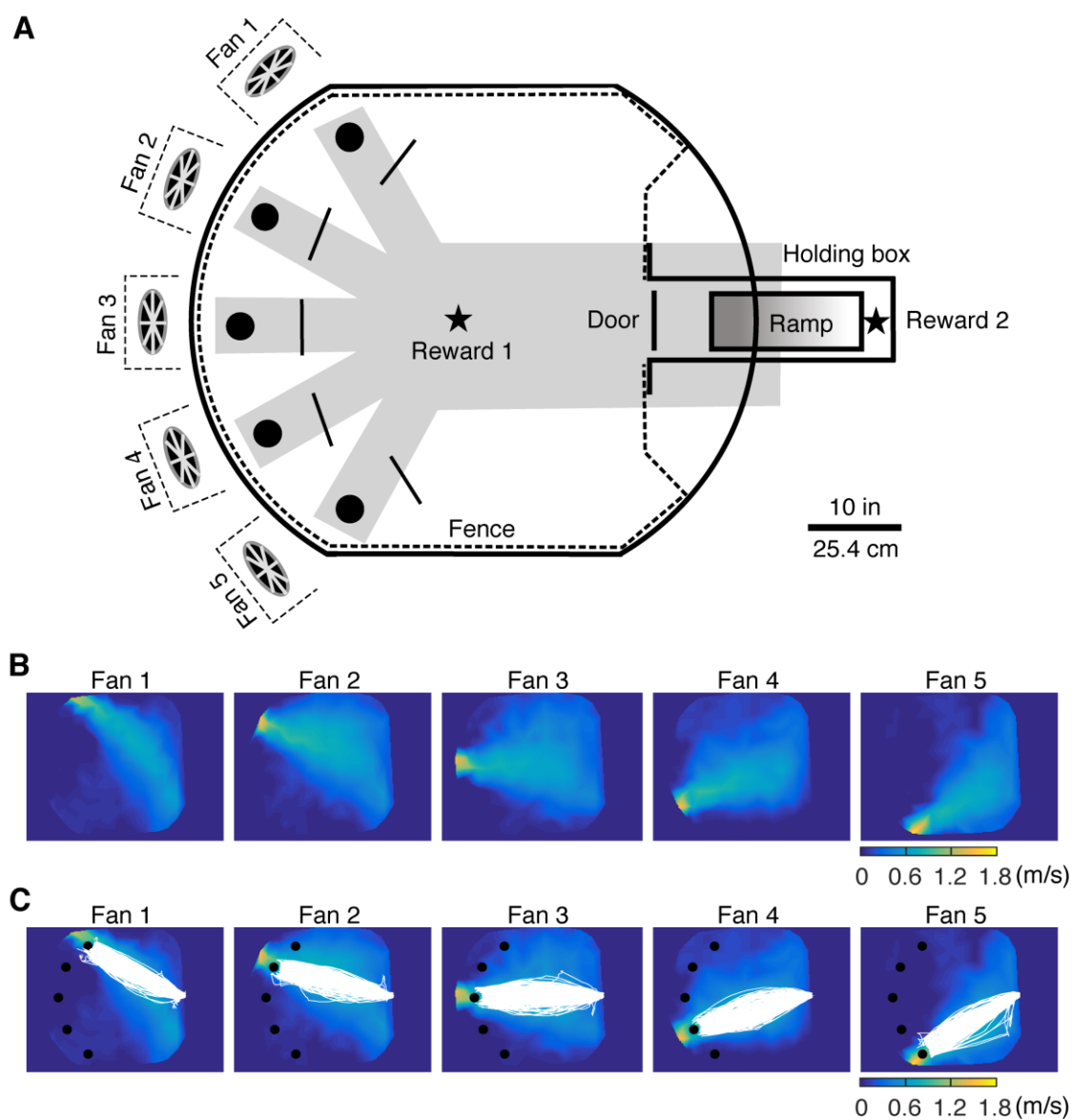


Figure 2.1 Rats were trained to localize airflow or light. **(A)** The arena's entrance door is opposite five fans, placed around the arena circumference. A fence confines the rat. Black solid lines indicate checkpoints. Five holes (black circles) allowed access to tunnels beneath the table (gray shadow) that led to a water reward port (Reward 1, black star), activated only for correct trials. A ramp led back to the holding box where a second reward (Reward 2, black star) was given for correct trials. **(B)** Airspeed colormap shows that the maximum speed lies approximately along the line connecting fans and the entry door. **(C)** Five rats' trajectories (all correct trials before vibrissal removal) superposed on airspeed colormap.

Control stimuli consisted of white light emitting diodes (LEDs) mounted to the top of each of the fan enclosures and directed towards the door. The light intensity of the bulbs was less than 0.1 lux in the center of the table as measured by a light meter (Digi-Sense, Model 20250-00). To ensure against bias towards any particular location each of the five fans or lights was activated the same number of times per training session, and the order of fans was randomized using the C++ “random_shuffle” algorithm (libstdc++, v6.0.19). The randomization was reseeded for each new training session.

We controlled for extraneous cues from audition and vision for all rats. Ambient noise in the room due to building mechanicals was measured to be 50.5 dB (Casella Cel-63X sound meter). The manufacturer’s specifications indicated that the sound emitted from each fan was between 13 and 28 dB; the sound meter did not register a change when a fan was turned on. A masking stimulus was played continuously during training. It consisted of audio recordings from all of the fans with additional bandpass-limited white noise superimposed. The masking stimulus was played back through two speakers beneath the arena (Juster AC-691N), located between fans 1 and 2, and between fans 4 and 5. Amplitude of the masking stimulus was measured to be 67.8 dB. An ultrasound detector (Pettersson D-230) confirmed that the fans did not emit ultrasonic cues.

The experiments were run in a dark room in which a computer monitor behind a curtain was the only ambient visible spectrum light source. Matte black cloth was mounted behind each fan to reduce the contrast between the fan’s blades and the background.

2.3.2 Behavioral shaping

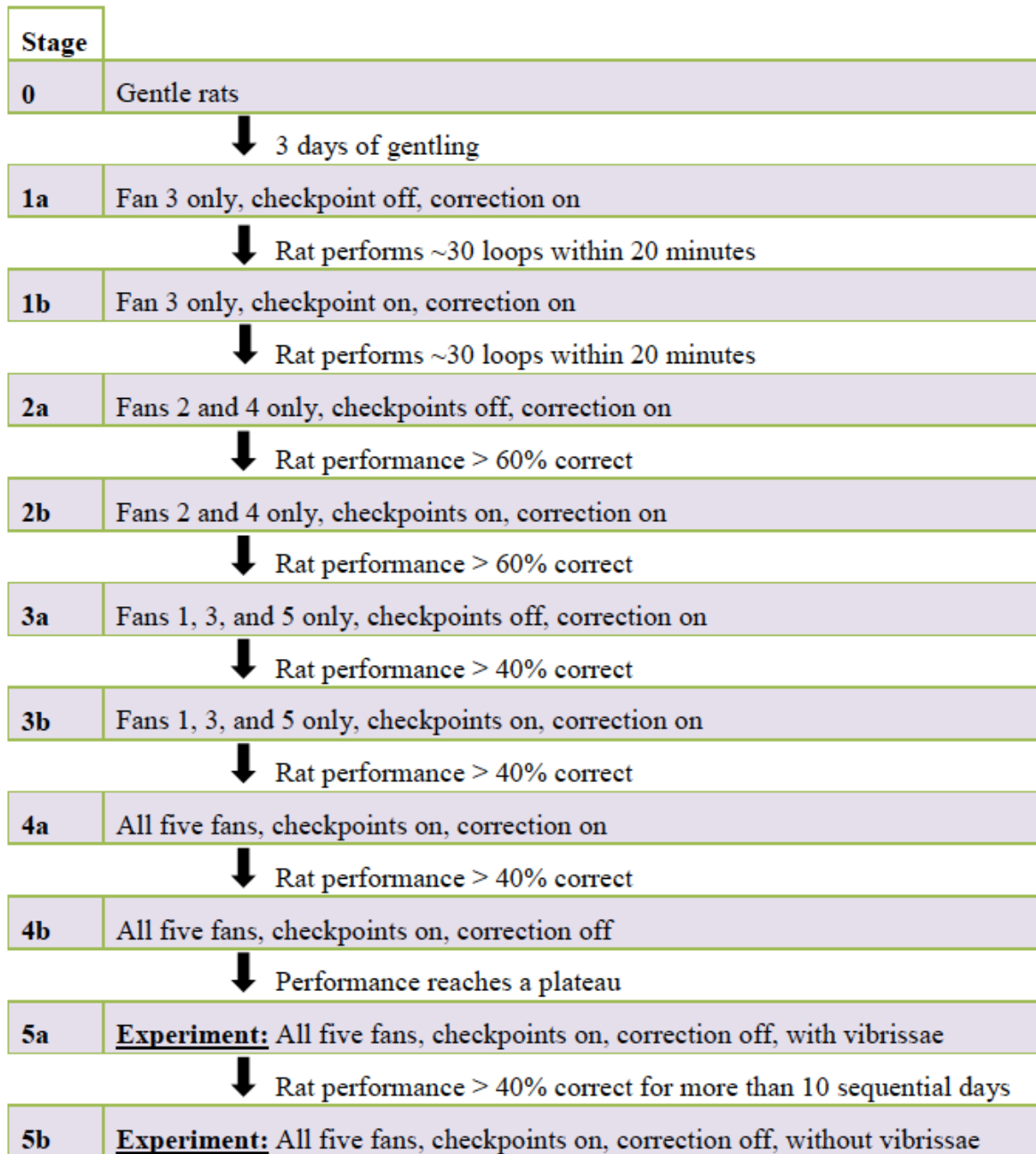


Figure 2.2 Rats learned to perform the task through a series of behavioral shaping stages. Rats were trained in four stages of increasing difficulty. In stages 1 to 4 the number of fans was gradually increased from a single fan to five fans. Fans were added symmetrically about fan 3. Each stage was composed of two sub-stages to adjust the difficulty of the task. The criteria for stage

advancement were adjusted to reflect the difficulty of the training stage. Stage 5a marks the beginning of the experiment and was determined retroactively to begin when the rat performed greater than 40% for 10 consecutive days with an average performance above 55%. In stage 5b vibrissae were cut off and the experiment was performed for an additional 10 days.

Rats were trained five days a week, for three to five months, starting at three months of age. All rats completed 45 to 50 trials per day (usually ~30 min/rat) and the order in which the rats were trained changed each day. The rats were deprived of water for 23 hours prior to training, but received *ad libitum* water two days per week.

Each day of training began with a 5-minute gentling session in which the rat was conditioned to tolerate being held firmly while its vibrissae were brushed with a set of blunt-tipped scissors. This conditioning allowed us to cut off the vibrissae without anesthesia during the original experiment (stage 5b in Fig. 2.2) and during the localization threshold experiment.

Rats were trained to localize airflow emanating from one of five fans. Training consisted of several stages of increasing difficulty, as schematized in Fig. 2.2. During training, a correction procedure was used such that when a trial was completed incorrectly the trial was repeated with the identical stimulus until the rat gave a correct response. In the final stage, the correction procedure was stopped. After rats achieved a success rate above 40% for 10 consecutive days with an average above 55%, all vibrissae (both macrovibrissae and microvibrissae) were trimmed to < 2 mm in length. Macrovibrissae included mystacial, supraorbital, genal, and the mental (whisker trident). Microvibrissae under 2 mm were not trimmed. Vibrissae were re-trimmed every other day to ensure that they never exceeded 2 mm in length.

Nineteen rats were initially trained. Of those, ten were excluded from the experiment during the first stage of training (stage 1a in Fig. 2.2). These ten rats refused ever to traverse the open-field arena, choosing instead to sit within the tunnel system and groom. One rat was excluded in the last stage of training (stage 4a in Fig. 2.2). This rat gradually became lethargic over a period of ~3 weeks, choosing to sit and groom in the tunnel underneath the table. Although her overall performance on the task (both percent correct and locomotor speed during the trial) resembled that of the other rats, training sessions gradually extended to one or two hours due to these extended periods of grooming, and she was therefore excluded from the study. Of the remaining eight rats, five composed the experimental group (localized airflow) and three composed the control group (localized light). A total of 7,217 trials were recorded. 6.7% of the trials were removed from the dataset because the rats were grooming, climbing, following the arena's edge or retreating back into the holding box before completing the trial. A total of 0.6% of all trials were removed due to computer malfunction.

On the third day after trimming the vibrissae of Rat 2 a fire alarm went off after it had performed 26 trials. Only 26 trials were used on that day.

2.3.3 Reward criteria

Reward criteria for training are shown in Fig. 2.3. In order to receive rewards, the rat was required to run towards the operating fan and cross two trigger regions along the way. All triggers were

implemented digitally through images taken by an overhead camera and were not physically observable. The first (checkpoint) set of triggers consisted of five linear regions of interest, 15.24 cm (6 in) wide, located 21.59 cm (8.5in) in front of their corresponding holes. Each trigger line was oriented to be orthogonal to the straight-line path connecting the center of its hole to the entrance of the arena. The second (hole) set of triggers consisted of 11.43 cm (4.5 in) circles surrounding each hole. During training stages 1a, 2a and 3a the checkpoint triggers were turned off to promote a smoother transition between increasingly difficult training stages. The distances between the door and the holes ranged between 93.98 cm (37 in) and 106.68 cm (42 in).

Upon reaching the hole trigger the rat was required to go down one of the 7.62 cm (3 in) diameter holes located in front of the fans leading to a tunnel system beneath the table. The tunnels led to the first reward and provided a path back to the holding box to receive a second reward. To prevent the rat from looping in the opposite direction, one-way doors were installed in each of the five branches of the tunnel system as well as a one-way hatch at the top of the ramp. In the event that a rat did not return to the holding box within a ~1 minute time span, rats were gently guided up the ramp by the trainer.

The first reward was a 0.09 ± 0.02 ml drop of fresh water and was dispensed by a solenoid valve in the center of the chamber beneath the table. The second reward was a 0.1 ± 0.07 ml drop of sucrose solution (85.575 g/L) and was dispensed manually with a pipette at the rear of the holding box (Fig. 2.1A). The purpose of the second reward was to motivate the rat to return to the holding box.

Both rewards were contingent on the rat getting the trial correct. A new trial was started once the rat returned to the holding box. The start of each trial was controlled manually by the trainer.

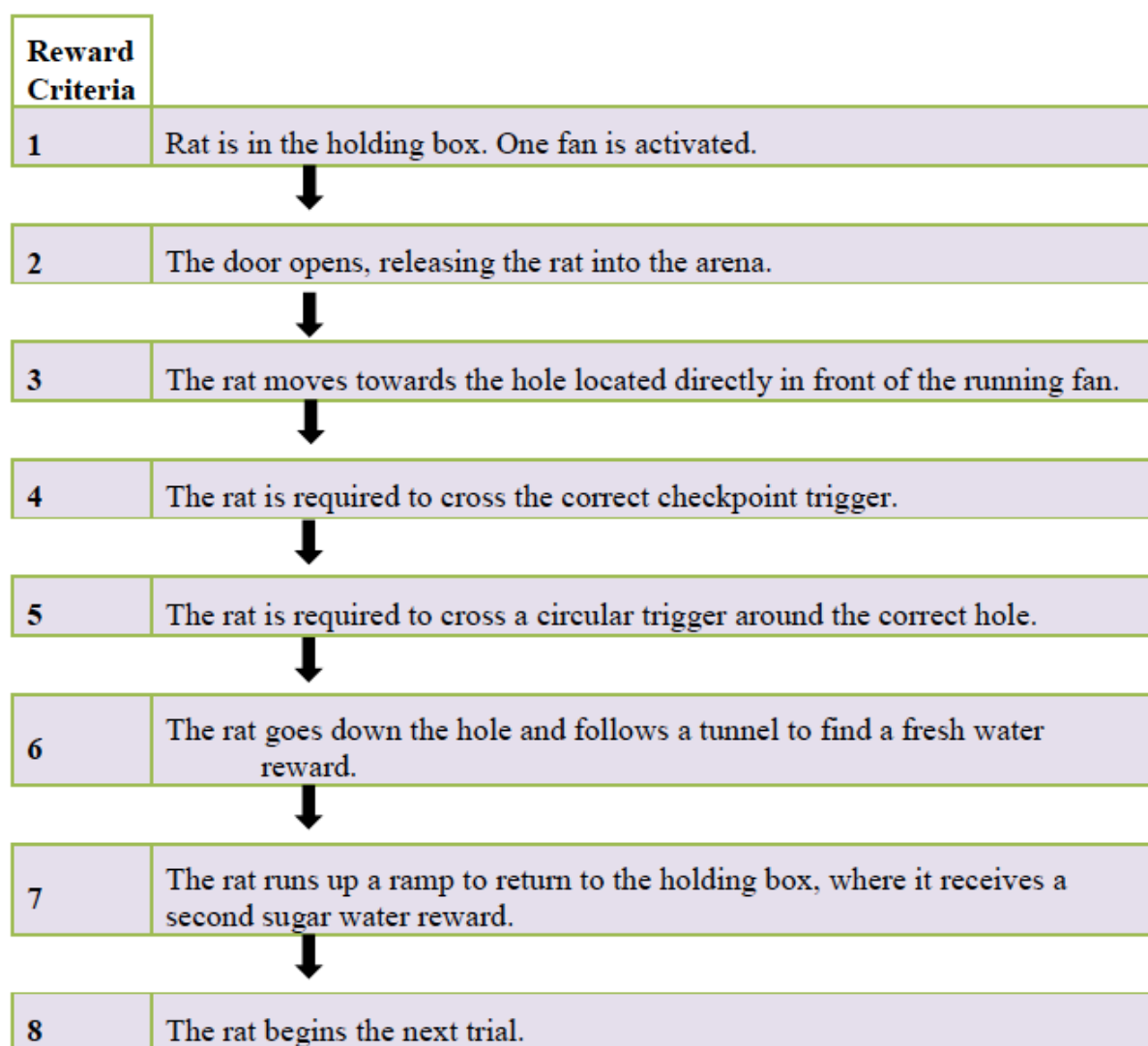


Figure 2.3 Reward delivery was contingent on performance. (1) The rat started in the holding box and one of the five fans was activated. (2) After a ten second delay, the motorized door lifted automatically. (3) The rat left the holding box and ran towards the airflow source. (4) To prevent the rat from making a choice close to the fan, it was required to cross the checkpoint trigger before (5) reaching the hole corresponding to the activated fan. Note that when the rat reached any of the hole triggers, the fan was turned off and the holding box door was shut. In cases when the rat failed (chose either the first or second trigger incorrectly, or both), all rewards were withheld, but the rat was allowed to navigate through the tunnels as normal. (6) Upon the successful completion of

steps 1 - 5 a solenoid valve opened beneath the table, making an audible click and releasing a fresh water reward. The rat travelled down the hole and through a tunnel system to the reward. (7) The rat then traversed a ramp back to the holding box to complete the trial and receive a second sugar water reward. The second reward was contingent upon the rat having received the first reward. (8) The rat started another trial. This process was repeated for a minimum of 45 trials per day per rat. For control rats, fans were replaced with LEDs.

2.3.4 Video recording and rat tracking

An infrared light source (15 W) illuminated the arena from above. Video was recorded at 20 fps at a resolution of 480x640 pixels by a surveillance camera (model: Swann PRO-760) and a video capture card (Pinnacle, AV to USB2 Rev. 1.2A). Custom circuitry and software were developed to monitor the checkpoints as well as to control the actions of the camera, vertical lift door to enter the arena, fans, LEDs, and the reward solenoid. The triggers were implemented by monitoring their respective regions of interest for changes in pixel intensity from the white background. If the intensity within the trigger's region of interest fell below a threshold value, the trigger was activated. Upon reaching a hole trigger the arena door was automatically closed and the fan was turned off. For correct trials the solenoid was automatically activated, producing a clicking sound and alerting the rat of the presence of a reward. The trial number, correct fan number, checkpoint trigger number, hole trigger number and full video for each trial were automatically recorded.

Rat positions were automatically tracked in post-processing using Matlab[®]. The tracking algorithm exploited the contrast between the rat (brown) and arena (white) to measure the position of the rat. An image of the empty arena was used to find and mask out persistently dark regions. Any

remaining dark regions greater than a size threshold represented the rat. The position of the rat was defined as the centroid of the dark region.

2.3.5 Average deviation

The straight-line trajectory is defined as the line that connects the door with the correct hole. The rat's deviation at each point in time is defined as the orthogonal distance between the rat's position and the straight-line trajectory. Intuitively, the average deviation can be thought of by imagining that the rat has taken a trajectory in which its deviation is constant throughout its entire path. The rectangular area enclosed by this hypothetical trajectory is defined by the straight-line trajectory and the average deviation value. It follows that the average deviation is equal to the enclosed area divided by the length of the straight-line path. The average deviation values plotted in Fig. 2.6B were therefore calculated by measuring the enclosed area shown in Fig. 2.4 and dividing by the length of the straight-line path.

2.3.6 Airflow maps

To monitor for changes in airspeed between training days, airspeed measurements were taken at 11 points throughout the arena for each fan for a total of 55 measurements each day. For each fan, the first measurement point was taken at the door, the next five points were taken half way between the door and each hole, and the final five points were taken in front of each hole. Typical fan speeds along the lines connecting the fans to the door were 1.1 ± 0.3 m/s, 0.8 ± 0.2 m/s, and 0.5 ± 0.2

m/s (mean \pm maximum difference) as measured from the door to the hole. We also recorded three days of higher spatial resolution measurements taken at 162 points for each fan, spaced evenly throughout the arena. To produce the color map images for Figs. 2.1 (B and C), 2.4 and 2.6A, and Movie S2.1, small markers were placed at the 162 measurement locations and the overhead camera was used to take a picture of the arena. The positions of the markers were then manually extracted from the image and used to linearly interpolate the airspeed for every pixel location within the arena.

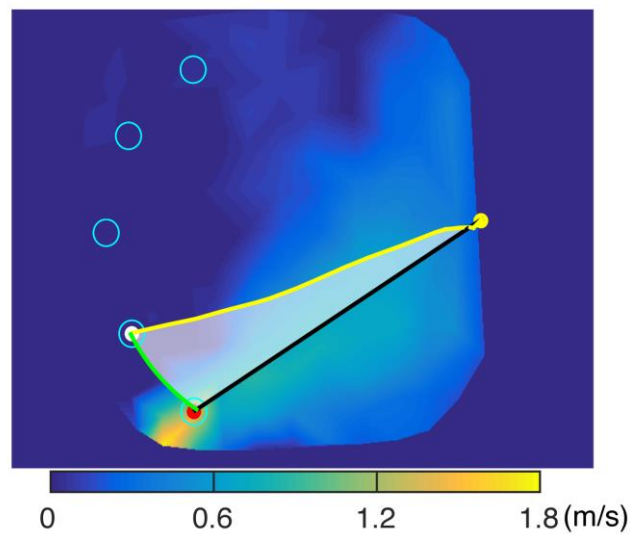


Figure 2.4 Path length deviation was quantified based on the rat's trajectory. The deviation was computed as the area enclosed by the straight-line path from the door to the activated fan (black line connecting the yellow dot to the red dot), the actual trajectory taken by the rat to the incorrect fan (yellow curve connecting yellow dot to white dot), and the arena boundary (green curve), divided by the length of the straight-line path.

2.3.7 Localization threshold experiment

For three of the five rats trained to localize airflow (Rats 1, 2, and 3) a follow-up experiment was performed to investigate the threshold at which the rats were able to localize airflow. In this experiment we used a 2-up/2-down paradigm to alter the magnitude of the airspeed based on the rat's performance. After the rat performed two correct trials the airspeed was lowered, increasing difficulty. Conversely, after performing two incorrect trials the airspeed was raised, decreasing difficulty. For the first six reversals the airspeed was changed in 10% increments. For the next six reversals the airspeed was changed in 2% increments (Fig. 2.5B and Fig. S2.1). Each day, this process was continued until the airspeed was reversed 12 times (12 "reversals") or after ~1.5 hours of testing. The speed of each fan was adjusted via a pulse-width modulation signal (PWM). On average, a 1% change in the duty cycle of the PWM signal resulted in a 0.015 m/s change in airflow speed at the hole. The duty cycle could be adjusted within the range of 1-99%.

Rats 1 and 3 performed the staircase procedure for six days with vibrissae and six days without vibrissae. For several days Rat 2 did not achieve an adequate number of reversals. Therefore it was tested for 10 days before trimming and 10 days after trimming. The subset of six days with the highest number of reversals before and after trimming was used in the threshold analysis. Table S2.3 shows the number of reversals achieved for each rat on each day. To normalize for the variable number of trials that each rat took to achieve convergence, we analyzed percent complete as opposed to trial number. The percentage of maximum fan speed was then resampled using linear interpolation at integer values of percent complete. Means and standard deviations were computed at these integer values.

2.4 Results

We begin by showing that rats trained to localize airflow present a performance (accuracy) decrement after trimming whiskers. Airspeed threshold values were obtained from the threshold experiment and rats with higher airspeed threshold exhibit a larger accuracy decrement in the main experiment. Moreover, rats without whiskers deviated more than with whiskers when rats failed in the task. In contrast, the control group of rats trained to localize light other than airflow neither show a performance decrement, nor deviated more after trimming whiskers.

2.4.1 Performance dropped significantly after trimming whiskers

Five rats (female, Long Evans, ~3 months) were trained to localize airflow emanating from one of five fans placed around the circumference of a circular arena, spaced $\sim 30^\circ$ apart as measured from the arena center (Figs. 2.1A, 2.2 and 2.3). Each day of training included at least 45 trials; only one of the five fans was on during any given trial. On each day the sequence of fans was randomized while ensuring that each fan was on nine times (see Section 2.3 *Materials and Methods* for details). At the start of each trial a door opened to allow the rat to leave a holding box, enter the arena, and localize the airflow source by running towards a hole in front of the fan. Airspeed at the hole was 1.1 ± 0.3 m/s and airspeed at the door was 0.5 ± 0.2 m/s (Fig. 2.1B).

In a preliminary study, we found that rats could circumvent the task by circling around the arena, exploring several fans in turn, and making a decision only when extremely close to the correct fan.

To prevent this behavior, a correct choice required rats first to cross a virtual checkpoint 21.6 cm (8.5 in) in front of the hole (Fig. 2.1A). If the rat both crossed the checkpoint and approached the hole, an audible click signaled the delivery of a water reward from a fluid port beneath the table. To obtain the reward the rat had to go down a hole and follow a tunnel beneath the table to the water port. If the rat performed the trial correctly it received a second reward for running up a ramp from the water port back to the holding box. Another trial began after a ~10 second inter-trial interval.

Because a trial was counted as correct only if the boundary of the hole and the checkpoint were both crossed, all rats tended to follow a nearly straight-line path to the hole in front of the airflow source (Fig. 2.1C). Movie S2.1 shows examples of both correct and incorrect trials.

Upon performing the task for ten consecutive days at a success rate above 55% (where chance = 20%), with no single day lower than 40%, a complete bilateral vibrissotomy was performed and the rats were then tested for an additional ten days. A control group of three rats was trained on the same task, except the fans were replaced with a white light source. The control group underwent the same bilateral vibrissotomy. Careful acclimatization procedures (see Section 2.3 *Materials and Methods* for details) allowed us to cut off (trim) all vibrissae in both groups of animals without anesthesia, using only gentle manual restraint. All vibrissae were trimmed to a length less than 2 mm; this trimming included all macrovibrissae and the longer of the microvibrissae (see Section 2.3 *Materials and Methods* for more detail). We observed no

significant group-wise change in locomotor speed or pausing of the rats after vibrissal trimming.

Descriptive statistics for this analysis are shown in Table S2.1.

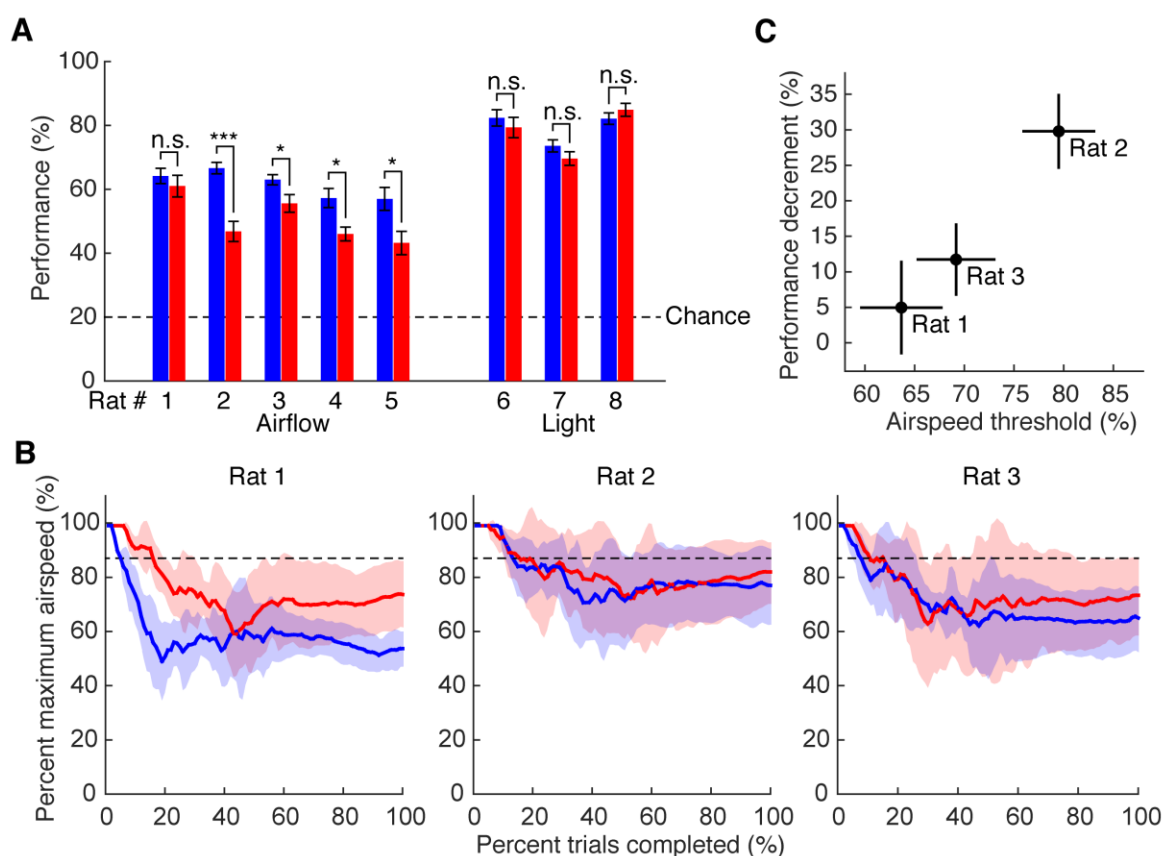


Figure 2.5 Vibrissal removal degrades performance in airflow but not light localization. **(A)** Average (10-day) performance before (blue) and after (red) vibrissal removal for rats trained to localize either airflow or light. Error bars show mean \pm SEM. *** $p < 0.001$, * $p < 0.05$, n.s. $p \geq 0.05$, Wilcoxon rank sum test, median values are reported in Table S2.2. **(B)** Average (6-day) localization threshold before (blue) and after (red) vibrissal removal on the 2-up/2-down experiment. Data show mean \pm SD percent maximum airspeed. Dashed lines indicate the fixed airflow speed used in Fig. 2.5A (87% maximum). **(C)** Average performance decrement (10-day average) with fixed airspeed is related to localization threshold (12-day average). Data points show mean values; vertical lines indicate \pm SEM performance decrement; horizontal lines indicate \pm SEM threshold.

Following vibrissal removal, all rats exhibited a notable decrement (~20%) in their ability to localize the source of the airflow; this effect was statistically significant in four of the five rats (Fig. 2.5A and Table S2.2). In contrast, none of the rats trained to localize the light source showed a significant performance decrement. As expected, all rats could still perform the airflow localization task at levels well above chance (20%) regardless of the presence of vibrissae, confirming that these sensors are not the exclusive modality used for flow sensing.

2.4.2 Rats with higher airspeed threshold exhibited higher accuracy decrement

To investigate the basis for inter-rat performance variability after vibrissal removal we replicated the original experiment while manipulating airspeed. This new experiment determined the localization thresholds of individual rats using a 2-up/2-down staircase paradigm. The vibrissae of three rats were allowed to regrow for one month and rats were then retrained for two weeks on the original experimental task (air speed = 1.1 ± 0.3 m/s at the hole). After two weeks, the threshold experiment started. Each day of training began with the fans running at full speed (1.4 ± 0.3 m/s at the hole); note that full speed is higher than the original experiment. Fan speed was decreased by 10% if the rat completed two trials correctly and increased by 10% following two incorrect trials. After the fan speed was reversed six times the resolution of the speed change was decreased to 2%. On each day, data collection stopped either after a total of 12 reversals (six reversals at 10% and six at 2%) or after ~1.5 hours of testing, when the rat had lost interest in the task (Fig. S2.1).

Comparing the results of the localization threshold experiment across rats (Fig. 2.5B) offers a compelling explanation for the variability in performance decrement. The localization threshold for Rat 1 was lower than the airspeed used during the original experiment, both before and after vibrissal removal. This rat was sufficiently sensitive to airflow that, although vibrissal removal caused a performance decrement, it was not large enough to reach statistical significance. In contrast, the localization thresholds for Rats 2 and 3 more closely bracketed the 1.1 ± 0.3 m/s airspeed used in the original experiment (87% of max); these rats exhibited significant performance reductions with vibrissal removal. Fig. 2.5C illustrates the relationship between performance decrement and localization threshold for these three rats. It shows that rats exhibiting higher accuracy decrement in the main experiments present higher airspeed threshold, which suggests that whisker could play a more important role in sensing lower airspeed compared with other cues.

2.4.3 Rats deviated more for the incorrect trials after trimming whiskers

Complementing the performance decrement, the magnitude of the localization error was also found to increase after vibrissal removal. Although rats' trajectories during correct trials were generally straight-line paths (Fig. 2.1C), their trajectories on incorrect trials deviated from these paths, and this deviation increased after vibrissal removal (Fig. 2.6A). Deviation was quantified as the shortest (i.e., orthogonal) distance from the rat's position to the straight-line trajectory. Average deviation was calculated in a two-step process: we first computed the area enclosed by three curves: the straight-line trajectory to the correct fan, the boundary of the arena, and the rat's actual

trajectory (Fig. 2.4), and then divided the area by the length of the straight-line trajectory. Average deviation thus captures the extent to which the rat's trajectory diverges from the straight-line path to the correct fan; see Section 2.3 *Materials and Methods* for more detail on this metric. Fig. 2.6B shows that on average, deviation from the straight-line path increased 20.4% for all rats trained to localize the airflow source; this effect was significant for all but Rat 1. In contrast, no significant changes in path length deviation were observed for any rats in the control group trained to localize the light source (Figs. 2.6B and 2.7, and Table S2.2).

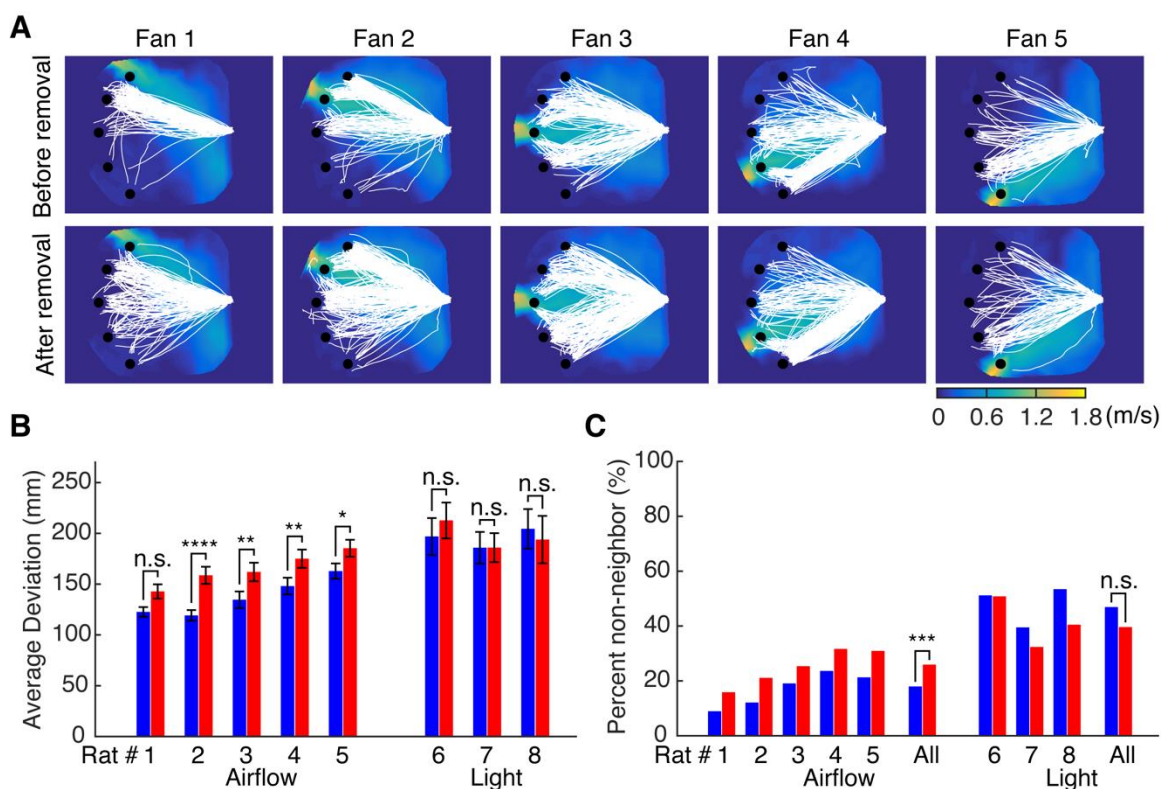


Figure 2.6 For incorrect trials, vibrissal removal causes rats localizing airflow to deviate more from the straight-line path to an airflow source but not a light source. (A) Trajectories of all incorrect trials of five rats trained to localize airflow ten days before vibrissal removal (top row) diverge less than after removal (bottom row). (B) For incorrect trials, deviation of each rat before vibrissal removal (blue) is smaller than after removal (red). Error bars show mean \pm SEM. **** $p < 0.0001$, ** $p < 0.01$, * $p < 0.05$, n.s. $p \geq 0.05$, Wilcoxon rank sum test, median values are reported in Table

S2.2. (C) The percent of incorrect trials for which a non-neighboring fan was chosen before (blue) and after (red) vibrissal removal. *** $p < 0.001$, n.s. $p \geq 0.05$, Yates's corrected chi-square test.

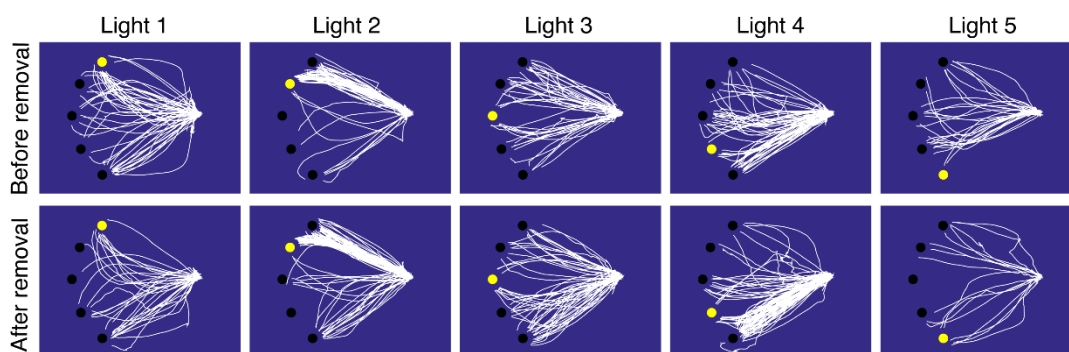


Figure 2.7 Vibrissal removal does not affect the rats' ability to find a light source. Trajectories of all incorrect trials for all three rats trained to localize a light source on the ten days before (top row) and after vibrissal removal (bottom row). Trajectories show equal deviation from the ideal straight-line path before and after vibrissal removal.

The changes in path length deviation shown in Fig. 2.6 (A and B) suggest that rats were choosing fans further away from the correct source of airflow. We confirmed this possibility by computing the percent of incorrect trials in which rats chose either a neighboring (incorrect) source, or a non-neighboring (incorrect) source. This analysis effectively measures the degree of spatial error in the rat's localization choice (Fig. 2.6C). All rats trained to localize the airflow showed an increased tendency to choose non-neighboring fans after vibrissal removal. When pooled, the increase reached significance. In contrast, rats trained to localize the light source showed no consistent change.

2.5 Summary

In this chapter, we answered the question of whether rats use their whiskers to sense airflow. In these behavioral experiments, five rats were trained to localize an airflow source placed at one of five locations around the perimeter of a circular arena. Three pieces of evidence demonstrated that information from the whiskers contributes significantly to the rat's ability to localize airflow. First, after the whiskers were removed, the rat's performance (accuracy) dropped significantly, while the control group of three other rats trained to localize a light source did not show a performance decrement after whisker removal. Second, during incorrect trials, the experimental group of rats deviated more after whisker removal, but the control group did not. Finally, the threshold airspeed at which rats can perform the localization task is higher before trimming than after trimming. Furthermore, the magnitude of the performance deficit after vibrissal removal is correlated with performance threshold: rats that exhibited a large performance drop after their whiskers were removed generally required higher airspeeds to successfully perform the localization task. This result suggests that rat whiskers, compared with other sensory cues, may play a particularly important role in sensing airflow at low speeds. Because air currents carry information about both odor content and location, these findings will be discussed in terms of the adaptive significance of the interaction between sniffing and whisking in rodents (see Section 5.5).

Chapter 3

Mechanical Responses of Rat Whisker to Airflow

This chapter was adapted mainly from the publication:

Yu, Y.S.W., Graff, M.M. and Hartmann, M.J.Z., Mechanical responses of rat vibrissae to airflow. *Journal of Experimental Biology*, **219**, 937-948 (2016b).

and partially from the manuscript:

Yu, Y.S.W., Bush, N.E. and Hartmann, M.J.Z., Whiskers in the wind: The vibrations of vibrissae and the activity of trigeminal primary afferents in response to a sustained airflow stimulus (in preparation).

3.1 Abstract

The survival of many animals depends in part on their ability to sense flow of the surrounding fluid medium. To date, however, little is known about how terrestrial mammals sense airflow direction or speed. The present work analyzes the mechanical response of isolated rat macrovibrissae (whiskers) to airflow in order to assess their viability as flow sensors. Results show that the whisker bends primarily in the direction of airflow and vibrates around a new average position at frequencies related to its resonant modes. The bending direction is not affected by airflow speed or by geometric properties of the whisker. In contrast, the bending magnitude and the vibration magnitude increases strongly with airflow speed and with the ratio of the whisker's arc length to base diameter. To a much smaller degree, the bending magnitude and the vibration magnitude also vary with the orientation of the whisker's intrinsic curvature relative to the direction of airflow.

These results are used to predict the mechanical responses of vibrissae to airflow across the entire array, and to show that the rat could actively adjust the airflow data that the vibrissae acquired by changing the orientation of its whiskers. Surprisingly, at low airspeed, whiskers vibrate parallel to the airflow direction, transitioning to perpendicular vibration at high airspeed. Like the whiskers of pinnipeds, the macrovibrissae of terrestrial mammals are multimodal sensors – able to sense both airflow and touch – and they may play a particularly important role in anemotaxis.

3.2 Introduction

With the exception of a few species, the faces of therian mammals are covered in vibrissae (whiskers), typically arranged on the cheek in an orderly pattern of rows and columns (Brecht et al., 1997; Muchlinski, 2010; Grant et al., 2013b). Whiskers have been the subject of research in both rodents (Bosman et al., 2011) and marine mammals (Dehnhardt et al., 2001; Hanke et al., 2013), but studies in these animals have largely focused on separate aspects of whisker function.

Rodents exhibit “whisking” behavior, in which the vibrissae are rhythmically (5-25 Hz) tapped and brushed against surfaces to enable direct tactile exploration (Welker, 1964; Carvell and Simons, 1990). Studies in rodents have therefore focused primarily on the use of whiskers as contact sensors, investigating questions in active tactile perception and sensorimotor integration (Diamond et al., 2008).

In contrast to rodents, pinnipeds do not exhibit clear whisking behavior, although the entire mystacial pad can move slightly as a whole. Studies in pinnipeds have focused primarily on the use of whiskers as remote flow sensors (Glaser et al., 2011; Miersch et al., 2011; Wieskotten et al., 2011). For example, it has been shown that seals can use their whiskers to track the wake of an artificial fish (Dehnhardt et al., 2001).

To date, however, few if any studies have investigated the possibility that terrestrial mammals might also use their vibrissae as flow sensors. If air currents of the magnitude typically found in natural environments generate significant vibrissal motion, then animals may exploit this sensation to their advantage.

This study takes the first steps towards investigating the possibility that the vibrissae may serve as airflow sensors in terrestrial mammals. We focus specifically on characterizing the mechanical response of the rat's "macrovibrissae" to airflow. The rat's macrovibrissae range in length between ~1 – 6 cm, much longer than the numerous "microvibrissae" (~1 mm) which segue into the fur (Welker, 1964; Brecht et al., 1997; Hartmann, 2001; Kuruppath et al., 2014). We first quantify how individual macrovibrissae bend and vibrate in response to airflow, and then generalize these results to predict how these responses will vary across the entire vibrissal array.

3.3 Materials and Methods

All procedures were approved in advance by Northwestern University's Animal Care and Use Committee.

3.3.1 Experimental setup

The experimental setup illustrated in Fig. 3.1A allowed us to independently vary airflow speed and the orientation of the vibrissa's intrinsic curvature relative to the airflow.

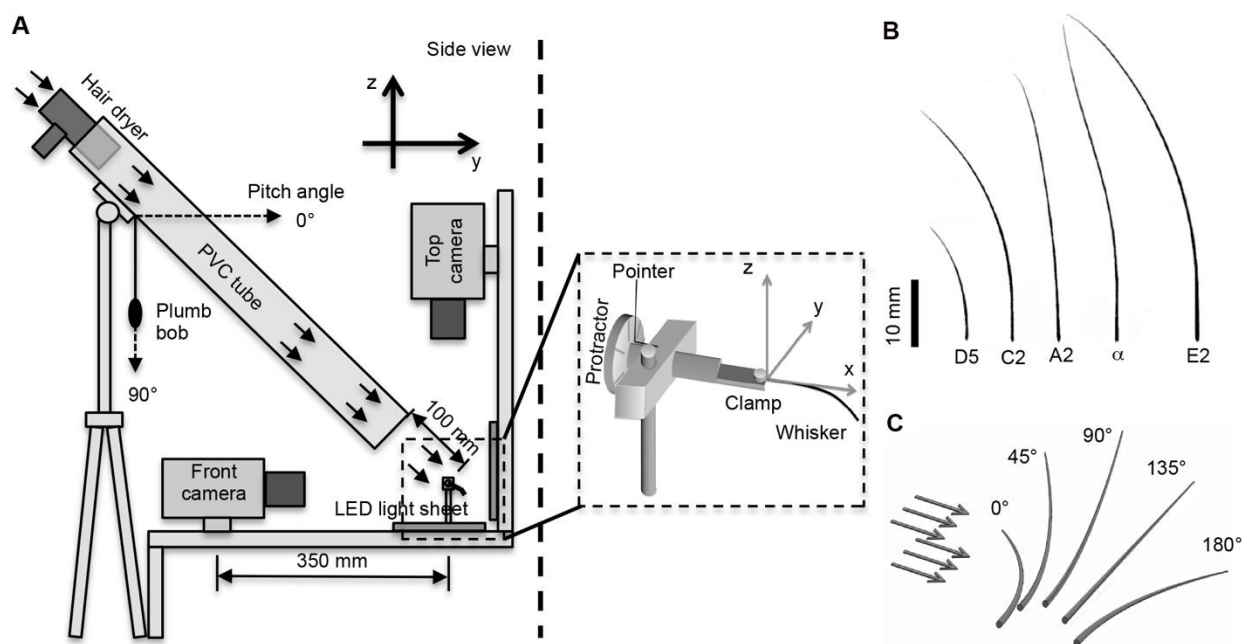


Figure 3.1 The experimental setup allowed airflow speed and the orientation of the vibrissa's intrinsic curvature relative to the airflow to be varied independently. (A) Schematic of the setup and definition of coordinate systems. The x-axis is directed axially, along the length of the whisker near its base, the y-axis is transverse to the whisker and parallel to the ground, and the z-axis is transverse to the whisker, vertical. The air source was fixed in position at a 45° angle relative to the ground. The expanded and rotated view illustrates the whisker mounted on the post along with the protractor used to determine the orientation angle of the whisker's intrinsic curvature relative to the airflow. Two LED light sheets provided illumination. (B) Manual tracings of the scans of the five whiskers used in the present experiment. (C) Definition of the orientation angle of the whisker relative to the airflow. A protractor was used to orient the whisker relative to the airflow.

Five orientation angles (0° , 45° , 90° , 135° , and 180°) were tested. When in the 0° and 180° orientations, the plane of the whisker was in the plane of the airflow. When oriented at 90° the plane of the whisker was perpendicular to the plane of the airflow.

Individual whiskers were plucked from one 2-year-old, female, Long Evans rats (*Rattus norvegicus*) and rigidly clamped to a metal post. No more than 96 hours elapsed between the time that the whisker was plucked and the experiment.

Two high-speed video cameras (Photron, FASTCAM-1024PCI), each fitted with a macro lens (Nikon, AF Micro-Nikkor 60mm f/2.8D) were mounted orthogonally ~ 35 cm from the whisker. The F-stop was set to F16 and 8-bit monochrome images were obtained with 1024×1024 resolution at 1,000 frames per second. Resolution near the focal plane in the top and front camera views was 14.4 ± 0.5 and 15.2 ± 0.8 pixels/mm, respectively. A command-obey configuration and software trigger provided synchronization (± 12.7 nS per manufacturer's specifications).

3.3.2 Orientation of the whisker relative to the airflow and quantification of airflow speed

The present experiments aimed to study the quasi-static deflection (bending) and vibrations of the whisker in response to naturalistic airflow stimuli rather than the flow structure around the whisker. Therefore, no effort was made to ensure flow laminarity or to characterize the details of the flow structure. We did, however, choose airflow speeds that the rat might encounter in the natural environment. Meteorological studies find typical land-surface wind speeds between 0-5 m/s (Monahan et al., 2011). We confirmed this range using a hot wire anemometer (Omega, model HHF42, resolution ± 0.1 m/s) to measure airflow speeds in locations where rats are expected

(bushes, dumpsters, fields, etc.). Although these measurements were not comprehensive, they ensured that our range was reasonable, even for airflow close to objects or the ground.

A hair dryer without heating was fixed in position to blow air at the whiskers through a PVC tube 4 inches in diameter and 38 inches long. The PVC tube was oriented 45° relative to the ground to avoid obstructing the cameras.

The hair dryer had two speed settings. A variable diameter air constrictor was placed over the intake to obtain a total of six airflow speeds (approximately 0.5, 1.4, 2.2, 3.4, 4.4, and 5.6 m/s). The anemometer was used to measure the average airflow speed at the whisker. At the lowest speed setting the speed measured at the whisker tip and base were the same to within the anemometer's resolution. At the highest speeds, the speed at the tip and base differed by at most 0.2 m/s. For these trials, the average speed at the tip and base was taken to be the speed around the whisker.

Fig. 3.1B illustrates the shapes and lengths of the five whiskers used in the experiments. From shortest to longest, the whiskers were D5, C2, A2, α , and E2. Whisker parameters are listed in Table 3.1.

As seen in Fig. 3.1B, rat vibrissae have an intrinsic curvature that approximates a parabola (Knutsen et al., 2008; Towal et al., 2011; Quist and Hartmann, 2012). Each whisker was aligned

with a protractor to obtain five different orientations relative to the airflow (Fig. 3.1C), and the six airflow speeds were tested at each orientation.

Table 3.1 Geometric parameters of the whiskers and values of λ_n used to predict resonant frequencies for the fixed-free conical beam. Values in cells with a white background are taken directly from Table 1 of Georgian (1965). Values for the vibrissae used in the present study are in cells shaded with a gray background. These values were interpolated from the data of Georgian (1965) to adjust for measured tip and base diameter. A_t is the area of the tip of the conical cantilever beam and A_b is the area of the base

Whisker identity	Length (mm)	Tip diameter (μm)	Base diameter (μm)	$(A_t/A_b)^{1/2}$	λ_n for Mode 1	λ_n for Mode 2	λ_n for Mode 3
				1.00	3.52	22.03	61.70
				0.50	4.63	19.55	48.50
				0.33	5.29	18.76	43.78
				0.25	5.85	18.51	41.34
A2	36.5	14	127	0.11	7.09	18.69	37.44
α	43.1	13	127	0.10	7.16	18.71	37.22
				0.10	7.20	18.71	37.10
E2	49.6	14	174	0.08	7.46	19.12	37.33
C2	34.3	11	149	0.07	7.63	19.39	37.45
D5	17.2	2	130	0.01	8.55	20.87	38.30
				0	8.72	21.15	38.45

3.3.3 Tracking the whisker's three dimensional shape

The two-dimensional (2D) camera views were tracked semi-automatically. In the first frame of each trial, the user manually selected the whisker's base point in top and side views. Because the base was clamped, its location was assumed constant throughout a trial. The tracking algorithm worked from base to tip, finding the darkest pixels along the whisker's length.

Three-dimensional (3D) merging of the 2D images was performed using the Camera Calibration Toolbox for Matlab[®] (Bouguet, 2013) using a 6×6 calibration grid. Each grid element was 5.08 mm (0.2 inches) square. Images of the calibration pattern were taken at 16 unique orientations spanning the range of the whisker's movement. The toolbox uses these images to create a model for each camera, including corrections for lens distortion. The models allowed us to merge conjugate pairs of points in the two camera views to a single 3D point. Conversely, we were also able to guess a 3D location and project the point into each camera view.

Because we could not place fiducial markers on the whisker without changing its dynamics we solved the inverse problem, in which we guess the 3D position of a whisker node and fit its projections in the 2D images using an optimization algorithm. The optimization begins at the whisker base because it provides one conjugate pair from which to start.

The optimization divided the whisker into nodes 2 mm apart, numbered from 1 to N from base to tip. The optimization used rigid body transformations to rotate node $n+1$ about node n . It used gradient descent to minimize the distance between each guess (of the position of the 3D node) and the closest tracked point in each 2D projection image. Each node's optimization was deemed complete when the spatial tolerance (change in total error between the 3D-back-projected and two actual 2D views) was less than 1×10^{-4} mm or a maximum of 1,000 iterations was reached. Due to blurring around the tip, whiskers were tracked to ~80% of the total arc length.

3.3.4 Quantifying whisker mass, length, diameter, volume, density, and taper

Whiskers were massed using a Mettler-Toledo UMX2 ultra microbalance (± 0.1 micrograms). After massing, the whiskers were scanned on a flatbed scanner (Epson Perfection 4180 Photo) and traced in Photoshop (Fig. 3.1B).

Next, we applied correction fluid (“white out”) to add ~ 5 mm stripes to each whisker in ~ 2 mm intervals. The diameter of the whisker at each stripe transition was measured at magnifications between 10x and 40x under an Olympus BX60 microscope. Photos were taken with a MBF Bioscience DV-47 camera. The arc length of each striped/non-striped segment was obtained by re-scanning on the flatbed scanner.

Each whisker segment was approximated as a truncated cone. The whisker’s total volume was obtained by summing the segmental volumes. Density was calculated by dividing the whisker’s mass by its volume. Taper was determined by performing a parabolic fit to the diameters measured at the locations of the stripe transitions along the whisker. Base and tip diameters were obtained from the parabolic fit.

3.3.5 Quantifying bending direction and bending magnitude

The present work was concerned with steady state, not transient, deflections of the whisker, so video recording began at least ten seconds after airflow was applied and lasted for five seconds.

The whisker base was set as the origin of a Cartesian coordinate system. As in previous work (Towal et al., 2011; Quist et al., 2014; Huet et al., 2015b), the x-axis was defined to lie along the proximal portion of the whisker (Fig. 3.1A, inset).

We defined the position of each node N with the whisker at rest as $[x_0, y_0, z_0]$. We defined the mean position (time average position) of each node N with the whisker in airflow as $[x_m, y_m, z_m]$,

$$x_m = \frac{1}{T} \sum_{k=1}^T x_k, y_m = \frac{1}{T} \sum_{k=1}^T y_k, z_m = \frac{1}{T} \sum_{k=1}^T z_k, \quad (\text{Equation 3.1})$$

where k is the frame number (1 ms/frame), T is the video duration (5,000 frames), and $[x_k, y_k, z_k]$ is the position of node n at frame k .

The tracked points on the whisker defined through Equation 3.1 allowed us to define the whisker's bending direction and bending magnitude, as follows:

Bending direction: For each node, bending direction was quantified by the angle between the direction of airflow and the vector connecting the position of the node at rest ($[x_0, y_0, z_0]$) to the mean position of the node in the airflow ($[x_k, y_k, z_k]$).

Bending magnitude: For each node, bending magnitude was calculated as the angle θ between two vectors: 1) the vector connecting the base point to the position of the node at rest, and 2) the vector connecting the base point to the mean position of the node in airflow. The definition of bending magnitude is schematized in two dimensions in Fig. 3.2.

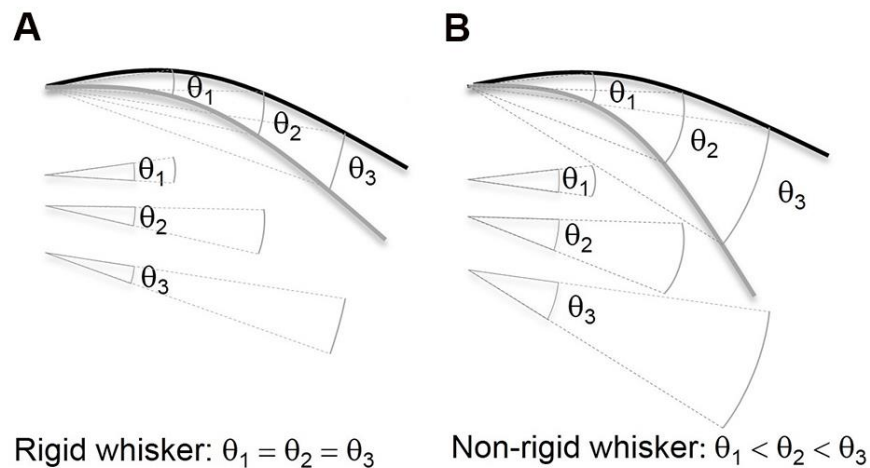


Figure 3.2 Schematic of bending magnitude (θ), quantified as the angular displacement of each node from rest to its position in the presence of airflow. The black curve indicates the whisker at rest, and the gray curve indicates the mean position of the whisker in the presence of airflow. If the whisker were rigid (left schematic) then θ would be the same at each node. Because real rat whiskers are flexible, the bending magnitude θ increases from base to tip (right schematic).

If the whisker were rigid, or if the follicle that held the whisker were very flexible, then the whisker would rotate only at its base, as occurs for flow-sensing insect hairs (Dechant et al., 2006). In this case, the bending magnitude would be identical at all nodes along the whisker (Fig. 3.2A). Rat whiskers are flexible, however, so bending magnitude must be computed at each node along the whisker length (Fig. 3.2B).

Fig. 3.2 illustrates the bending magnitude θ in 2D for visual clarity, however, throughout all of *Results*, θ was calculated in three dimensions as the angle between two vectors. Whisker bending does not occur entirely in the bending direction because turbulence causes out of the plane effects. However, as will be noted in Section 3.4 *Results*, the out of plane bending was small with an average value of 0.0° .

3.3.6 Quantifying vibration frequency

As will be described in Section 3.4 *Results*, all whiskers vibrated strongly in response to airflow, but the major axis of vibration was difficult to determine. We choose to quantify vibration frequency in the y-direction (transverse to the whisker, parallel to the ground).

For each whisker, a frequency representation was obtained from the y-position data (in units of mm) from the tracked node closest to 40% from the whisker base. Each 5,000 ms trial at each of the five orientations was split into five segments of 1,000 ms each, for a total of 25 segments.

Matlab[®] was used to calculate the absolute value of the fast Fourier transform (FFT) of each of the 25 segments of data, and these transformed signals were divided by the length of the segments. This procedure yielded 25 spectra for the y-amplitude as a function of frequency. These 25 spectra (units of mm) were then averaged, and this final average was termed the "mean amplitude spectrum."

As will be shown in Section 3.4 *Results* (Fig. 3.6), the peaks in the mean amplitude spectrum were broad, reflecting the wide range of frequencies and directions that characterized each whisker's vibrations. To associate a single experimentally-measured frequency with these broad peaks, a two-step procedure was used.

First, we determined the minimum and maximum values that could reasonably be expected for each of the resonance modes of each whisker, i.e., the widest possible range of expected frequencies. To do this, we used the following equation, which describes the resonance modes for a fixed-free tapered cantilever beam (Georgian, 1965):

$$f_n = (\lambda_n D/4S^2)(E/\rho)^{1/2}/(2\pi). \quad (\text{Equation 3.2})$$

In Equation 3.2 the whisker's base diameter (D) and arc length (S) as well as the calculated density for the whisker are measured values (see Section 3.2.4). We determined the coefficient λ_n from Table 3.1 (Georgian, 1965). To determine the widest possible range of expected frequencies, we set Young's modulus (E) either to 3 or 11 GPa in Equation 3.2. The ranges of frequencies established by this variation in Young's modulus are shown in yellow, cyan, and green in Fig. 3.6.

Second, we found the crest of the amplitude spectrum within the range of expected frequencies. To do this, we found the points at which the amplitude spectrum intersected the minimum ($E = 3$ GPa) and the maximum ($E = 11$ GPa) predicted frequencies. Those two points were connected by a line. We computed the vertical distance from the line to the amplitude spectrum at each

frequency. The largest distance defined the crest of the amplitude spectrum in that region, and the corresponding frequency was considered the experimentally-measured resonance frequency for that mode.

3.3.7 Quantifying vibration magnitude

Analogous to bending magnitude, the temporal vibration magnitude was quantified as the absolute angle between two vectors: (1) the vector connecting the base point to the mean position of the node in airflow, and (2) the vector connecting the base point to the temporal position of the node in airflow (see Fig. 3.10A in Section 3.4.7). The vibration magnitude is defined as the mean of 5,000 temporal vibration magnitudes, as indicated in the following equation:

$$\phi = \frac{1}{T} \sum_{k=1}^T \phi_k , \quad (\text{Equation 3.3})$$

where k is the frame number (1 ms/frame), and T is the video duration (5,000 frames). A temporal vibration magnitude, ϕ_k , at time frame number k , is defined as the angle displacement of a whisker from its temporal position to its mean position of the vibrating whisker.

3.3.8 Quantifying vibration direction

The vibration direction was quantified based on the whisker polar angle in the transverse plane, parallel to airflow direction, i.e., the y-z plane, to which whisker axis is normal. The definition of the polar angle can be seen from Fig. 3.12B in Section 3.4.9. Polar angles between $[0 \pi/2]$, $[\pi/2 \pi]$, $[-\pi -\pi/2]$, and $[-\pi/2 0]$ define the first, the second, the third and the fourth quadrants, respectively. The whisker nodal positions at 5,000 time frames projected in y-z plane shape in circle or ellipse (see examples in Fig. 3.12A). After viewing each whisker's positions in y-z plane at each velocity and each orientation, we found in many cases that the major axis of the ellipse is either parallel or orthogonal to airflow direction. We then introduced a vibration direction index (*VDI*) to look how likely the vibration direction is parallel or orthogonal to airflow direction. The vibration direction index is indicated in the following equation

$$VDI = \frac{N_{\perp}}{N_{\parallel}}, \quad (\text{Equation 3.4})$$

where N_{\perp} denotes the number of frames in which the whisker nodal position fell in the first or the third quadrants, and N_{\parallel} is the count either in the second or the fourth quadrants. The airflow direction is from the second quadrant to the fourth quadrant, 45 deg to the x-axis. Therefore N_{\perp} quantifies the frequency of whisker position perpendicular to airflow direction, whereas N_{\parallel} quantifies the frequency of whisker position in parallel with airflow direction. As seen from Fig. 3.12A, $VDI > 1$ defines an ellipse shape with its major axis in the first and the third quadrants, $VDI < 1$ defines an ellipse shape with its major axis in the second and the fourth quadrants, and $VDI \approx 1$ defines a circular shape.

3.4 Results

We begin by showing that the whisker primarily bends in the direction of airflow and vibrates around a new average position. The bending magnitude is shown to depend strongly on airflow speed, orientation of the whisker relative to the airflow, and whisker geometry. The vibrations occur at frequencies correlated with the whisker's resonance modes. We analyze how bending and vibrations are likely to vary across the whisker array in response to airflow. Vibration magnitude scales to bending magnitude. Vibration direction is parallel to the airflow direction at low airspeed, but transitions to a direction perpendicular to airflow direction at high airspeed.

3.4.1 The whisker primarily bends in the direction of the airflow and oscillates about that new position

As described in Section 3.3 *Materials and Methods*, five whiskers (E2, α , A2, C2, and D5) were plucked from a rat. The base of each whisker was rigidly clamped to a post and air was directed on the whisker at different speeds. All results are described in the experimental reference frame in which the direction of airflow is taken to be 0° , the z-axis is vertical, the y-axis is parallel to the ground, and the x-axis is parallel with the whisker base.

The typical response of a whisker to airflow of moderate speed (2.3 m/s) is shown in Fig. 3.3 (A and B), with the whisker oriented 45° relative to the airflow. This figure quantifies the motions of the same whisker shown in Supplementary Video S3.1.

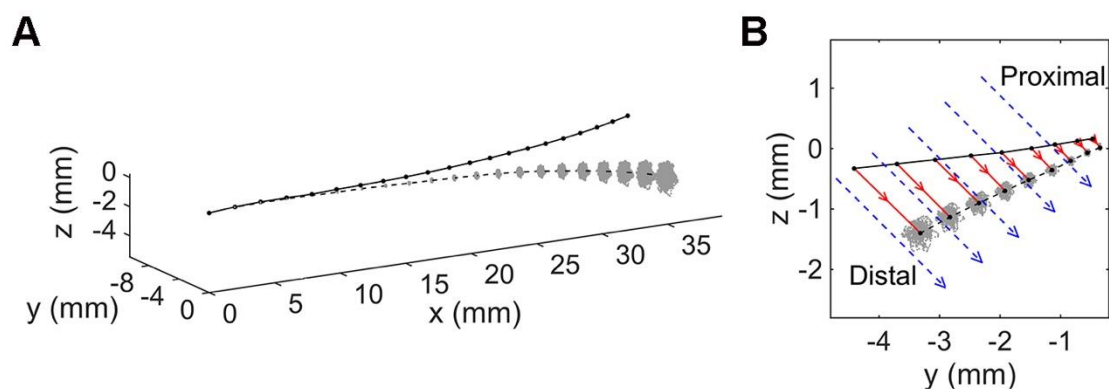


Figure 3.3 A whisker will mostly bend in the direction of airflow, and will exhibit vibration about its new mean position. The figures depict the response of the E2 whisker to airflow with speed of 2.3 m/s, (see Movie S3.1 for the motion of this whisker). **(A)** The whisker is oriented 45° relative to the airflow and its shape is tracked in both the absence and presence of airflow. The position of the whisker without airflow is shown as a solid black line, with 21 black dots indicating the 21 tracked nodes, spaced 2 mm apart. In the presence of airflow, the whisker deflects to a new mean position (black dashed line) and oscillates about that mean position (ellipses of gray dots). Each dot in each ellipse represents the position of that node in one video frame (1 ms). **(B)** Projection of the whisker shown in (A) into the y-z plane. The small red solid vectors from the whisker at rest to the whisker's mean position indicate the bending direction of the tracked nodes of the whisker. The magnitude of these vectors increases along the whisker's arc length, as does the amplitude of vibration, as indicated by the increasing size of the gray ellipses. The large dashed blue arrows indicate the airflow direction, and are mostly parallel with the vectors indicating the bending direction of the whisker.

Three characteristics of the whisker's response are seen in Fig. 3.3. First, the whisker bends to a new mean position under the influence of the airflow, and it oscillates about that new mean. In Fig. 3.3A the vibrations of the whisker nodes are seen as ellipses, with each dot in the ellipse representing the location of the node in a single video frame (1 ms). Second, as shown in Fig. 3.3B, the bending magnitude, as well as the amplitude of vibration, increases along the arc length of the whisker from proximal to distal. The increased vibration amplitude is seen as increasing area of the ellipses along the whisker length. Third, Fig. 3.3B shows that the primary bending direction is

in the direction of airflow. The small red arrows indicating bending direction are almost completely parallel with the large blue dashed arrows, indicating the airflow direction.

Note that the bending direction as defined in Fig. 3.3 is the direction in which the whisker travels from its resting position to its new mean position. This direction is not always the same as the direction in which the whisker vibrates. In fact, sometimes the vibrations did not even form a well-defined ellipse. The details of vibration magnitude and direction are complex, and will not be further described here.

3.4.2 Bending direction is independent of airflow speed and orientation of the whisker relative to the airflow

Fig. 3.3 showed only one example in which the primary direction of whisker bending was in the direction of airflow. We carefully examined the effect of speed and orientation angle for all five whiskers. Whisker deflections were recorded at six different airflow speeds, and at five different orientation angles of the whisker relative to the airflow as defined in Fig. 3.1C (0° , 45° , 90° , 135° , 180°).

Fig. 3.4 confirms that the whisker primarily bends in the direction of airflow, and also shows that the bending direction is independent of airflow speed and whisker orientation relative to the airflow. To create Fig. 3.4, bending direction was quantified at all tracked nodes of the whisker

and averaged to obtain means and standard deviations. Although all plots of Fig. 3.4 show substantial variability, the average bending direction is always in the direction of flow (0°).

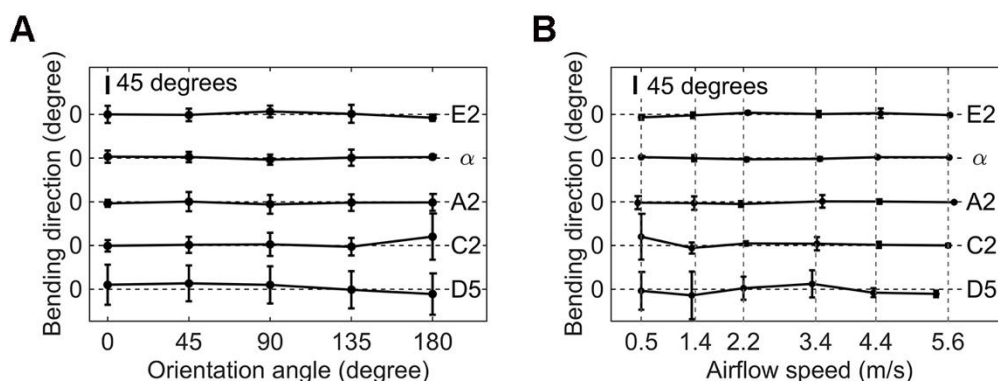


Figure 3.4 Bending direction does not vary systematically with orientation angle or airflow speed. In both plots whiskers are ordered by length, from longest (E2) to shortest (D5). In both plots the bending direction was averaged over all nodes except the first node at the base of the whisker, because it is fixed. **(A)** Mean and standard deviation of bending direction as a function of orientation angle for all five whiskers. Data are averaged over all six airflow speeds. **(B)** Mean and standard deviation of bending direction as a function of airflow speed for all five whiskers. Data are averaged over all five orientation angles. Notice that there is small variability in airflow speed for different whiskers, which is observed as small shifts in the placement of the data points on the x-axis. In both **(A)** and **(B)**, variability in bending direction is larger for shorter whiskers than for longer whiskers because measurement error was greater for smaller deflections.

Notably, the bending magnitude out of the plane of the airflow direction never exceeded 2.5° for any whisker, and its average was 0.0° , indicating that out-of-plane motion was equally likely to occur above and below the plane. In contrast, in-plane bending magnitude had a maximum amplitude of 32.5° and an average amplitude of 4.4° across all nodes and all whiskers.

3.4.3 Bending magnitude increases along the whisker and depends on airflow speed, orientation, and whisker geometry

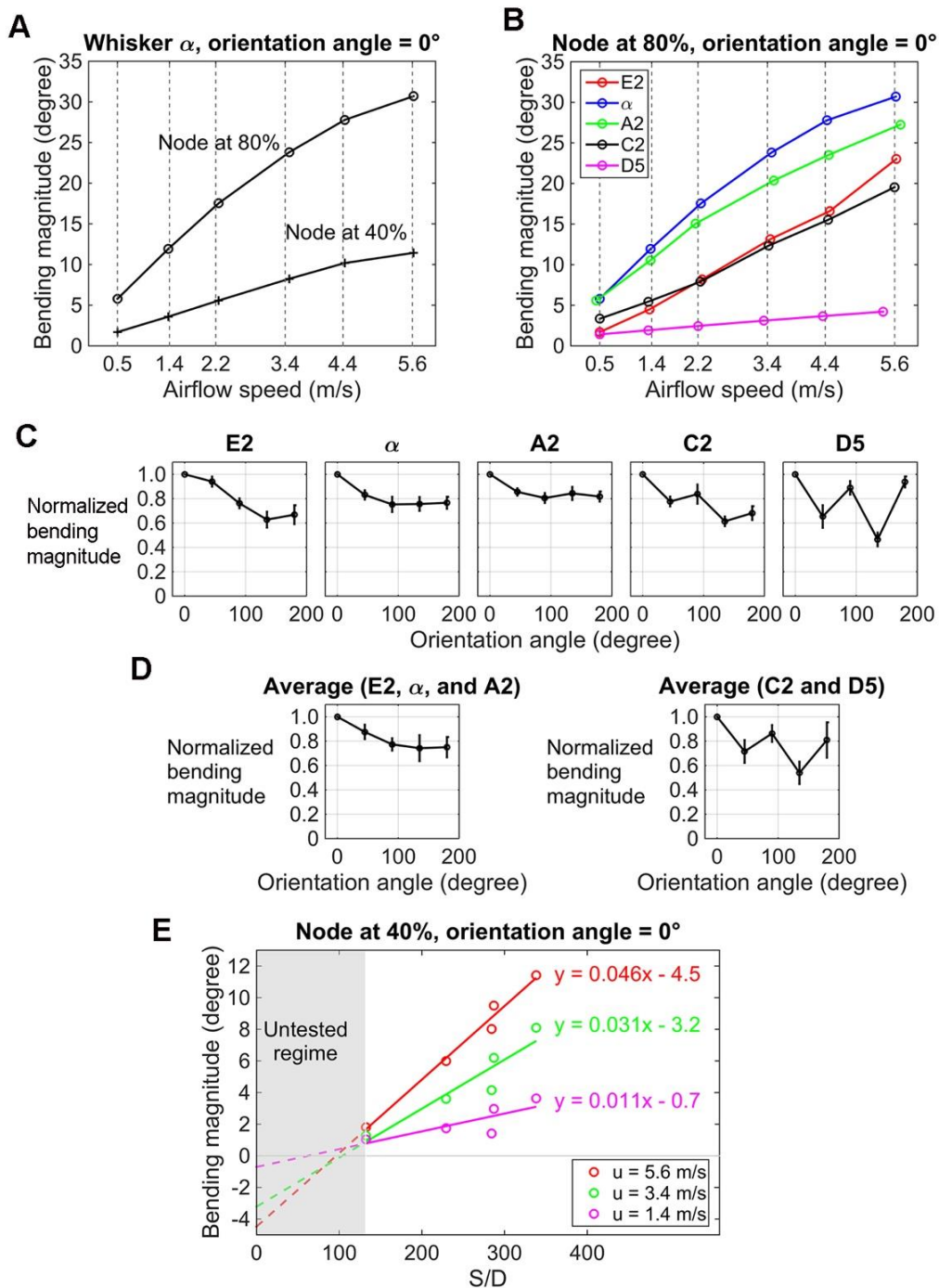


Figure 3.5 Bending magnitude depends on airflow speed, orientation angle of the whisker, and the whisker's arc-length to base diameter (S/D) ratio. (A) The bending magnitude of whisker α at an orientation of 0° relative to the airflow is shown for nodes 40% and 80% out along the whisker length. (B) Bending magnitude of all five whiskers increases monotonically with airflow speed. Results are shown for whiskers oriented 0° relative to the airflow and for nodes 80% out along the whisker length. (C) For each whisker, normalized bending magnitude varies with orientation angle. Bending magnitude was normalized by that whisker's largest bending magnitude, which was always found at an orientation angle of 0° (concave forwards, toward the airflow). The normalized bending magnitude at each orientation angle is averaged over the four highest airflow speeds. Data are shown for a node 40% out along the whisker length. (D) For the three larger whiskers (E2, α , and A2) normalized bending magnitude decreases smoothly with orientation angle, while for the two shorter whiskers (C2 and D5) the relationship is "W" shaped. These results are averages of those shown in (C). (E) Bending magnitude increases approximately linearly with the S/D ratio of the whisker. The whisker identities are D5, C2, E2, A2 and α , ordered from small to large S/D ratios. Note that the S/D ratio for E2 is only slightly smaller than S/D for A2. Results are shown for a node 40% out along each whisker and at airflow speeds of 1.4 m/s, 3.4 m/s, and 5.6 m/s. Linear fits between bending magnitude and the S/D ratio show increasing slopes with airflow speed. Because the airflow speeds were not identical for all five whiskers, values of bending magnitude have been interpolated between the airflow speeds closest to the speed of interest.

Bending magnitude along the whisker length will be influenced by Reynolds number, material properties of the whisker (density and Young's modulus), and geometric parameters of the whisker (base diameter, arc length, taper, and intrinsic curvature). Understanding the effects of all these parameters is challenging. To start, analysis was limited to three major parameters that will strongly influence bending magnitude: airflow speed, orientation angle, and the ratio of whisker length to base diameter (S/D ratio).

Unsurprisingly, bending magnitude was strongly correlated with airflow speed, and was larger at more distal locations along the whisker. This effect is illustrated for two nodes of the α whisker in Fig. 3.5A. Bending magnitude increases monotonically with airflow speed for both nodes, but is much larger at a node 80% out along the total whisker length than at a node 40% out. These results indicate that the whisker does not bend as a rigid body (c.f., Fig. 3.2). Although the results of Fig.

3.5A are shown only for an orientation angle of 0° , similar results were found for all orientation angles.

The results shown in Fig. 3.5A were found to generalize across all whiskers, as shown in Fig. 3.5B. All whiskers show an approximately linear increase in bending magnitude with airflow speed. Again, results are shown only for an orientation angle of 0° , but similar results were found for all orientation angles.

The effect of orientation angle is subtler. At the lowest two airflow speeds (0.5 m/s and 1.4 m/s), no effect of orientation angle could be observed, and these speeds were excluded from subsequent analysis of orientation angle. At higher airflow speeds (2.2 m/s and above), systematic variations of bending magnitude with orientation angle were found.

Specifically, for all whiskers the bending magnitude at orientation angle 0° (concave forward into the airflow) was always larger than at any other orientation angle. Fig. 3.5C shows the bending magnitude at each orientation angle, normalized by the bending magnitude at orientation 0° . For the larger three whiskers (E2, α , and A2), the curves show a profile that decreases smoothly from 0° to 180° . In contrast, the two shorter whiskers (C2 and D5) show a W-shaped profile, with a crest near 90° (concave downwards orientation).

Notice that the effects of orientation angle cannot be directly related to whisker length. The fundamental basis for orientation effects must be the whisker's intrinsic curvature, because this is

the only parameter that affects the whisker's 3D symmetry. Shorter whiskers have higher intrinsic curvature (Knutsen et al., 2008; Towal et al., 2011; Quist and Hartmann, 2012), explaining why the effect of orientation angle appears to be related to whisker length. From a mechanical point of view, the intrinsic curvature of the whisker allows it to “twist” about its own axis, and will have a non-linear effect on both axial force and bending (Huet et al., 2015b; Huet and Hartmann, 2016). The results for the longer and shorter whiskers are averaged in Fig. 3.5D, where the smooth drop off and “W” shape became even clearer.

Finally, Fig. 3.5E illustrates how bending magnitude is affected by S/D ratio for three different airflow speeds. In general, there is an approximately linear trend, such that bending magnitude increases with S/D ratio for all airflow speeds tested. Given that the area moment of inertia (which determines bending) scales as radius to the fourth power, it makes good intuitive sense that a whisker with a low S/D ratio will bend less than a whisker with a large S/D ratio.

3.4.4 The whisker vibrates at frequencies correlated with its resonance modes

Like all mechanical systems, whiskers tend to vibrate near their resonance frequencies (Hartmann et al., 2003; Neimark et al., 2003; Andermann et al., 2004; Ritt et al., 2008; Boubenec et al., 2012; Yan et al., 2013). Making the standard assumption that a whisker is linearly tapered (Ibrahim and Wright, 1975; Williams and Kramer, 2010; Quist et al., 2011; Hires et al., 2013) and can be modeled as a fixed-free conical beam (Georgian, 1965), the whisker's resonant frequency can be computed according to Equation 3.2 of Section 3.3 *Materials and Methods*.

We aimed to compare whisker vibrations with their theoretical resonance profiles, however, under the influence of airflow whiskers were observed to vibrate in all three dimensions, and in many cases the major axis of vibration was challenging to define. In performing the vibration analysis we had to make two choices: first, which direction of motion to analyze, and second, which node out along the whisker arc length to analyze.

To decide on the direction of motion to analyze we first quantified vibration magnitude and frequency in the x-, y-, and z- directions, as defined in Fig. 3.1A. The y- and z- directions are both transverse to the base of the whisker, while the x-direction is directed axially. Unsurprisingly, vibrations in the y- and z- directions were similar in both magnitude and frequency, while vibrations in the x-direction were much smaller and more variable in magnitude. Because results in y- and z- directions were so similar, results show only the frequency content of the vibration in the y-direction.

To decide on which node to analyze, we examined the frequency content at each node individually. At proximal nodes, the vibration magnitude was so small that the frequency was challenging to identify, while at distal nodes the vibration magnitude was large, but only the first mode of vibration could be observed. We ultimately chose to perform the frequency analysis at a node 40% out along the whisker arc length because the vibration magnitude was large enough to permit accurate measurement and multiple modes of vibration could be observed.

With these choices made, Fig. 3.6A shows the frequency content of vibrations of all five whiskers in response to airflow at a speed close to 5.6 m/s. Results for all five whiskers are averaged over the five orientation angles. Because the resonance peaks are broad, however, it is challenging to estimate the peak frequencies. For example, the first mode of whisker A2 does not have a well-defined peak.

To address this problem, we found the “widest possible range” for each resonance mode using Equation 3.2 of Section 3.3 *Materials and Methods*. In Fig. 3.6A the widest possible ranges for the first, second, and third resonance modes are highlighted in yellow, cyan, and green, respectively. The points at which the mean amplitude spectrum intersected the boundaries of these ranges were connected by imaginary line segments, and the vertical distance from the segments to the mean amplitude spectrum was found at each frequency. The largest distance was taken to define the crest of the spectrum, and the corresponding frequency was considered to be the resonance frequency for that mode. This procedure allowed us to establish a single experimentally-measured value for each resonance mode.

To compare observed and predicted resonance frequencies Young’s modulus was left as a free parameter and optimized by minimizing the summed squared error between predicted and experimental values, for all frequency modes, for all five whiskers. A best fit between predicted and observed resonance frequencies was obtained with a Young’s modulus of 6.6 GPa ($R^2 = 0.986$), as shown in Fig. 3.6B.

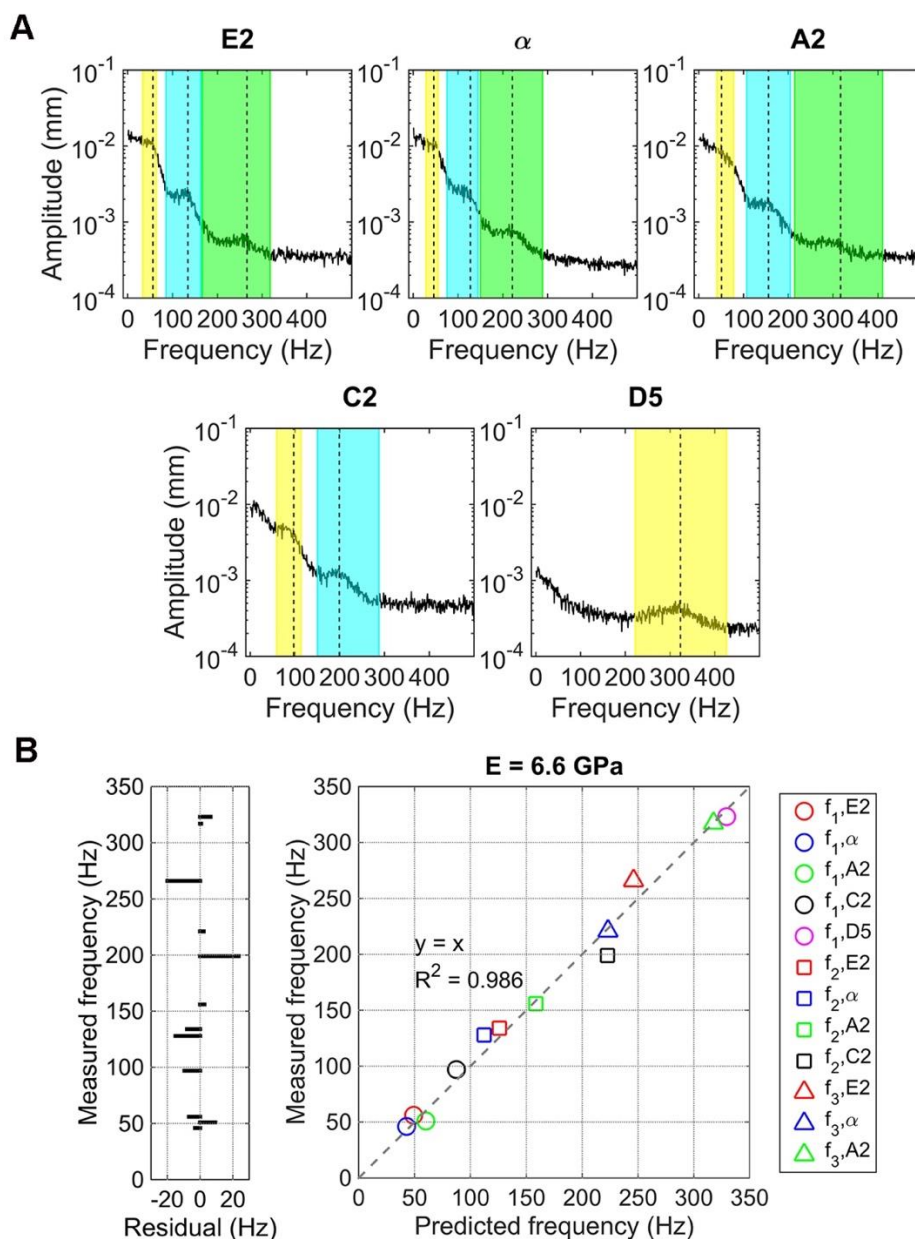


Figure 3.6 The vibration frequencies of a whisker are correlated with its resonance modes (A) The average y-amplitude as a function of frequency in units of mm (the “mean amplitude spectrum”) is shown for all five whiskers for an airflow speed close to 5.6 m/s. Vibrations were measured in the y-direction, that is, transverse to the whisker and parallel to the ground. All position data were obtained from the tracked node closest to 40% out along the total whisker length. Data have been averaged across all orientation angles relative to the airflow. Whiskers E2, α , and A2 show three clear resonance modes, C2 shows two resonance modes, and D5 shows only the first mode resonance. The regions highlighted in yellow, cyan and green indicate the “widest possible range” for each resonance mode, found by inserting Young’s modulus = 3 GPa or 11 GPa into Equation

3.2 in Section 3.3 *Materials and Methods*. The vertical dashed lines indicate the peak of the amplitude spectrum within that resonance range. **(B)** Comparison of experimental and theoretical values for the resonance frequencies shows an excellent match. The best linear fit between predicted and measured values for all modes of all five whiskers was found with Young's modulus set to 6.6 GPa.

3.4.5 Computing mechanical responses to airflow across the entire vibrissal array

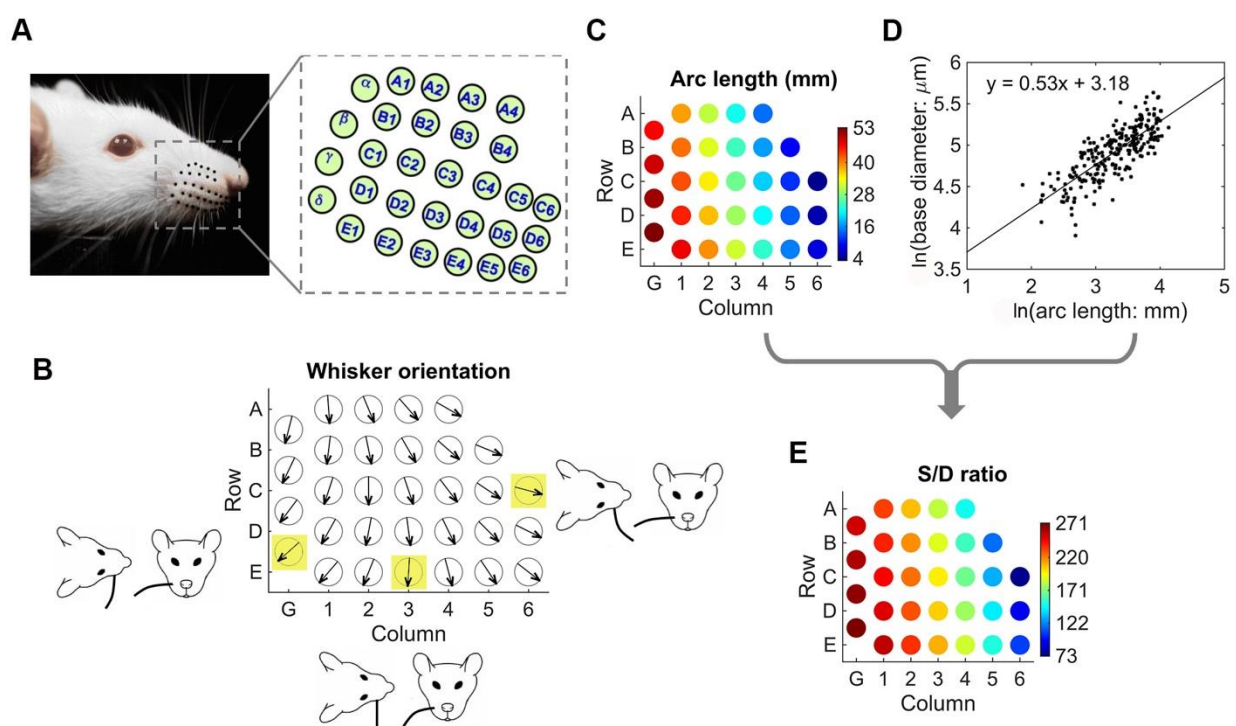


Figure 3.7 Parameters used to calculate bending magnitude and vibration frequency in response to airflow. **(A)** A photo of rat whisker pad with whisker basepoints enhanced as black dots. Whiskers are arranged in an array and named by their (row, column) identity. **(B)** Whisker orientation across the array when the rat's head is approximately level and the whiskers are at rest. The circles represent the vibrissal base points. The arrow in each circle is a direction vector that indicates the concave-forward direction of the vibrissa's intrinsic curvature. Three examples are shown to improve intuition for how the orientation of whisker curvature varies across the array. **(C)** Arc length varies strongly with column and weakly with row across the whisker array (data from (Towal et al., 2011)). **(D)** An analysis of 244 whiskers showed that a power-law adequately described the relationship between base diameter and arc length. **(E)** The arc length to diameter (S/D) ratio increases from rostral to caudal with a smaller dependence on row.

The previous sections have indicated that a vibrissa's response to airflow depends not only on airflow speed, but also on the whisker's orientation relative to the airflow and on the S/D ratio. As shown in Fig. 3.7A, the rat's vibrissae are arranged in a regular array of rows and columns on the cheek. Their orientation and geometry varies systematically across the array (Ibrahim and Wright, 1975; Brecht et al., 1997; Diamond et al., 2008; Towal et al., 2011). We used these systematic variations to estimate how the vibrissal response to airflow will vary across the array.

We began by accounting for the whisker's geometric parameters: the orientation of its intrinsic curvature on the rat's face, the whisker's arc length, base diameter, and the S/D ratio:

Orientation of the whisker's intrinsic curvature: Previous work has shown that each whisker has a unique intrinsic curvature (Knutsen et al., 2008; Towal et al., 2011). The orientation of the intrinsic curvature shifts smoothly from concave downwards in caudal regions of the array to concave forward in more rostral regions. This smooth variation is depicted in Fig. 3.7B; the equation for orientation as a function of the (row, column) position of the whisker is $\zeta = 18.8col - 11.4row - 5.0$ (Towal et al., 2011).

Arc length (S): Whisker arc length increases with column (from rostral to caudal), with a weak dependence on row, as shown in Fig. 3.7C. The equation for arc length as a function of (row, column) position is $S = -7.9col + 2.2row + 52.1$ (Towal et al., 2011).

Base diameter (D): To date, whisker diameter has not been characterized as a function of (row, column) position, however, previous work found a power law relationship between base diameter and whisker arc length (Hartmann et al., 2003; Neimark et al., 2003). We confirmed this relationship using data obtained from 244 whiskers in a concurrent study. Results are shown in Fig. 3.7D. The best fit equation was found to be: $D = 24.1S^{0.53}$.

S/D ratio: Finally, we used the equations from Fig. 3.7 (C and D) to compute the S/D ratio for each whisker, as illustrated in Fig. 3.7E.

The parameters identified in Fig. 3.7 allow us to combine the orientation and geometric data with the empirical relationships found in Fig. 3.5 to simulate how bending magnitude will vary across the vibrissal array for three different airflow speeds. These simulations were run as follows:

- The airflow direction was assumed to be horizontal, parallel with the ground.
- The simulated rat was assumed to have a level head pitch, parallel to the ground as depicted in Fig. 3.7A. The head pitch determines each whisker's orientation relative to the (horizontal) airflow.
- The S/D ratio for each whisker was determined from Fig. 3.7E. Three whiskers (C6, D6, E6) were excluded from analysis because their S/D ratios were less than 132, within the untested regime of Fig. 3.5E.
- Given the S/D ratio of each whisker and an airflow speed, the equations of Fig. 3.5E were used to compute the whisker's bending magnitude, for a node 40% from the base and an orientation angle of 0° .
- To account for each whisker's orientation relative to the airflow, results were scaled by the ratios shown in Fig. 3.5D. Whiskers with S/D ratios greater than 250 were assumed to

follow the smooth, “large whisker” average, while whiskers with S/D ratios smaller than 250 were assumed to follow the W-shaped “small whisker” average.

Simulation results are shown in Fig. 3.8. At a single airflow speed (Fig. 3.8A), the dominant effect is the S/D ratio. Bending magnitude decreases from the Greek Column to Column 5. Smaller variations are seen from Row E to Row A. The trend with column remains close to linear across the full range of airflow speeds (Fig. 3.8B).

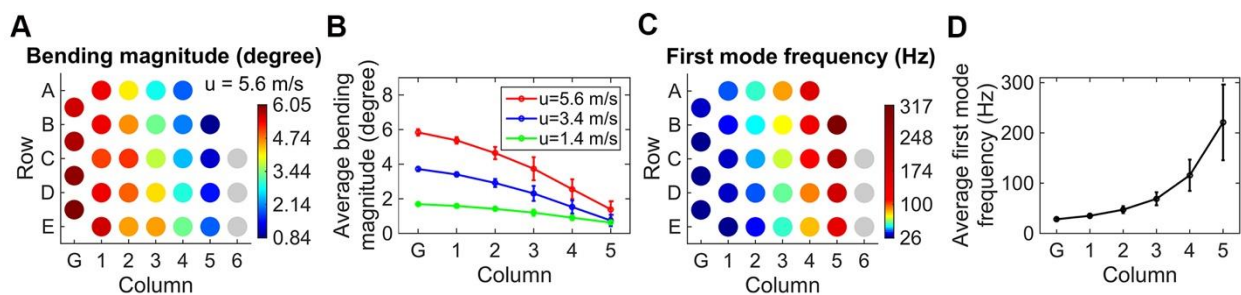


Figure 3.8 Bending magnitude and vibration frequency in response to airflow predicted across the full array of whiskers. **(A)** Predicted bending magnitude at nodes 40% out along each whisker in response to airflow at 5.6 m/s. Overall, bending closely follows the S/D ratio shown in Fig. 3.7E. The three most rostral whiskers are omitted from this analysis because they fall into the “untested regime” of Fig. 3.5E. **(B)** Bending magnitude as a function of column (averaged across rows) is predicted for three different airflow speeds. **(C)** Predicted first mode resonance frequencies across the whisker array. Vibration frequency increases from caudal to rostral. Note that the colorbar is very non-linear. **(D)** The predicted first mode frequency is shown as a function of column, averaged across rows.

A similar analysis was performed for vibration frequency with results shown in Fig. 3.8 (C and D). This figure required an estimate of each whisker’s tip diameter, but the tips of the 244 whiskers shown in Fig. 3.7D were often significantly damaged. Fortunately, tip diameter has only a small effect on frequency (Georgian, 1965), so the average value, 6 μm , was used for all whiskers.

Inserting the values of base diameter, tip diameter, arc length, the best fit value for Young's modulus (6.6 GPa), and the average density (1,300 kg/m³), into the equation for whisker resonance (Equation 3.2), we predicted the first mode resonance frequency of all whiskers. As shown in Fig. 3.8 (C and D), the first mode resonance frequency increases from Column G to Column 5 as the whiskers become shorter.

Thus bending and vibrations are complementary: larger, more caudal whiskers will experience larger bending magnitudes but lower frequency vibrations, while shorter, more rostral whiskers will experience smaller bending magnitudes but higher frequency vibrations.

3.4.6 The effect of head pitch and whisking motions on the response of vibrissae across the array

During “whisking” behavior rats rhythmically sweep the macrovibrissae between 5 and 25 Hz (Welker, 1964; Carvell and Simons, 1990). Rats also often pitch their heads up and down during navigation and tactile exploration. Both head and whisker motions will significantly change the whisker orientation relative to the airflow, which will affect bending magnitude (Fig. 3.5C). We used the same approach as in Fig. 3.8 to investigate the effect of head pitch and whisking on the response of vibrissae across the array.

The simulated bending magnitudes of the vibrissae at rest at two different head pitches are shown in Fig. 3.9A. Pitching the head upwards tends to increase bending magnitude because most whiskers will tend to orient more concave forwards towards the airflow (c.f., Fig. 3.5D).

We then simulated a 60° whisker protraction using kinematic equations obtained from behaving rats, which include the effects of dorsal-ventral elevation as well as the whisker's roll about its own axis (Knutsen et al., 2008). Simulated bending magnitudes for the array of protracted whiskers are shown in Fig. 3.9B, again for two head pitches. As in Fig. 3.9A, increasing head pitch increases overall bending magnitude.

Comparing Figs 3.9A and 3.9B, we see that whisker protraction causes more whiskers to orient concave forward into the airflow, producing an increase in the range of bending magnitudes for a given column. It is critical to note, however, that these simulations do not include the effects of changes in rostrocaudal angles; the simulations reveal only the effects of the changing orientation angles during protraction.

The results of Figs. 3.5, 3.8, and 3.9 are subject to two important caveats: experiments were performed on isolated whiskers, and airflow was always directed perpendicular to the whisker length. In reality, the rat's head will affect the flow field around each whisker, and whiskers will emerge from the face at many different angles relative to the flow. Although more experiments are required to investigate these effects, the general trends revealed by Figs. 3.5, 3.8, and 3.9 support the conclusion that the rat has a rich motor repertoire for flow exploration.

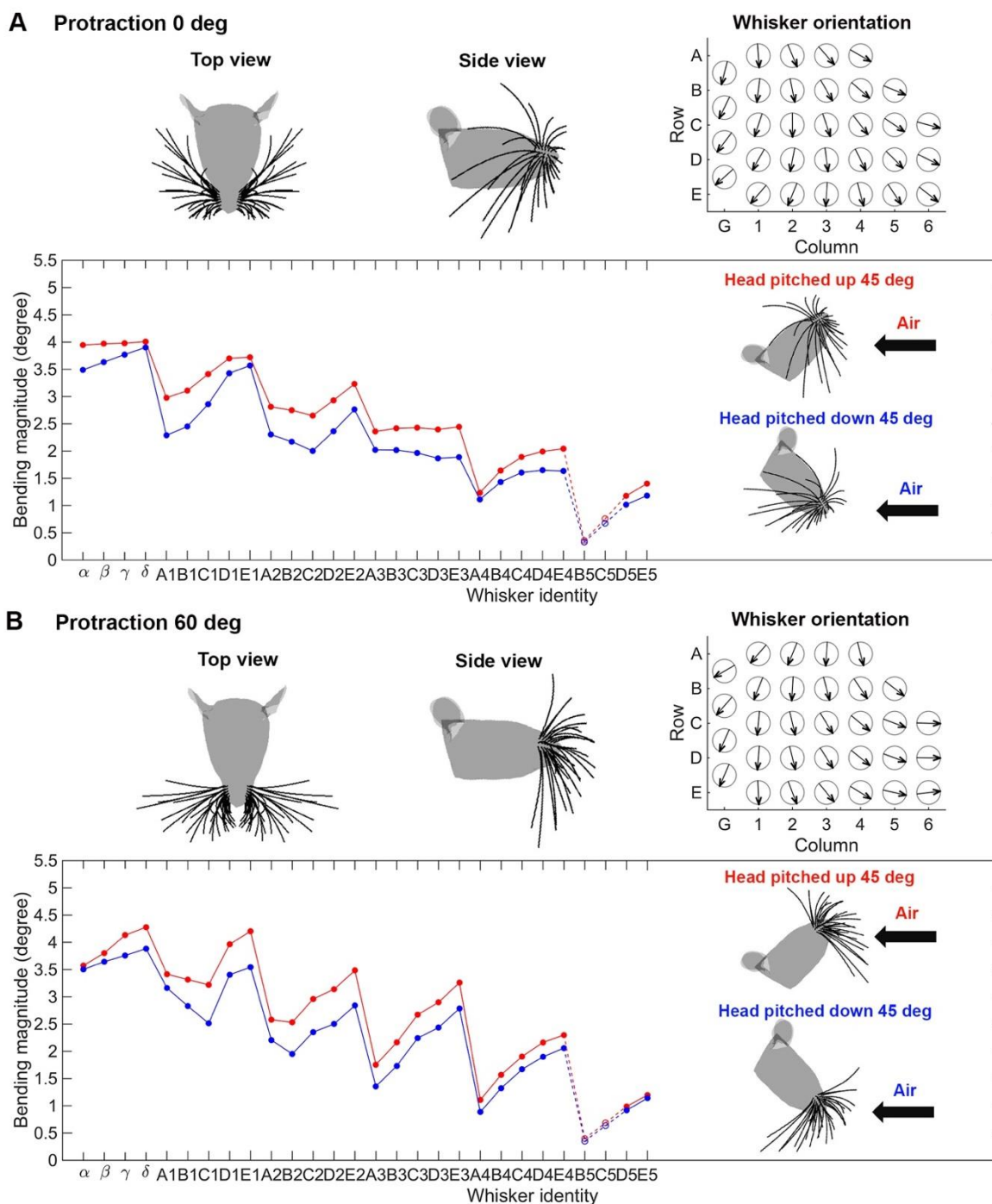


Figure 3.9 The effect of head pitch and whisking motions on the bending magnitude of vibrissae across the array. In both (A) and (B) the figurines provide visual intuition for the configuration of the whisker array at rest in top and side views. The top right graph in both subplots shows the orientation of the intrinsic curvature of each vibrissa, using the same convention as Fig. 3.7B. The arrow in each circle is a direction vector that indicates the concave-forward direction of the

vibrissa's intrinsic curvature. The x-axis in both subplots is linear with column, consistent with the approximately-linear caudorostral spacing of the whiskers on the mystacial pad (Brecht et al., 1997; Towal et al., 2011). **(A)** Predicted bending magnitude at nodes 40% out along each whisker in response to airflow at 3.4 m/s. The vibrissae are simulated to be at rest with the rat's head pitched either up or down by 45°. **(B)** Predicted bending magnitude at nodes 40% out along each whisker in response to airflow at 3.4 m/s. The vibrissae are simulated to have protracted by 60°, with the rat's head pitched either up or down by 45°.

If, as we suggest, the vibrissae play a role in sensing complex flow profiles, then we expect the rat to have the ability to actively probe flow structure by adjusting its sensors. Accordingly, Figs. 3.8 and 3.9 indicate that the rat can change the orientation of its whiskers either via head movements or by whisking. Changing the orientation angles of the whiskers will alter bending magnitudes in complex ways that depend strongly on intrinsic whisker curvature (Fig. 3.5B), which varies systematically across the array. Active exploration of flow structure may help the rat distinguish between externally-generated flow and flow generated by locomotion, typically near ~1 m/s (Arkley et al., 2014).

When taken with the recent discovery that whisking and sniffing are coordinated by the same central pattern generator (Moore et al., 2013), the present work suggests that vibrissotactile sensation may be important to olfactory search behaviors. Neurons in the trigeminal pathway respond strongly to airpuffs, and the present work demonstrates not only that vibrissae are mechanically sensitive to airflow, but also that the rat could actively adjust how the vibrissae respond to airflow. Given that an animal's nervous system coevolves with its ability to move so as to gather particular types of sensory information, the potential anemotaxic role of vibrissae in odor localization could be key to understanding processing in the vibrissotrigeminal system. See Section 5.5 for further discussion.

3.4.7 Vibration magnitude increases along the whisker length and depends strongly on airflow speed and the ratio of whisker's arc length to its base diameter, but only weakly on the whisker's orientation relative to airflow.

As described in *Materials and Methods*, we used high speed video (1,000 fps) to quantify the mechanical behavior of whiskers in response to sustained airflow stimuli. Five whiskers were tested, each identified by their row and column position within the array: E2, α , A2, C2, and D5. The shapes and geometric parameters (arc length S , base diameter D , and S/D ratio) for these whiskers are shown in Fig. 3.10A. Airflow stimuli were delivered at different speeds (approximately 0.5 m/s, 1.4 m/s, 2.2 m/s, 3.4 m/s, 4.4 m/s, and 5.6 m/s) and from different directions (0° , 45° , 90° , 135° , and 180°). The airflow “direction” was defined based on the orientation of the whisker's intrinsic curvature relative to the airflow, with 0° and 180° representing concave forwards and backwards relative to the airflow, respectively, and 90° representing concave upwards relative to the airflow. Discrete positions (“nodes”) along the whisker were tracked at intervals of 2 mm. Linear interpolation between these nodes then yielded the complete shape of the whisker, i.e., the position of each point on the whisker.

If the whisker were a perfectly rigid body, pinned at its base, it would rotate in response to airflow stimulation and would not bend. However, the whisker is flexible, and therefore it both bends and vibrates in response to an airflow stimulus. At each point along the whisker, the bending magnitude (θ_{bend}) can be quantified as the angle between that point on the whisker at rest and the mean position

of that point when the whisker is in airflow. As schematized in Fig. 3.10B, recent work has shown that the bending magnitude increases along the whisker length, so that more distal portions of the whisker rotate through larger angles than more proximal regions (Yu et al., 2016b). The same study showed that the bending magnitude at each node depends strongly on airflow speed, the ratio of the whisker's arc length to its base diameter (S/D ratio), and weakly on the whisker's orientation relative to airflow (Yu et al., 2016b).

We anticipated that similar relationships would be found for vibration magnitude. To test this possibility, we quantified vibration magnitude at each node along the whisker by finding the average angular displacement of the node from its mean position (see *Materials and Methods* for details). Results showed that, just like bending magnitude, vibration magnitude was also greatest at distal, rather than proximal locations along the whisker length (Fig. 3.10B). This result is illustrated for two example nodes on the α whisker in Fig. 3.10C. In this example the whisker was oriented concave forward into the airflow (orientation angle = 0°) and vibration magnitude is plotted as a function of airspeed for nodes at 40% and 80% out along the whisker length. Airspeed strongly drives the magnitude of vibrations at both nodes, but vibration magnitude is always much larger at 80% of the whisker length than at 40% of the length. Similar results were found for all orientation angles and for all whiskers.

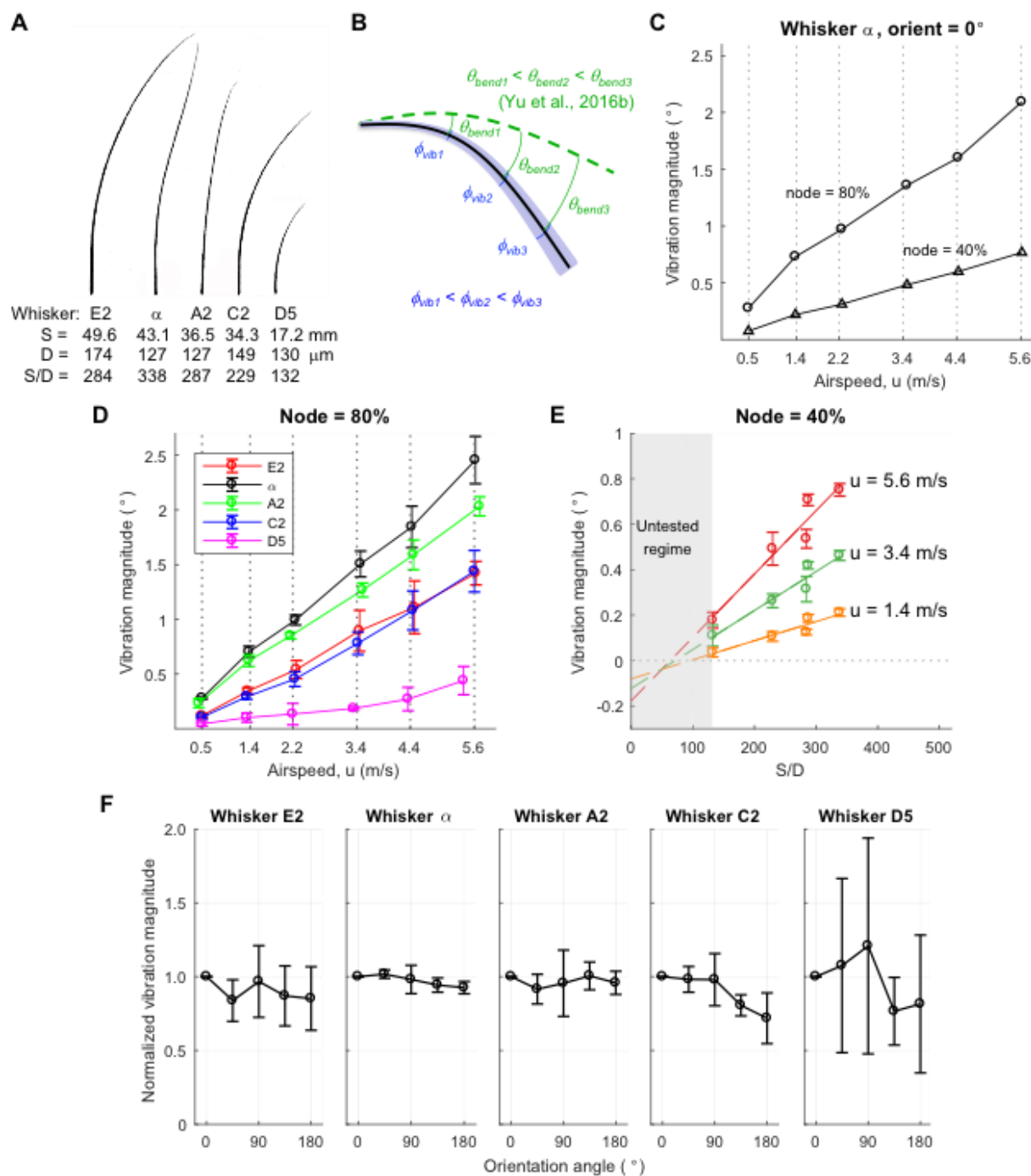


Figure 3.10 Vibration magnitude varies with airspeed and whisker geometry, but only weakly on the orientation of the whisker relative to airflow. **(A)** Five whiskers with different S/D ratios were used in the experiments. A lower S/D ratio means that the whisker is stiffer compared to a whisker of the same length with a higher S/D ratio. **(B)** Schematic of bending and vibration magnitudes. Dashed green curve indicates the position of the whisker at rest (no airflow). Solid black line indicates the mean position of the whisker in the presence of airflow. Blue transparent region

schematizes vibration magnitude around the static bending. For all whiskers in all conditions, we found that $\phi_{vib1} < \phi_{vib2} < \phi_{vib3}$. **(C)** Vibration magnitude is larger at more distal locations along the whisker. The plot shows the vibration magnitude of nodes located at 40% and 80% along the whisker α . In this example, the whisker was oriented concave forward into the airflow, but similar results held for all whiskers at all orientations. **(D)** Vibration magnitude tends to increase linearly with airspeed. Results are shown for nodes 80% out along the whisker length and averaged over all orientation angles. **(E)** Vibration magnitude increases approximately linearly with the S/D ratio of the whisker. Along the x-axis, ordered from small to large S/D ratio, the whisker identities are D5, C2, E2, A2 and α . Results are shown for a node 40% out along each whisker and at airspeeds of 1.4, 3.4 and 5.6 m/s. Linear fits between vibration magnitude and S/D ratio show increasing slopes with airspeed. Because airspeeds were not identical for all five whiskers, values of vibration magnitude have been interpolated between the airspeeds closest to the speed of interest. Note that the S/D ratio for E2 is only slightly smaller than that for A2, so that points for these whiskers are nearly overlaid in the case of $u = 3.4$ m/s. Results for **(D)** and **(E)** show mean \pm SD at five orientation angles. **(F)** The whisker's orientation relative to airflow did not strongly contribute to vibration magnitude. In each subplot, the vibration magnitude has been normalized by that whisker's vibration magnitude at orientation angle 0° (concave forwards, toward the airflow). Results show mean \pm SD at six airspeeds for a node 40% out along each whisker.

The result that vibration magnitude increases with airspeed holds for all whiskers, as shown in Fig. 3.10D. The figure shows that vibration magnitude increases approximately linearly with airspeed, but that the slopes are different for the different whiskers. Again, based on analogy to results for bending magnitude (Yu et al., 2016), we anticipated that the whisker's S/D ratio could have a strong influence on vibration magnitude. This relationship is plotted in Fig. 3.10E, showing that vibration magnitude scales approximately linearly with the whisker's S/D ratio. For visual clarity, results are shown for only three airflow speeds, but the linear trend applies to all tested airflow speeds. It is unsurprising that a whisker with a low S/D ratio will vibrate less than a whisker with a large S/D ratio because the stiffness of a conical whisker scales as D to the fourth power.

The orientation of the whisker relative to airflow was not found to have a strong influence on vibration magnitude. Fig. 3.10F plots the vibration magnitude obtained at each orientation of the

whisker normalized by the vibration magnitude obtained when the whisker was oriented at 0° . Based on one-way ANOVA with repeated measures, it indicated significant differences only for the α whisker ($p < 0.05$) and the C2 whisker ($p < 0.001$). Thus, unlike bending magnitude, which exhibits a clear dependence on whisker orientation relative to airflow, vibration magnitude does not appear to depend strongly on the whisker's orientation angle.

3.4.8 The vibration magnitude scales linearly with the bending magnitude.

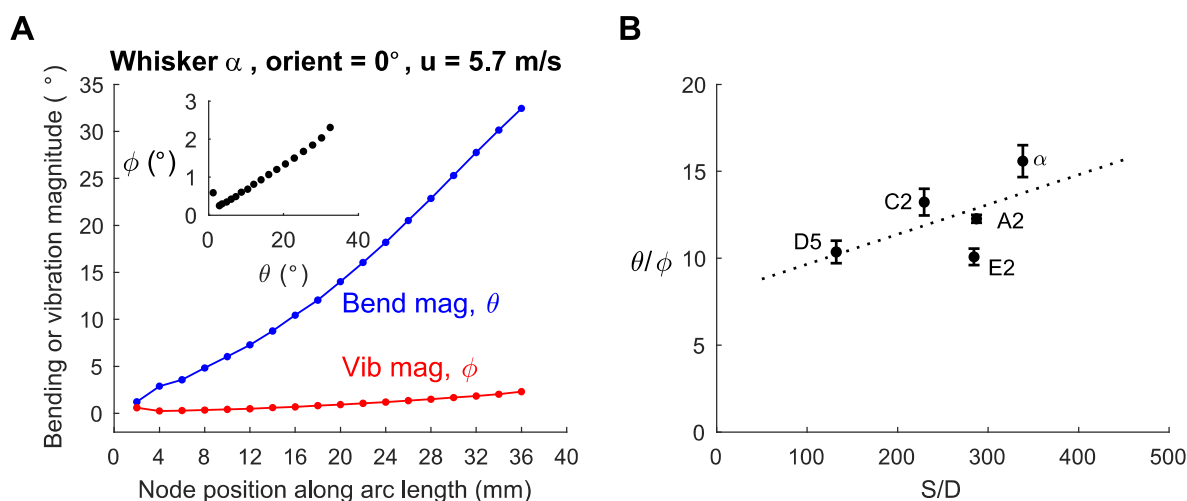


Figure 3.11 Vibration magnitude scales with bending magnitude. **(A)** Bending magnitude and vibration magnitude along the arc length of whisker α at orientation angle 0 deg and airspeed 5.7 m/s. The inset shows vibration magnitude versus bending magnitude of all the nodes of whisker α . **(B)** The ratios of bending magnitude to vibration magnitude (θ/ϕ) of these five whiskers fall within a range of 10 - 16 , and slightly increase with the S/D ratio. Data were shown mean \pm SEM over all whisker nodes at all velocities and all orientation angles.

As previously indicated in Figs 3.5A and 3.10C, both bending magnitude (θ_{bend}) and vibration magnitude (ϕ_{vib}) increase along the whisker length. The bending magnitude defines the static component of whisker deflection in response to airflow, while the vibration magnitude quantifies

the dynamic component. The bending and vibration magnitudes can be conceptualized as the mean and deviation of the deflection, respectively.

We found that bending magnitude is always much larger than vibration magnitude, but that their ratio, θ/ϕ , remains approximately constant at all nodes along the whisker. An example of bending and vibration magnitudes for the α whisker is shown in Fig. 3.11A. As shown in the inset, vibration magnitude scales linearly with bending magnitude along the whisker length.

Similar results were found for all other orientation angles, airspeeds and whiskers, and the θ/ϕ ratios as a function of S/D ratio are shown in Fig. 3.11B. The θ/ϕ ratios of these five whiskers fall between 10-16, increasing weakly with the S/D ratio.

3.4.9 At low airspeed, whiskers vibrate parallel to the airflow direction, transitioning to perpendicular vibration at high airspeed.

Previous work (Section 3.4.2) has demonstrated that whiskers always tend to bend in the direction of airflow, regardless of airspeed, whisker geometry, or orientation of the whisker relative to the airflow. We quantified vibration direction for each whisker by tracking the position of a node located ~80% out along its length.

Results are shown in Fig. 3.12, and reveal that the whisker's vibration direction is much more complex than its bending direction. The top row of subplots in Fig. 3.12A shows the whisker's

vibrations during an airflow stimulus of 0.5 m/s. The position of the tracked node, tracked over time, forms an ellipse with its major axis parallel to the airflow direction. This distribution becomes circular as the airspeed increases to 3.5 m/s (Fig. 3.12A, center row of subplots), and returns to an elliptical shape at a high airspeed of 5.6 m/s, but with the major axis perpendicular to the airflow direction (Fig. 3.12A, bottom row of subplots).

To quantify the degree to which vibrations were parallel or perpendicular to the direction of airflow, we introduce a vibration direction index (*VDI*), defined as the ratio of the count of time points in which the whisker position fell in the first and third quadrants to the count in the second and fourth quadrants. A $VDI > 1$ indicates that a majority of the vibration direction is perpendicular to airflow, and a $VDI < 1$ indicates vibration direction is parallel with airflow direction.

We calculated the *VDI* for all orientations and airspeeds for all five whiskers, as shown in Fig. 3.12B. With the exception of the shortest whisker (D5), vibration direction index increases with airspeed, indicating a shift from parallel vibration to perpendicular vibration as the airspeed increases. Interestingly, whisker α , which has the largest S/D ratio, exhibits a very distinct perpendicular vibration at all airspeeds greater than 2.2 m/s. Although the orientation of the whisker relative to the airflow was found to have some influence on vibration direction, its effects were challenging to quantify: no clear trends were found across whiskers.

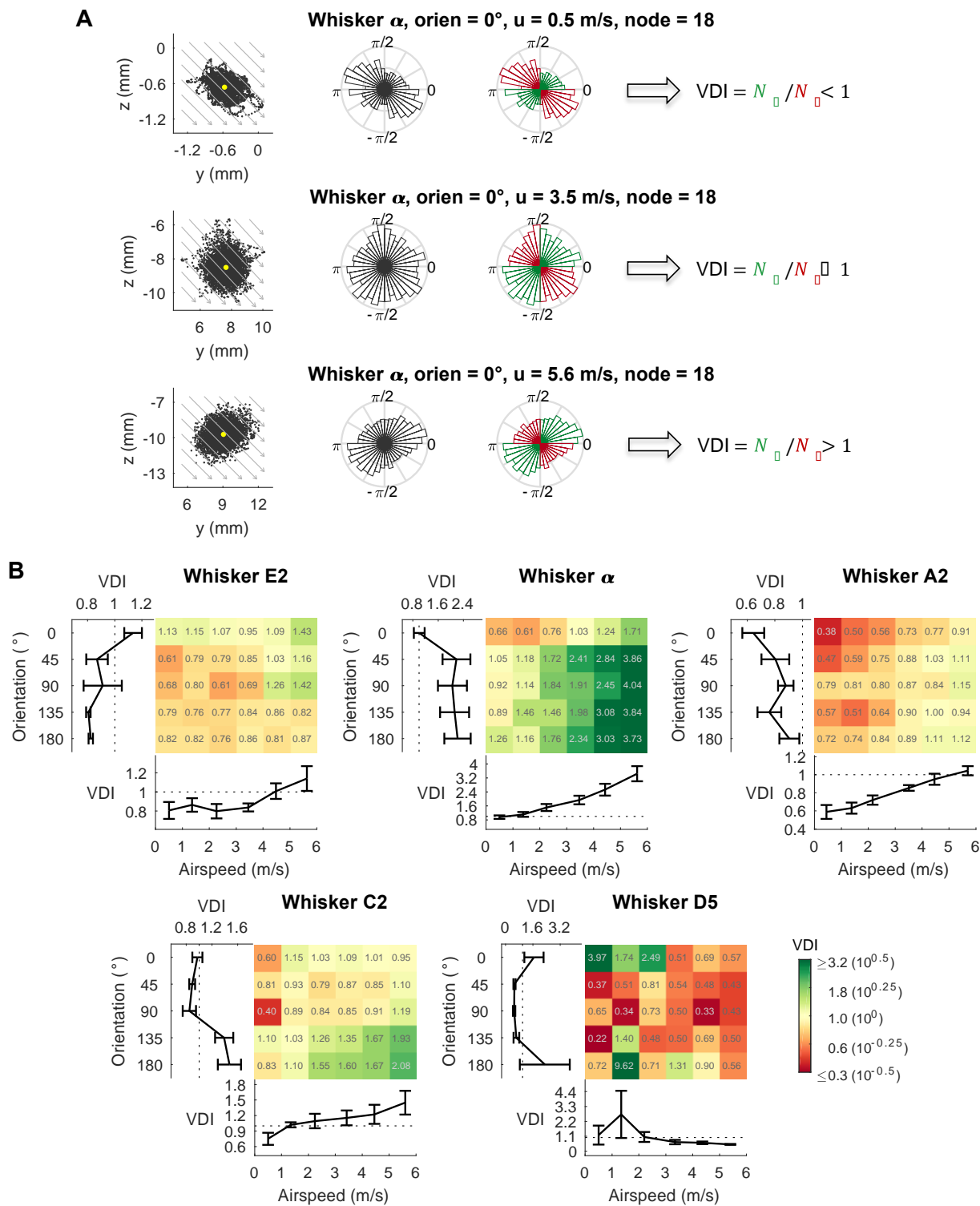


Figure 3.12 Vibration direction tends to be parallel with the airflow direction at low airspeed, and perpendicular to the airflow direction at high airspeed. (A) The airflow-evoked vibration of the α

whisker at an orientation angle of 0° provides one example of the general finding that increases in airspeed are associated with transitions in vibration direction. The three rows of this figure show vibrations that occur for airspeeds of 0.5 m/s (vibration primarily parallel to airflow direction), 3.5 m/s (vibration equally likely in all directions), and 5.6 m/s (vibration primarily perpendicular to airflow direction). Each row contains three subplots. The first subplot in each row shows the distribution of node positions for every time point in the trial (5,000 samples). Gray arrows indicating airflow direction. The second subplot in each row shows the normalized polar histogram of the node positions. The third subplot in each row shows the same normalized polar histogram, but color codes the polar angles of the first and third quadrants in green, and the polar angles of the second and fourth quadrants in red. Vibration direction index is less than 1 in the top row, approximately equal to 1 in the center row, and greater than 1 in the bottom row. **(B)** The vibration direction index VDI at each orientation angle and each airspeed for each whisker at a node around 80% out along the whisker length. The color grid plot indicates the variation of the vibration direction index at each of the six airspeeds and each of the five orientation angles. Note that the colormap legend is log scaled and the value of the vibration direction index for each condition is labeled in each grid. For each whisker, the subplot underneath the color grid plot shows the variation of the vibration direction index with airspeed, and the subplot on the left shows the variation with orientation angle. Data are shown as mean \pm SD.

3.5 Summary

In this chapter, we investigated the mechanical information that rat whiskers can provide about airflow. In these mechanical experiments, sustained airflow at several different speeds was directed at five isolated whiskers with their curvatures oriented differently to the airflow direction. We found that the whiskers bend and vibrate in airflow, and we quantified five mechanical parameters – bending direction, bending magnitude, vibration direction, vibration magnitude, and vibration frequency. Results demonstrated that these mechanical parameters are closely related to airflow direction and speed: (1) bending direction always indicates the airflow direction; (2) bending magnitude and vibration magnitude increase approximately linearly with airspeed and are affected by whisker geometry and orientation relative to the airflow direction; (3) vibration direction is influenced not only by airflow direction, but also, surprisingly, by airspeed; (4)

vibration frequency is associated with the whisker's resonance modes, and can therefore be used to distinguish airflow stimuli from direct touch. During touch, a whisker's vibration frequency depends in complex ways on intrinsic whisker dynamics, the location (along the whisker length) of whisker-object contact, object surface texture, stick-slip, and friction (Ritt et al., 2008; Wolfe et al., 2008a). A summary of these relationship is shown in Fig. 3.13. The mechanics of whisker in airflow *versus* touch will be discussed in detail in Section 5.2.

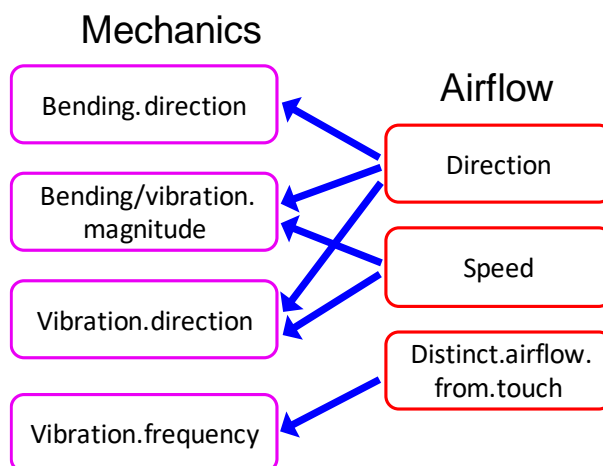


Figure 3.13 Mechanics of whiskers in airflow represent airflow information. Bending direction tells airflow direction, bending and vibration magnitudes correlate directly to airspeed, vibration direction is affected by both airflow direction and speed, and vibration frequency correlated with resonances can be used to distinguish the airflow stimuli from direct touch. Bending direction indicates airflow direction, bending and vibration magnitudes depend strongly on airspeed and weakly on airflow direction, vibration direction is affected by both airflow direction and speed, and vibration frequency correlated with resonances can be used to distinguish airflow stimuli from direct touch.

Chapter 4

Responses of Primary Sensory Neurons in the Vibrissotrigeminal System to Airflow

This chapter was adapted from the manuscript:

Yu, Y.S.W., Bush, N.E. and Hartmann, M.J.Z., Whiskers in the wind: The vibrations of vibrissae and the activity of trigeminal primary afferents in response to a sustained airflow stimulus (in preparation).

We thank Pravin Kumarappan for collecting the neural data presented here.

4.1 Abstract

The rodent vibrissal (whisker) system is commonly studied in the context of tactile perception and sensorimotor integration. We recently demonstrated that rats also use their whiskers during anemotaxis, i.e., when localizing an airflow source (Chapter 2). We also found that whiskers bend primarily in the direction of the airflow; that their bending magnitudes scale with airflow speed; that they vibrate around their new deflected position with vibration frequencies related to their resonance modes; and that vibration magnitude scales with bending magnitude (Chapter 3). In this chapter, we characterized the responses of primary sensory neurons in the trigeminal ganglion (Vg) to a sustained airflow stimulus. We recorded from Vg neurons in anesthetized rats during presentation of an airflow stimulus at different speeds and from different directions. The average firing rate of Vg neurons increases with airflow speed, and depends on airflow direction. Additionally, we showed that the firing patterns of Vg neurons are related to the intrinsic vibration

modes of the whisker. These results described here suggest a possible neural representation for both whisker bending and vibration under airflow stimulation.

4.2 Introduction

Mechanisms for flow sensing and anemotaxis are well studied in arthropods, and in some aquatic mammals. Remarkably, however, no study had investigated the sensory cues used by terrestrial mammals to detect and localize airflow until our two recent investigations (Yu et al., 2016a) (Yu et al., 2016b). These two studies are the first to demonstrate that rats use their whiskers during active behavior to sense airflow (Yu et al., 2016a), and to characterize the mechanical response of whiskers to airflow (Yu et al., 2016b).

The whisker tends to bend in the direction of airflow and vibrates around its deflected position at frequencies close to its resonance modes. The magnitudes of bending and vibration are related to the airflow speed, and the vibration direction was affected by the airflow speed and direction. Air puffs can generate neural response through vibrissae in rats (Kleinfeld et al., 2002; Ganguly and Kleinfeld, 2004; Ollerenshaw et al., 2012), but the neuronal activities stimulated by airflow in the vibrissae system have not been quantified. How the mechanical responses of rat whiskers in the presence of airflow influence the neural coding of airflow information is essentially unknown.

As a first step towards understanding the coding mechanism of neuron to the airflow information, we recorded from vibrissal-responsive primary sensory neurons of the trigeminal ganglion (Vg) in

anesthetized rats while presenting airflow stimuli to the whisker array. Extracellular recordings of single units from the Vg were performed while independently varying the airflow speeds and direction. The airflow was presented at three different speeds, 1 m/s, 3 m/s, and 5 m/s, and from three different direction angles, -45 deg, 0 deg, and 45 deg relative to the animal's head. We correlated the neural activities with airspeed and airflow direction, and compared the spike patterns to the theoretical resonance modes that describe whisker vibration. Results are discussed in the context of a potential role of Vg neurons for encoding the airflow stimuli dictated by the mechanical responses of the whisker in the airflow.

4.3 Materials and Methods

All procedures were approved in advance by Northwestern University's Animal Care and Use Committee. A total of five female Long Evans rats (age ~3 months) were used.

4.3.1 Surgical procedures

Five female Long Evans rats (age ~90 days) were anesthetized with a ketamine-xylazine hydrochloride cocktail delivered intraperitoneally (60 mg/kg ketamine, 3.0 mg/kg xylazine, and 0.6 mg/kg acepromazine maleate). Adequate anesthetic depth was assessed via the toe-inch reflex every fifteen minutes and the observation of whisker twitch through the entire surgical procedure and the recording stage; boosters were administered as necessary to maintain a deep plane of anesthesia. Body temperature was maintained at approximately 37°C using a water-regulated heat

therapy pump (HTP – 1500, Adroit Medical Systems). After exposing the skull, three or four stainless steel screws were placed in the skull over neocortical areas and covered in dental acrylic. This structure was affixed to the surgical bed to maintain head fixation. A small (~1 mm diameter) craniotomy was then performed ~2 mm caudal relative to bregma and ~2 mm lateral to the midline to allow access to the trigeminal ganglion (Vg). A single tungsten electrode (FHC, Bowdoin, Metal Electrode; typical impedance 2–5 M Ω) was lowered to a depth of ~9 mm until multi-unit responses to manual whisker deflections could be heard. The electrode was then advanced slowly until isolated single neuron responses to tactile stimulation of a single vibrissa were obtained. Neural signals were amplified on an A-M Systems (Sequim, WA) four channel amplifier (1000x gain) with analog bandpass filtering between 1 Hz and 10 kHz before digital sampling at 40 kHz using Datawave SciWorks (Loveland, CO).

After isolation of a single vibrissal responsive unit, airflow stimuli were presented and neural responses were recorded. Recorded voltage signals were digitally bandpass filtered between 300 Hz and 8000 Hz before spike identification and sorting with the open-source software *Klusta* (Rossant et al., 2016).

4.3.2 Airflow stimulation

Animals were anesthetized and placed in a custom head-fixation apparatus which allowed free access to all whiskers on the left side of the mystacial pad. A regulated compressed air source was connected to a custom airflow presentation apparatus which was calibrated to direct airflow to the

same point from the 3 directions. Varying the compressed air pressure allowed us to control the airspeed at the center of the vibrissal array.

Airflow was supplied from three directions, -45° , 0° and 45° relative to the lambda-bregma plane, towards the center of the whisker array (Fig. 4.2A). Two protocols were used during experiments. In the first protocol, we measured the airspeed at the center of the array before each stimulus condition (speed/direction combination) and adjusted the position of the airflow source to obtain the expected airspeed at the center of the whisker array. This protocol used two airspeed conditions: 1 m/s and 3 m/s. The second protocol was optimized to increase the amount of data collected by calibrating the airspeed from a fixed apparatus calibrated once before the collection of data (see *Section 4.3.3*). This protocol used 3 speeds (1 m/s, 3m/s and 5m/s). Four neurons were recorded using the first protocol and another four neurons were recorded based on the second protocol.

For each combination of airspeed and direction, we presented the airflow stimuli for 10 trials. A trial consisted of sustained airflow presentation for 15 seconds. A pause of 4 seconds between trials was included to allow the whisker to relax to rest.

4.3.2 Airflow stimulus calibration

All airspeeds were measured using a hot wire anemometer (Omega, model HHF42, resolution = 0.1m/s). To calibrate the airspeeds, the airflow apparatus was fixed in position and an anemometer

was affixed to a 3-axis motorized manipulator (Sutter MP-285). Airspeed measurements were taken from the anemometer at a range of positions for all tested pressures and apparent directions.

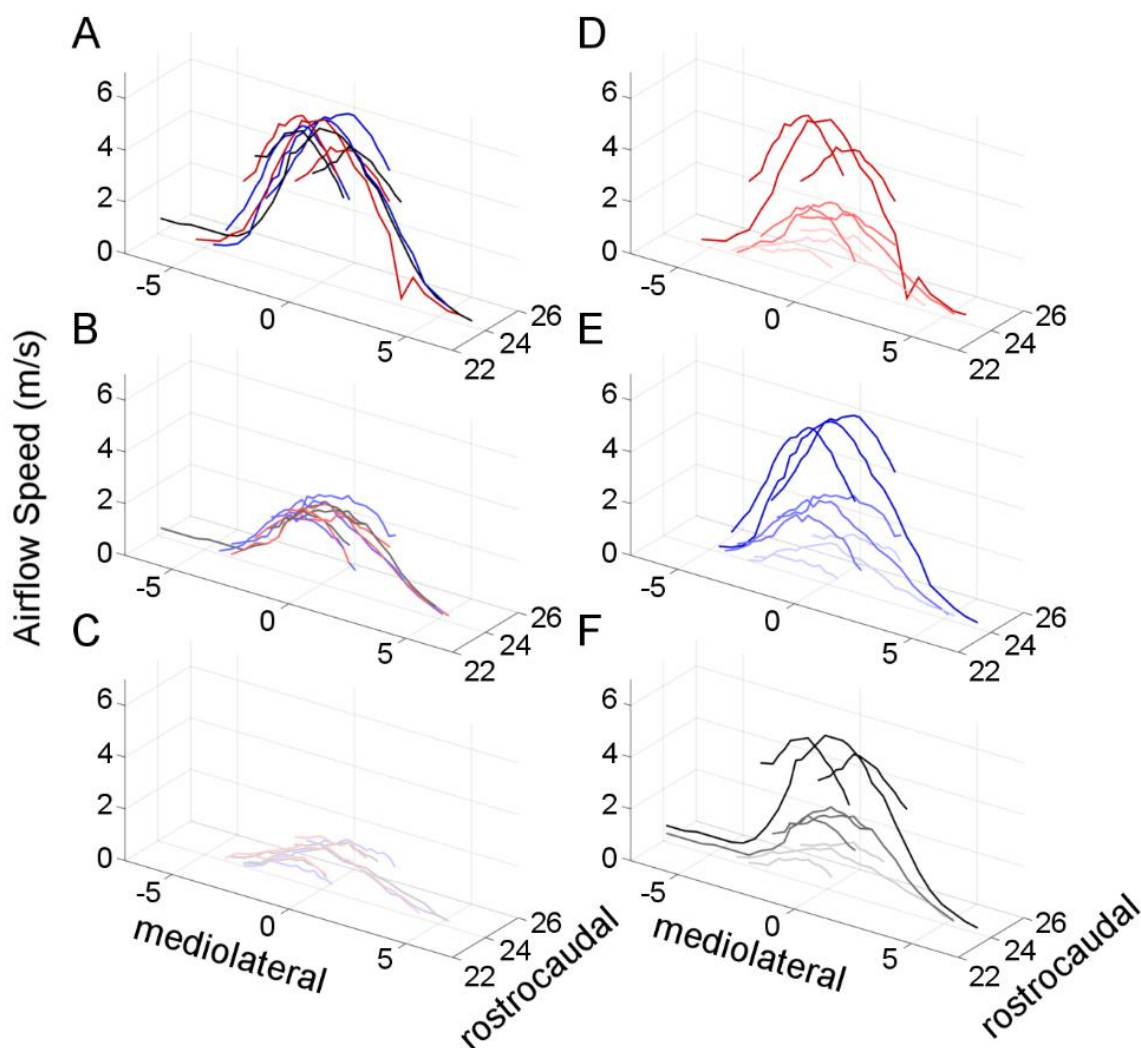


Figure 4.1 Airflow stimulus calibration. Each panel in the left column (A-C) compares the measured airflow speeds for the different directions, keeping supply pressure constant. The overlap at all positions and directions indicated that for each pressure (intended airspeed) there is no bias in wind flow speed across directions. Each panel in the right column (D-F) shows the measurements for a given direction across airspeeds. For all subplots, red, blue and black indicate airflow direction 45 deg, 0 deg and -45 deg, respectively. The saturation of the color represents the magnitude of the airspeed. Dark, medium and light colors indicate 5 m/s, 3 m/s and 1 m/s, respectively. The location (0,0) represents the center of the whisker array. All locations units are in mm.

The airflow map for each combination of speed and direction was obtained and is shown in Fig. 4.1. Each panel in the first column (Fig. 4.1A-C) compares the measured airspeeds for the different directions, keeping supply pressure constant. The overlap at all positions and directions indicates that, for each pressure (intended airspeed) and location, the airspeed is consistent across directions. Each panel in the second column (Fig. 4.1D-F) shows the measurements for a given direction across airspeeds. The airspeed drops off as the mediolateral distance increases. The airspeed drops off as rostrocaudal distance increases, but not so much so that the apparent speed at the anterior region of the whisker array at one pressure is the same as the apparent speed at the posterior region of the array. The airspeed maps at different speed levels are distinct from each other (Fig. 4.1D-F). This allowed us to investigate the effect on the neural response from different airflow directions and airspeeds.

4.3.4 Quantifying whiskers' resonances

The mass of the whiskers was measured using a Mettler-Toledo UMX2 ultra microbalance ($\pm 0.1 \mu\text{g}$). The diameter of base and tip of the whisker was measured at magnifications 10x under a Leica DM750 microscope. Base and tip diameter were obtained from the parabolic fit. After measuring the diameter, the whiskers were scanned on a flatbed scanner (Epson Perfection 4189 Photo) and traced in Matlab[®]. The length of the whisker is then obtained from that trace. Each whisker was approximated as a truncated cone. Density of the whisker was calculated by dividing the mass by its volume. To calculate the theoretical resonant frequencies, we again used the Equation 3.2 and the Young's modulus $E = 3 - 11 \text{ GPa}$ (see Section 3.3.6), which describes the resonance modes

for a fixed-free tapered cantilever beam (Georgian, 1965). In this work, we calculated the first mode of the resonance of the whisker to compare the neural spiking periodicity.

4.4 Results

We begin with examples of Vg activity in response to airflow. All neurons increase their firing rate with airspeed and many exhibit adaptation to the stimulus. The firing rate of Vg neurons was also affected by airflow direction. Interestingly, some neurons' preferred airflow directions change with airspeed. We found that a Vg neuron's firing periodicity was related to the mechanical resonances of its associated whisker. Lastly, a toy model was introduced to interpret how the mechanics of the whisker dictate the neuron's responses.

4.4.1 Neurons adapt over the course of a sustained airflow stimulus

We collected a small set of extracellular recordings from primary sensory neurons of the trigeminal ganglion (Vg) in order to explore whether Vg neurons respond to airflow stimulus, and if they do so consistently with what we might expect given tactile studies. We do not, however, attempt to detail how these neurons might encode airflow stimulus, and leave that to future, more exhaustive work. Since Vg neurons have been shown to be excited only during tactile stimulation, we expect they will respond sharply at the onset of airflow, and cease firing quickly after airflow ends. Since airflow consists of both slow, constant (bending) and fast, changing (vibration) components, we expect Vg neurons to respond throughout the duration of the stimulation regardless of if they were

slowly adapting type or rapidly adapting type. Given what is seen in tactile responses, we would also expect most neurons to be tuned to the stimulus magnitude and direction.

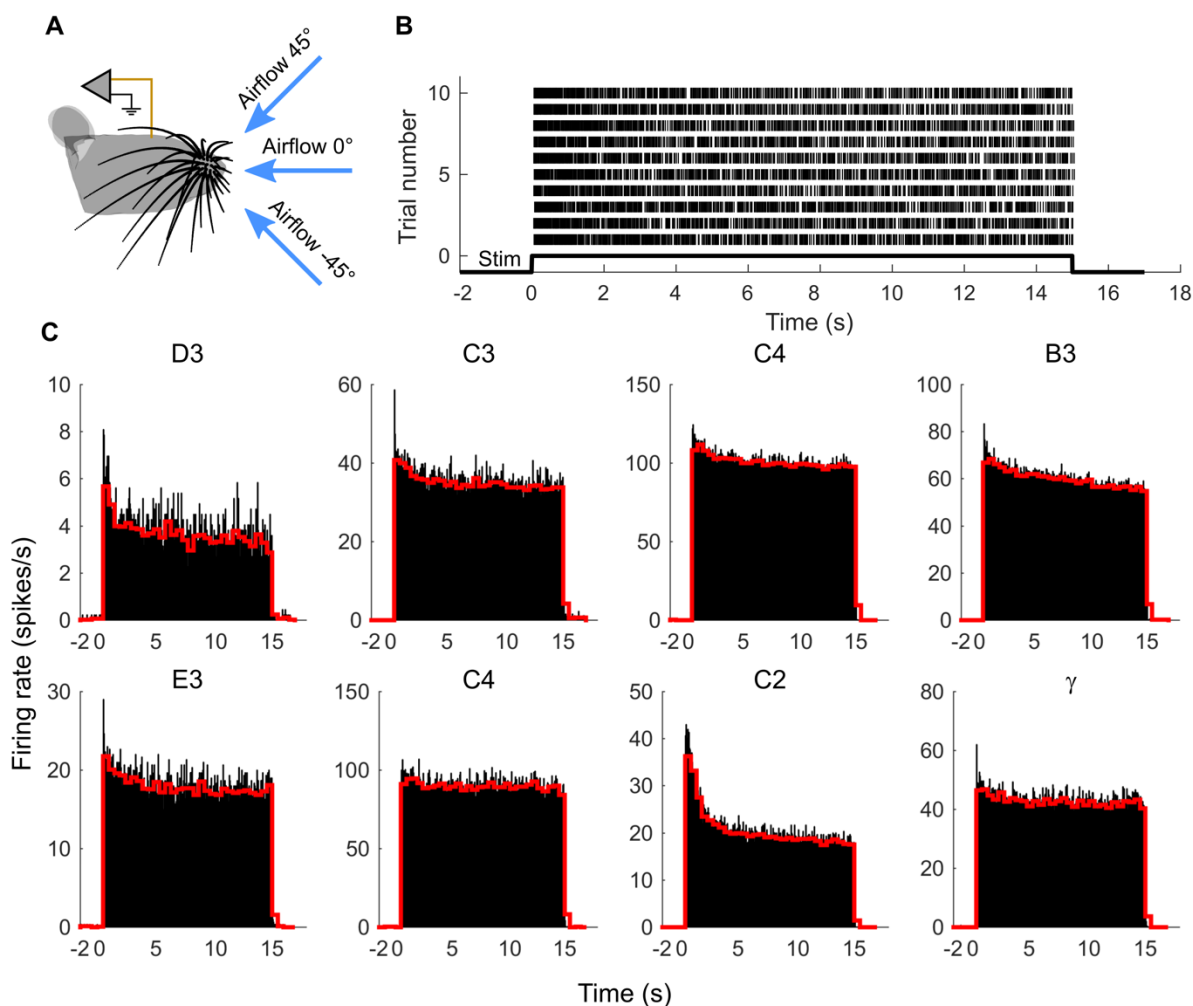


Figure 4.2 Firing rates of Vg neurons during presentation of sustained airflow stimuli. **(A)** For these experiments, airflow direction is defined based on the orientation of the airflow stimulus relative to the rat's head. **(B)** Raster plot of an example neuron innervating whisker C2 for all trials at one condition at one airflow condition with airflow direction at -45° and airspeed at 3 m/s. **(C)** Peri-stimulus time histograms (PSTHs) for all neurons across all trials and conditions. Neurons are identified by the whisker they innervate. Data for neurons in the top row have been averaged over 90 trials that included three orientations and three airspeeds (1 m/s, 3 m/s and 5 m/s), while data for neurons in the bottom row have been averaged over 60 trials that included three orientations but only two airspeeds (1 m/s and 3 m/s). Black histograms have a bin size of 50ms; red histograms have a bin size of 500ms. Whisker C2 is the same neuron shown in **(B)**.

We recorded extracellular responses of Vg neurons to airflow stimulation while varying both airflow direction and airspeed. Note that we define direction now relative to the animal's head rather than with respect to a single whisker. We performed a sequence of 10 trials per combination stimulus of condition (3 directions: $45^\circ, 0^\circ, -45^\circ$ by 2 or 3 speeds: 1 m/s, 3 m/s, [5m/s]; 60 or 90 trials total). Care was taken to align the center of airflow on the center of the whisker array for all stimulus directions and speeds (see *Materials and Methods*). On each trial, airflow was directed for 15 seconds toward the animal's head with an inter-trial interval of 4 seconds. We used high speed video to confirm that 4 seconds was sufficient time for the whisker to return to its resting position (see *Materials and Methods*).

Eight single units innervating eight whiskers in the trigeminal ganglion were obtained from five animals. An example of the spike train obtained from one neuron is shown in Fig. 4.2B, for a single air speed and direction (3 m/s, -45°). This neuron's response exemplifies several characteristics that were observed for all eight neurons. As seen, this neuron starts spiking at the onset and continues to the offset of the airflow stimuli. A high firing rate is associated with stimulus onset. During the inter-trial interval, the neuron is silent. Some evidence for adaptation can be observed from the raster plot for this neuron; a higher firing rate is observed between 0-3 second post-onset than the remaining presentation.

Fig. 4.2C generalizes the results shown in Fig. 4.2B, plotting peri-stimulus time histograms (PSTHs) for all neurons averaged across all trials and conditions. All neurons exhibit a strong response to stimulus onset, fire consistently during airflow stimulation, and are silent in the

absence of stimulation. The neurons presented exhibit a variety of adaptation characteristics, evident on a time scale of <50 ms (large peaks in black histograms (C3, E3, γ)) to several seconds (relaxation of red histograms (C2, C4 (top), E3)). No neuron ceases firing before the end of the stimulus. Many neurons exhibit some level of adaptation to the stimulus, but some do not reach a steady-state even after 15 seconds of sustained stimulation.

4.4.2 All neurons increase firing rate with airspeed

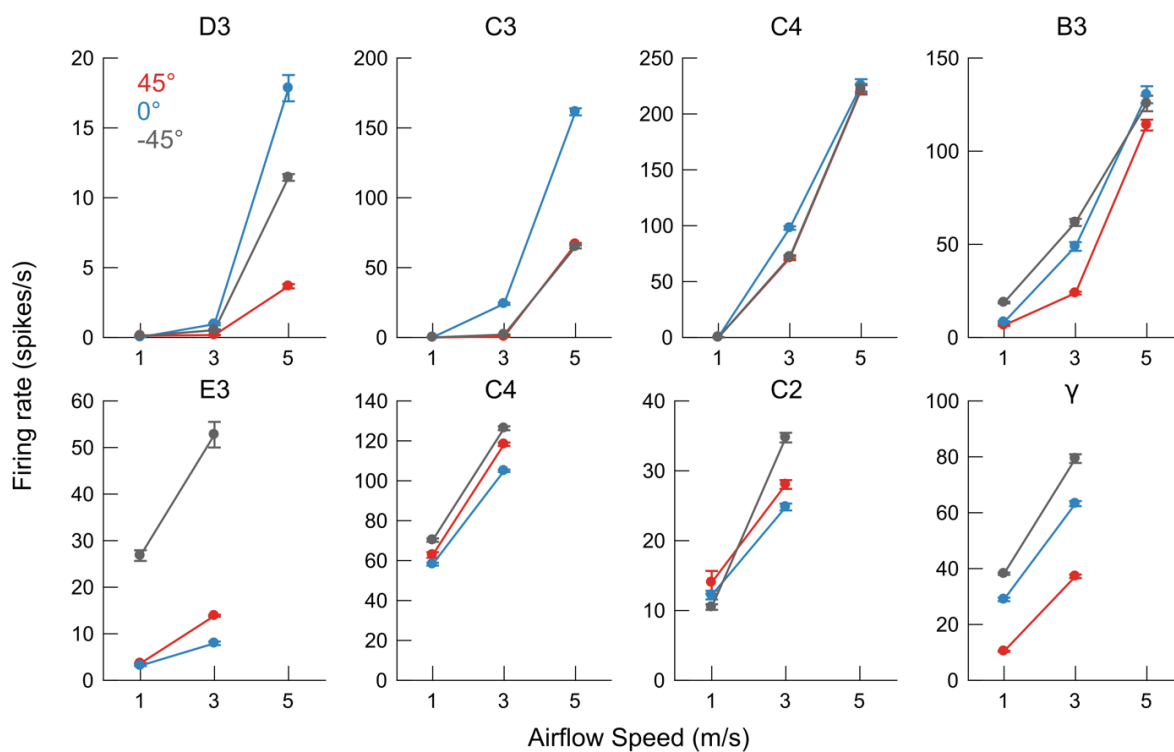


Figure 4.3 Firing rate increases with airspeed. All eight neurons show an increase of firing rate with airspeed. Three airspeeds were used for neurons shown in the top row and two airspeeds were used for neurons shown in the bottom row. Blue, red and black indicates airflow directions, -45° , 0° , and 45° , respectively, as shown in the legend of the first subplot. Data show mean \pm SEM over all tested trials at each condition.

Next, we computed the average firing rates for each trial at each airflow condition. Unsurprisingly, all neurons increase firing rate with airspeed, as shown in Fig. 4.3 (Two way ANOVA: main effect of airspeed $p < 0.001$ for all neurons). It is likely that higher bending and vibration magnitudes of the whisker at higher airspeed result in the higher firing rates. Vg neurons are well known to exhibit strong directional tuning (Lichtenstein et al., 1990; Kwegyir-Afful et al., 2008), and this effect is also evident in Fig. 4.3; each neuron's firing rate depends on the airflow direction (Two way ANOVA: main effect of direction $p < 0.001$; interaction effect of speed*direction $p < 0.001$ for all neurons). The airflow direction in which the neuron exhibited the highest firing rate was termed that neuron's "preferred airflow direction."

4.4.3 Firing rate depends on airflow direction

To observe the effect of airflow direction on the neural response at the same airspeed level, we normalized the firing rate to the maximum mean firing rate. The normalized firing rate variation with airflow direction is shown in Fig. 4.4. From these plots, it is clear that a neuron's firing rate changes with airflow direction. More interestingly, we found that neuron's preferred airflow direction can change with airflow speed. For example, the D3 innervating neuron prefers airflow at $\pm 45^\circ$, and not 0° at low airspeeds, but this relationship is reversed for high airspeeds. This can also be observed in the C2 innervating neuron. Moreover, the modulation depth—the degree to which a neuron shows differential responses across directions—is observed to reduce in some cases as airspeed increases. That is, the preferred direction tuning of the cell weakens as the stimulus magnitude increases. This is seen clearly in the C3, B3, γ , and C4 (top) innervating

neurons. This change in preferred direction could be explained by the observation that the main axis of the vibration direction changes as the airspeed increases. That is, the neuron's preferred direction does not change, but rather as airspeed increases, the whisker vibrates in a different direction, altering the mechanical input to the follicle.

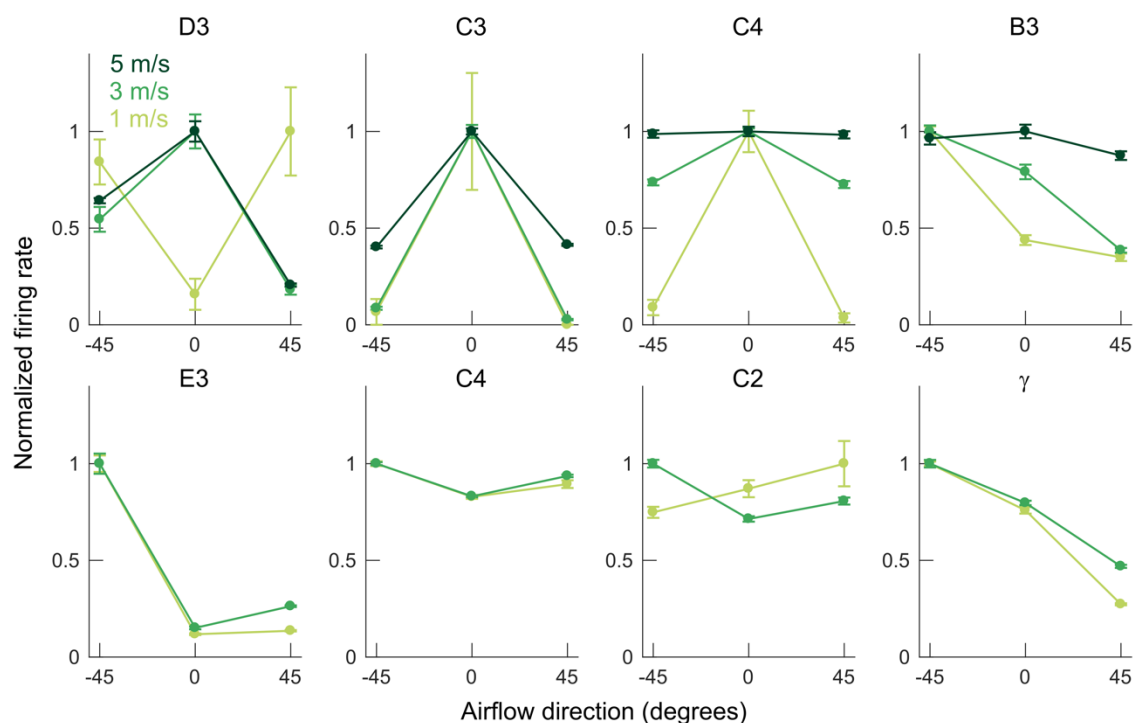


Figure 4.4 Firing rate changes with airflow direction. All eight neurons show a variation of firing rate with airflow direction. Each neuron is identified by the name of the whisker it innervates. The light, medium, and dark green curves indicate slow, medium, and fast airspeed (1, 3, and 5 m/s) as indicated by the legend in the first subplot. Three airspeeds were used for neurons shown in the top row and two airspeeds used for neurons shown in the bottom row. Bottom row shows two airspeed levels based on the preliminary protocol and top row shows three airspeed levels based on the second protocol. Data show mean \pm SEM over all tested trials at each condition. Firing rates are normalized to the maximum mean firing rate for a given airspeed. The absolute firing rates can be seen in Fig. 4.3.

4.4.4 Single unit firing periodicities are close to whiskers' resonances.

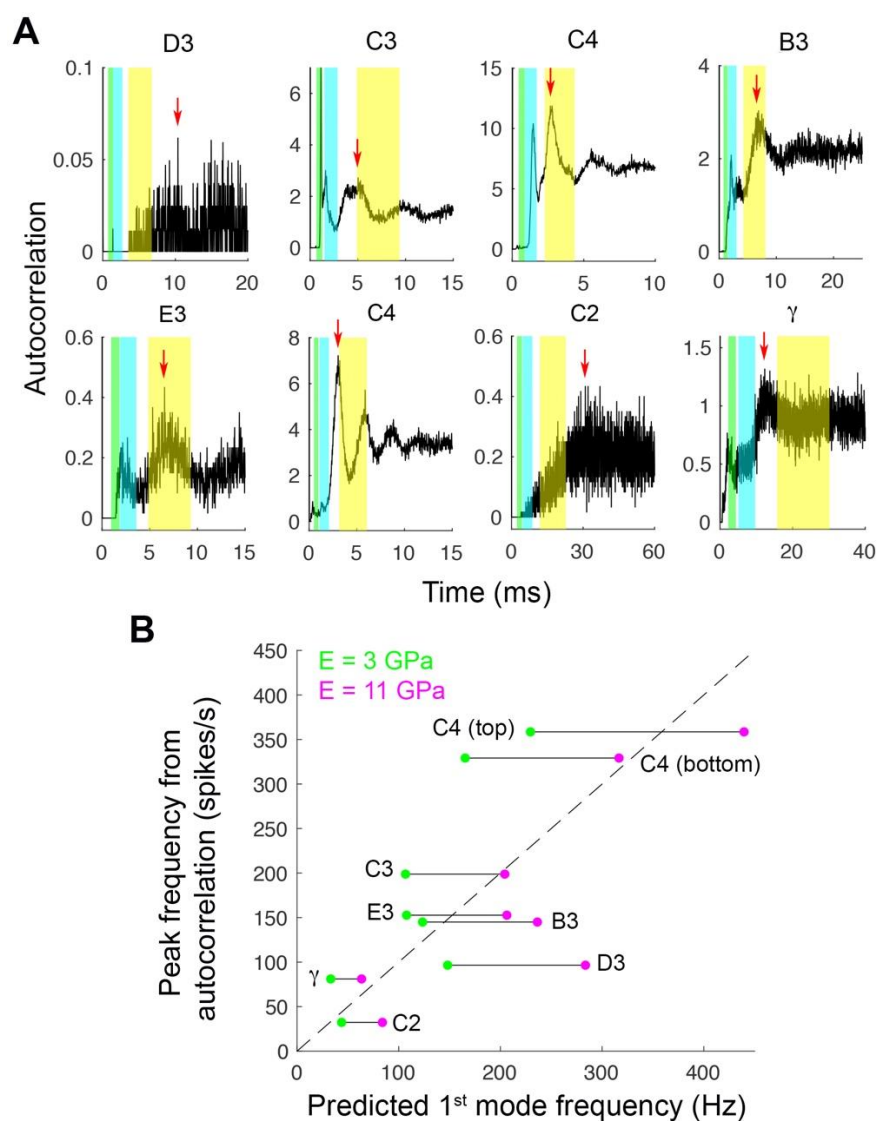


Figure 4.5 Neurons' firing periodicities correspond to whiskers' resonances. **(A)** Autocorrelation of the spike trains for each neuron across all conditions and trials. Shaded regions in yellow, cyan and green represent ranges for 1st, 2nd and 3rd theoretical resonant modes of the whiskers as computed using Young's modulus $E = 3\text{--}11$ GPa, respectively. The peaks of autocorrelation coefficient curves are pointed by red arrows. Note that the abscissa denotes time and the shaded regions indicate the period – the reciprocal of the frequency. **(B)** Relationship between predicted first mode resonance of whisker and observed autocorrelation peak frequency. The dashed line denotes line of equality. Green and magenta dots indicate the predicted first frequency given Young's modulus at 3 GPa and 11 GPa, respectively, and the lines connecting these two dots are the predicted ranges.

We next investigate the patterning of spiking to test whether a neuron could be entraining to the whisker's resonant modes. We computed the autocorrelation of each spike train for each neuron as a measure of spiking periodicity. Fig. 4.5A shows the autocorrelation coefficients of the spike train for each neuron averaged on all conditions and trials. Peaks in the autocorrelation represent common inter-spike intervals, possibly representing a periodic spike pattern. A neuron's firing periodicity could result from its intrinsic cellular dynamics (Hutcheon and Yarom, 2000; Prescott et al., 2008), and/or the periodicity of the mechanical stimuli (Salinas et al., 2000; Fourcaud-Trocme et al., 2003). To see if the observed periodicities in the spike trains correlate with the vibration of the whisker, we computed the theoretical resonances of each whisker that a given neuron innervates (see *Materials and Method*). The first, second and third resonance ranges (using a Young's Modulus range of 3-11 GPa) were superimposed on the autocorrelation curves. The first resonance range (yellow shade) overlaps with the major peak of the autocorrelation curve for many of the neurons.

We then compared the theoretically predicted first mode resonant frequency of the whisker (based on the measured whisker shape and mass) with the peaks found from the autocorrelation curves of the neural spike trains. Results was shown in Fig. 4.5B. Peaks were chosen by finding the maximum autocorrelation coefficients for all neurons except whisker C3 innervating neuron (Fig. 4.5A) for which we chose a peak closest to the first resonance range and the first skewed maximum coefficient might be due to neuron's intrinsic spiking dynamics. Observed spiking periodicities are close to the theoretical whisker resonances. Recall that whisker vibrates at frequencies correlated

with its resonances in the presence of airflow (see Section 3.4.4). This result indicates that the vibrational mechanical stimulus may be driving the temporal patterning of Vg neuron spiking.

4.4.5 A toy model of the mechanical stimulus: the change of vibration direction with airspeed adds complexity into the coding mechanism of Vg neurons.

Bending direction is always parallel to airflow direction and does not change with airspeed (Section 3.4.2), which suggests that mechanoreceptors distributed leeward of the whisker base in the follicle will respond most robustly to airflow. However, the finding that the whisker's vibration direction varies with airspeed complicates this possible neural coding mechanism. We here introduce a toy model of the whisker follicle to examine how airspeed-dependent variations in vibration direction affect the mechanical signal on the mechanoreceptors around the whisker base.

Fig. 4.6 illustrates a mechanical model of the whisker base in the follicle at three airspeeds. Assume that the airflow direction is horizontal. We thus consider two mechanoreceptors (X and Y) arranged perpendicularly with respect to the whisker base, with receptor X leeward (downstream) of the airflow. The effects of whisker orientation relative to the airflow and whisker's geometry are neglected. Suppose that the bending and the vibration of the whisker are represented as mechanical forces: a force due to bending and a force due to vibration, respectively. Bending force represents a "DC (direct current)" component of the stimulus and vibration force defines an "AC (alternating current)" component.

The bending force only acting on receptor X applies for all airspeeds because the bending direction is always in the direction of the airflow, and its magnitude scales with airspeed. Vibration force is a dynamic component which can be decomposed into horizontal (X) and vertical (Y) components. As airspeed increases, the vibration direction changes gradually from parallel to perpendicular. Specifically, at low airspeed (Fig. 4.6A), the vibration force is dominated by the horizontal component; at medium airspeed (Fig. 4.6B), the vertical component became notable and both components are equally important; at high airspeed (Fig. 4.6C), the vertical component dominates the vibration force. Like bending force, the averaged magnitude of the vibration force increases with airspeed.

Neurons' firing rates vary with both airspeed and direction. Suppose that bending was the only response of the whisker in airflow. The neuron's firing rate would only represent the static component of the stimulus with a magnitude dependent on direction and speed. Although the magnitude of the vibration is very small compared with bending, the finding that the periodicity of neuronal firing was close to the resonant frequency of the whisker suggests that vibration may be a relevant coding factor. If vibration were purely random (i.e., without any relationship between speed and direction), it might add noise to neurons' response. In reality, however, vibration direction does carry information about airspeed. In the low airspeed, receptor X would receive more vibration signal than receptor Y; in the medium airspeed, both receptors would receive similar vibration signal; and in the high airspeed, vibration would add more dynamic stimulus into receptor Y than receptor X. This unique stimulus suggests a possible complex coding mechanism in Vg neurons in which both speed and direction information are multiplexed in a single neuron.

Note that multiple neural coding schemes are possible, but the mechanics of the whisker impose a constraint on the possible information available to the Vg neurons during the sensing of airflow.

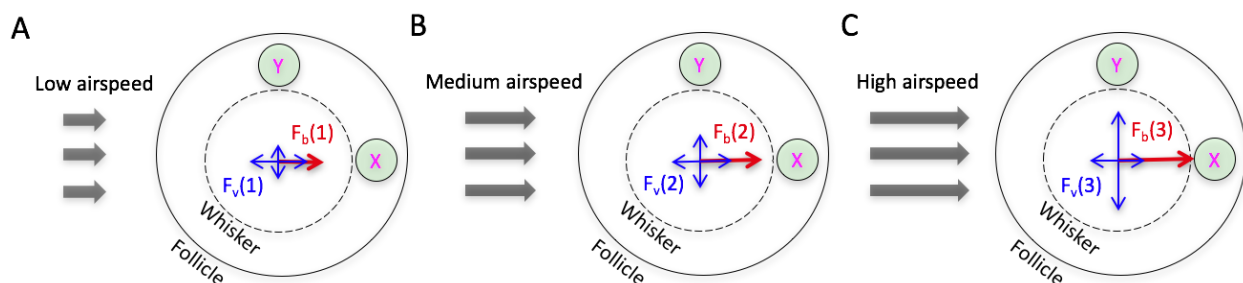


Figure 4.6 The simplified component forces acting on mechanoreceptors in the whisker follicle at different airspeeds. Force due to bending (red vectors), F_b , and force due to vibration (blue vectors), F_v , acting on only two mechanoreceptors, X and Y, are considered at three airspeed levels. **(A)** At low airspeed, the dominated vibration force is in the direction of the airflow and acting on receptor X. **(B)** At medium airspeed, both horizontal and vertical components of the vibration force are comparable in magnitude. **(C)** At high airspeed, the vertical component of the vibration force dominates and acts on receptor Y. Bending forces at these three airspeeds always act on receptor X. The solid circle indicates the boundary of the follicle, and the dashed circle indicates the whisker base in the follicle. Airflow is assumed horizontal. The magnitude of the bending force satisfies $F_b(3) > F_b(2) > F_b(1)$ and the averaged magnitude of the vibration force satisfies $F_v(3) > F_v(2) > F_v(1)$. Note that the scale of the vibration force with respect to the bending force is exaggerated.

4.5 Summary

In Chapter 3, we quantified five mechanical parameters of the whisker's response to sustained airflow: bending direction, bending magnitude, vibration frequency, vibration magnitude, and vibration direction. In this chapter, we describe the activity of whisker-sensitive Vg neurons in response to sustained airflow. Firing rate, preferred airflow direction, and spiking periodicity are quantified based on data from eight single units.

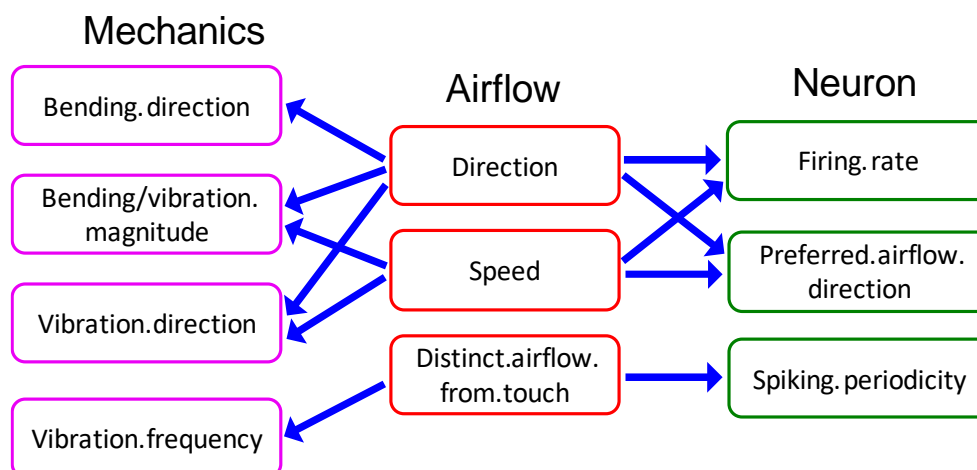


Figure 4.7 Relationships between the whisker's mechanical response, the physical parameters of airflow, and the responses of primary sensory neurons in the trigeminal ganglion.

The neural representations, as well as the mechanics of vibrissae in airflow, allow us to conjecture how rats use their vibrissal-trigeminal system to decode airflow information. The mechanics of the vibrissae, the airflow information, and the neural responses are all decomposed and their relationships were summarized in Fig. 4.7. The mechanics of vibrissae in airflow reveals that bending direction, vibration direction, bending magnitude and vibration magnitude are all related to the airflow direction; bending magnitude, vibration magnitude, and vibration direction are all affected by the airspeed. We speculate that the vibration frequency can be used to distinguish airflow stimuli from direct touch.

In parallel, neural recordings reveal that airflow direction and airspeed affect both the average firing rate and the preferred airflow direction of vibrissal responsive Vg neurons. These neural findings are consistent with the idea that the mechanics of the vibrissae dictate Vg neural representations. Larger bending/vibration magnitudes lead to higher firing rates, the change of

vibration direction with airspeed alters a neuron's preferred airflow direction, and vibration frequency is related to the neural spiking periodicity.

A caveat to the work is that these findings are based on only eight single units. More units are expected to validate and expand on these results.

Chapter 5

Conclusions, review and future work

This chapter was partially adapted from the following two publications:

Yu, Y.S.W.*, Graff, M.M.*, Breese S.C., Man., Y.B. and Hartmann, M.J.Z., Whiskers aid anemotaxis in rats. *Science Advances*, **2**, e1600716 (2016a). *Equal contributions.

Yu, Y.S.W., Graff, M.M. and Hartmann, M.J.Z., Mechanical responses of rat vibrissae to airflow. *Journal of Experimental Biology*, **219**, 937-948 (2016b).

and mainly adapted from the manuscript:

Yu, Y.S.W. and Hartmann, M.J.Z., Rodent vibrissae as flow sensors: comparisons to insect hairs and pinniped vibrissae (in preparation).

This chapter begins by summarizing the behavioral, mechanical, and neural investigations of the role of the rat whisker system in sensing airflow (Section 5.1). We then describe the differences between the whisker's mechanical response during direct touch *versus* airflow (Section 5.2). Next, we compare rat whiskers with the tactile and flow-sensing hairs of arthropods, and with the whiskers of pinnipeds (Sections 5.3 and 5.4). Lastly, a potential role for the rat whisker system in sensing airflow during olfactory search (Section 5.5) and future research directions (Section 5.6) are suggested.

5.1 The vibrissae are multimodal sensors, responsive to both touch and airflow

Although it is common wisdom that terrestrial mammals can sense and follow the wind, the cues that underlie this ability are virtually unstudied. To our knowledge, the only study of anemotaxis in terrestrial mammals investigated the behavior of marsh rice rats (*Oryzomys palustris*) (Schooley and Branch, 2005). Rats were released outdoors at a fixed location but at a random orientation. They moved either upwind or downwind 82% of the time, and rarely moved crosswind. Multiple cues could subserve this behavior, including motion of the fur, thermal signals from glabrous skin, and – as suggested by the present thesis – the macrovibrissae.

The present behavioral experiments (Chapter 2) demonstrate that rat whiskers aid in anemotaxis. A group of five rats was trained to localize an airflow source. With whiskers trimmed, rats can still locate airflow above chance, but dropped significantly in accuracy compared with the original condition that whiskers were intact (Fig. 2.5A). Rats also were found to deviate more from the correct air source location when they failed in the task (Fig. 2.6). In contrast, the control group of three rats trained to localize light instead of airflow did not show decrements in accuracy or increases in deviation (Figs. 2.5A and 2.6). Though many other cues, such as thermal information from the snout, pinnae, and corneas, mechanical cues from other sensory hairs including pelage (fur), tylotrichs and the microvibrissae could aid the rats in localizing the airflow, they did exploit the airflow information from their macrovibrissae, indicating that vibrissae are an important cue, particularly in sensing airflow with low speed because rat with higher accuracy decrement has higher airspeed threshold (Fig. 2.5C) (Yu et al., 2016a).

The mechanical experiments in this thesis (Chapter 3) demonstrate that macrovibrissae respond to airflows as small as 0.5 m/s (Fig. 3.5), certainly sensitive enough to respond to typical air currents on land (Monahan et al., 2011). Furthermore, because most whiskers are oriented concave forward or concave down, the mechanical response to airflow will be amplified compared to a concave

backwards orientation. The macrovibrissae transmit multiple cues about flow velocity: the whisker bends in the flow direction and oscillates around its new static position (Figs. 3.3 and 3.10). The magnitudes of bending and vibration vary systematically with airflow speed, whisker geometry, and the whisker's orientation relative to the airflow (Figs. 3.5 and 3.10), but bending direction is largely unaffected by these parameters (Fig. 3.4). The vibration frequency correlates with whisker's property (Fig. 3.6) and the vibration direction was affected by both airflow direction and airspeed (Fig. 3.13).

The neural experiments described in this thesis (Chapter 4) demonstrate that the whisker-sensitive primary sensory neurons in the trigeminal ganglion respond to airflow stimuli. The neurons' firing rates increased with airspeed, and were affected by airflow direction. The firing periodicity of each ganglion neuron was dominated by the first resonance mode of its associated whisker. Moreover, the preferred airflow direction of the neuron changes with airspeed. These results from the neural investigations correspond to the mechanical findings of whiskers in airflow and reveal that whisker's mechanics helps dictate the neuronal responses to airflow.

Taken together, these results demonstrate that, as is the case for marine mammals (Dehnhardt and Ducker, 1996; Glaser et al., 2011; Grant et al., 2013a) the vibrissae-trigeminal system of rodents can sense both flow and touch.

5.2 The mechanics of rat whiskers in response to airflow *versus* touch

The rodent vibrissal-trigeminal system, which has a well-established role in tactile detection and texture discrimination (Kleinfeld et al., 2006; Jadhav and Feldman, 2010), also contributes significantly to the detection and localization of airflow (Yu et al., 2016a; Yu et al., 2016b). In this

section, we summarize the mechanical responses of rat whiskers to airflow and compare the mechanics of whiskers in airflow with touch.

5.2.1 The mechanical responses of rat whiskers to airflow

Rats often live in burrows and/or enclosed environments where airflow is quite stagnant and diffusion is the primary mechanism for gas exchange (Burda et al., 2007). Once outside, a rat will typically encounter airflows with speeds that range between 0.5 and 5 m/s (Monahan et al., 2011). Experiments in this airspeed range have shown that an isolated whisker (plucked from the animal) will bend and vibrate in response to sustained airflow (Fig. 3.3). The whisker's mechanical response can be quantified with five parameters: bending direction, bending magnitude, vibration magnitude, vibration frequency, and vibration direction.

The first four of these five parameters vary with physical stimuli in a way that makes good intuitive sense. A whisker primarily bends in the direction of the airflow, and the bending direction is mostly independent of airspeed and the orientation of the whisker relative to the airflow (Figs. 3.3 and 3.4). Both bending magnitude and vibration magnitude tend to increase with airspeed, and are also affected by the whisker's geometry, specifically, by the ratio of a whisker's arc length to its base diameter (Figs. 3.5 and 3.10). In addition, bending magnitude can change up to 40%, depending on the whisker's orientation relative to the airflow; the bending magnitude is always largest when the whisker faces concave forward into the airflow (Fig. 3.5). Finally, vibration frequency correlates with the whisker's resonance modes, and is dominated by the first mode

resonance (Fig. 3.6). In general, these findings are consistent with intuitions for how thin cantilever beams will behave in airflow and the results are largely unsurprising.

The vibration direction, however, is more difficult to understand. Vibration direction tends to be parallel to the airflow direction at low airspeed, but transitions to perpendicular to the airflow direction at higher airspeeds. An example of this directional shift is shown in Fig. 3.12A. This figure was created by stimulating the whisker with airflow at three different speeds, and then using high speed video (1,000 frames per second) to track the position of a point on the whisker approximately 80% out along its length. At low airspeed, the cluster of tracked positions forms an ellipse with its major axis parallel to airflow direction; at medium airspeed, this shape is circular, without a preferred direction; at high airspeed, the shape returns to an ellipse, but with its major axis now perpendicular to the airflow direction.

Although this transition in vibration direction was found for four out of five whiskers tested, the physical mechanism underlying the transition is as yet unclear. Perpendicular vibration of a thin beam in fluid flow has been reported in some previous studies (Sainsbury, 1971; Kaneko et al., 2008), and some candidate mechanisms include aeroelastic flutter (Dowell, 1970; Lee et al., 1999; Lucia et al., 2004) and vortex-induced vibration (Khalak and Williamson, 1999; Sarpkaya, 2004; Williamson and Govardhan, 2004).

5.2.2 The mechanical response of a rat whisker to airflow compared to touch

The mechanical responses of vibrissae to airflow and touch differ in several ways, summarized in Table 5.1. The most important differences are the uniformity of bending direction, the distribution of forces along the whisker, and vibration characteristics.

Table 5.1 A comparison of the mechanics involved with airflow and touch on the vibrissa.

		Airflow	Touch
Bending	Direction	Whiskers primarily bend in the direction of the airflow (Yu et al., 2016b).	After making contact with an object, whiskers bend on the object's surface in different directions depending on their kinematic trajectory, their intrinsic curvature, friction, and object geometry (Solomon and Hartmann, 2008, 2010; Hobbs et al., 2016; Huet and Hartmann, 2016).
	Magnitude	Depends strongly on airspeed and whisker's taper, and weakly on whisker's orientation relative to airflow direction (Yu et al., 2016b).	Depends on force magnitude and geometry of whisker-object contact.
Vibration	Direction	Depends on both airflow direction and airspeed.	Vibrations will damp relatively quickly after contact. Vibration frequency depends in complex ways on intrinsic whisker dynamics, object surface texture, the location (along the whisker length) of whisker-object contact, stick-slip, and friction (Ritt et al., 2008; Wolfe et al., 2008b).
	Magnitude	Depends strongly on airspeed and whisker's taper, and weakly on whisker's orientation relative to airflow direction.	
	Frequency	Correlated with whisker's resonance modes (Yu et al., 2016b).	
Force and moment	On whisker	Distributed load	Point load
	In follicle	In theory, the forces and moments at the whisker base could be identical for both airflow and touch even though the whisker shapes are different. This equivalency will occur at a single instant in time, and is only of theoretical interest.	

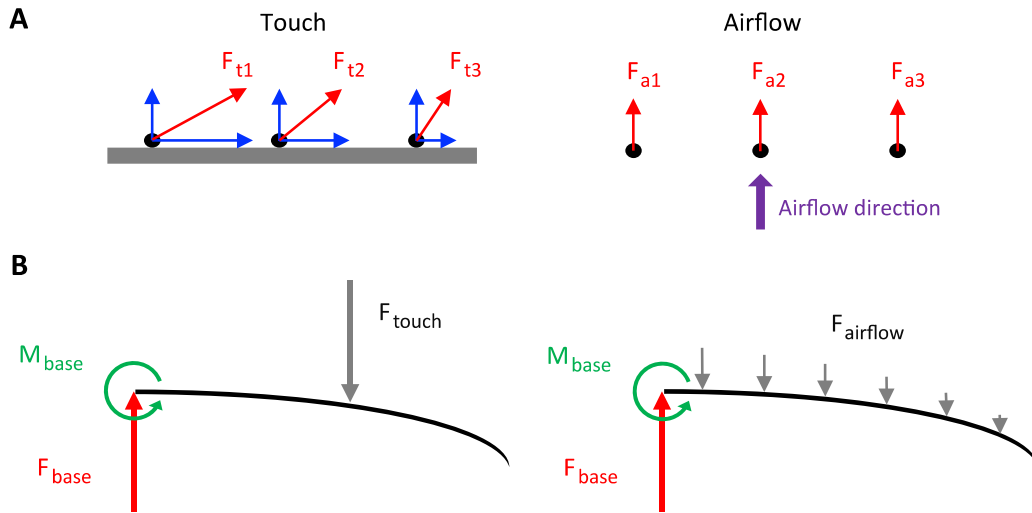


Figure 5.1 The mechanics of rat whiskers in response to airflow. **(A)** The cross-sections of three whiskers are schematized as black circles. In the left panel, the three whiskers touch a flat plane. They experience the same normal force (vertical blue vectors) but different frictional forces (horizontal blue vectors), leading to different resultant force directions and magnitudes (red vectors). The right panel illustrates that the forces generated by sustained airflow (red vectors) are all in the direction of airflow (purple vector). **(B)** Schematics of a point force on a whisker during touch and the distributed forces on whisker during airflow stimulation. In theory, touch and airflow can generate the same force and moment at the whisker base (F_{base} , M_{base}), even though the deflected whisker shape will be quite different. However, this equivalency will last for only a single instant in time.

Uniformity of bending direction: In response to a directional airflow stimulus, all whiskers will bend in approximately the same general direction. In contrast, as the whiskers are actively protracted against an object, they will tend to slip in different directions depending on their intrinsic curvatures, their individual kinematic trajectories, object geometry, and friction (Solomon and Hartmann, 2008, 2010; Hobbs et al., 2015; Huet et al., 2015a), Friction is a particularly important effect during whisker-object contact. In the general case, as the whisker slips on an object, the force normal to the object surface and the frictional force (tangential to the object surface) will change in different ways. The bending direction of the whisker will not necessarily equal the normal force direction. For example, even though two whiskers might initially experience very a

similar normal force direction at the instant when they first touch a flat plane, they will exhibit very different bending directions because of their intrinsic curvature and friction (Fig. 5.1A).

Force distribution along the whisker: The forces generated by the touch of a whisker on an object are generally restricted to a short region along the vibrissal length, and are often well approximated as point load deflections (Birdwell et al., 2007; Solomon and Hartmann, 2011; Quist et al., 2014). In contrast, airflow exerts a distributed load along the whisker length. As shown in Fig. 5.1B, the distributed force from airflow, F_{airflow} , and the point force from touch, F_{touch} , can in principle generate identical forces and moments at the whisker base, even though the shape of the whisker is different. In this case, animals will not be able to distinguish the input signals between touch and airflow based only the mechanical signals at the whisker base. However, this possibility is of only theoretical interest and has no practical relevance, because the deflection associated with airflow will be accompanied by vibrations and the mechanical signals will change at the next instant.

Vibration characteristics and their relationship to bending: Although vibrations will be induced by both touch and airflow, their characteristics will be very different depending on how they are generated. Airflow will tend to cause the simultaneous vibration of all whiskers near their resonance frequencies. To first order, these frequencies are unaffected by airflow speed and direction. The vibrations will be superposed on bending, the vibrations will continue for as long as airflow is sustained, and vibration direction depends in a complex way on airspeed. In contrast, during tactile contact, only the touched whiskers will vibrate, and their vibration frequencies will

depend on intrinsic whisker dynamics, the location (along the whisker length) of whisker-object contact, stick-slip, friction, and object surface texture (Ritt et al., 2008; Wolfe et al., 2008a; Boubenec et al., 2012; Quist et al., 2014). In addition, vibrations will damp as the whisker increasingly presses against the object (Boubenec et al., 2012; Quist et al., 2014; Hobbs et al., 2015). If all whiskers simultaneously deflect past an edge, they will vibrate near their resonance modes, but these vibrations will damp and will not be superposed on a quasistatic bend. Finally, an airflow stimulus will generate a unique relationship between bending and vibrations across the whiskers of the array. Longer whiskers will bend more in response to airflow, but vibrate at lower frequencies than shorter whiskers. Tactile stimuli will not generate such a systematic relationship across the array.

5.3 Comparison with tactile and flow-sensing hairs of arthropods

Air movement sensation is widely investigated in terrestrial arthropods such as the pseudoscorpions, scorpions, mites, spiders, and insects (Humphrey and Barth, 2007). The conspicuous property of arthropods in sensing fluid flow is that they all use hair-like structures with their hair shaft flexibly suspended in the skin or exoskeleton (Humphrey and Barth, 2007). Though vibrissae are also essentially a hair-like structure with vibrissal shaft embedded in a follicle complex, their morphology, function, and response to airflow differ from arthropods hairs in several ways.

5.3.1 Different from bending that occurs in arthropod tactile hairs and rat vibrissae, arthropod flow-sensing hairs rotate as a rigid body in airflow

Unlike vibrissae, which respond to both touch and airflow, arthropods hairs are functionally segregated (Barth, 2004; Dechant et al., 2006). The length of terrestrial arthropod flow-sensing hairs ranges roughly from 100 μm to 2,000 μm (Humphrey and Barth, 2007). Most common length in cricket cerci *G. bimaculatus* was found at about 200 μm (Magal et al., 2006), with extreme values at 1,200 μm (Gnatzy and Tautz, 1980). Tactile hairs are typically longer than flow-sensing hairs, i.e. trichobothria (Fig. 5.2). Properties of tactile hairs on the walking leg tarsus and metatarsus were studied in detail for wandering spider *Cupiennius salei*, with an average length of a tarsal hair (TaD1) at 2.6 mm, and a metatarsal hair (MeD1) at 3.2 mm (Albert et al., 2001). Vibrissae, however, are much longer than arthropods hairs. The lengths of rats macrovibrissae in the caudal area covering the face, critically involved in spatial tasks, are in range between 4 and 70 mm (Belli et al., 2017), up to a few hundred times longer than that of arthropods hairs, and the lengths of rats microvibrissae in the rostral area surrounding the mouth, critically involved in object recognition tasks, are up to 7 mm (Brecht et al., 1997).

One of the other conspicuous differences between the flow-sensing hairs and the tactile hairs in arthropods lies in their responses to mechanical stimuli. Bending is observed in rat vibrissae both in response to touch and airflow. Like rat vibrissae, the arthropod tactile hairs bend when receiving a touch stimulus. The flow-sensing hairs in arthropods, however, rotate – and do not bend – in response to airflow (Albert et al., 2001; Magal et al., 2006; Humphrey and Barth, 2007). This

unique response in arthropods – rotation in airflow and bending in touch – allow us to consider flow-sensing hairs as rigid bodies, while tactile hairs as non-rigid bodies (Fig. 5.2). A rat vibrissae can only be treated as a non-rigid body because its distal region always deflects more than its proximal region (Figs. 3.3 and 3.5A).

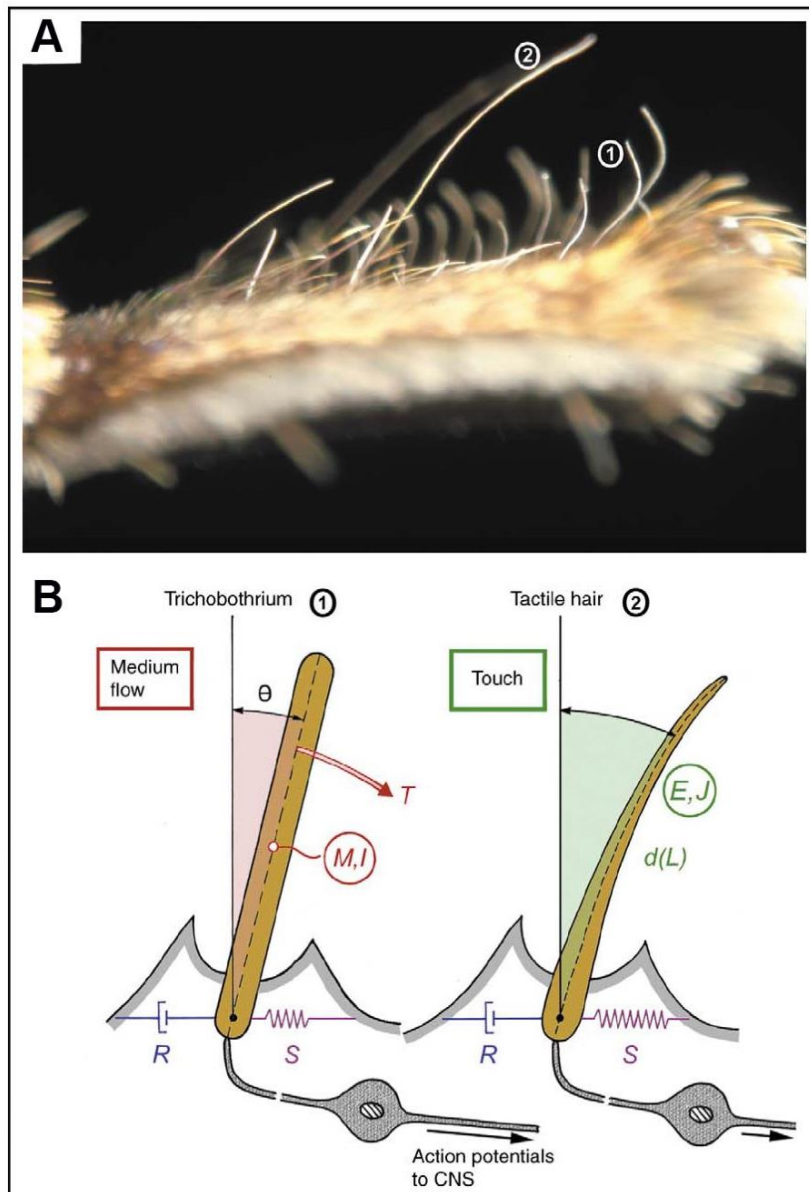


Figure 5.2 Spider flow-sensing hair and tactile hair. (A) Last segment (tarsus) of a spider (*Cupiennius salei*) leg with (1) flow-sensing hair, i.e. trichobothria, and (2) tactile hairs. (B)

Simplified diagram showing the different mechanical responses of these two types of hairs – trichobothria and tactile – to airflow and touch, respectively. Note: T , torque induced by the air flow and deflecting the hair shaft; M , mass of the hair shaft; I , inertia due to M ; R , damping constant; S , torsional restoring constant, like R resisting hair deflection; E , Young's modulus; J , second moment of area; $d(L)$, diameter of hair shaft as a function of hair length. (A) and (B) are adapted from Barth, 2004.

The primary reason why trichobothria of *Cupiennius salei* do not bend in airflow is that the restoring force, which counteracts deflection and drives the deflected hair back to its resting position, is extremely low, with elastic torsional restoring constant S in the order of 10^{-12} N-m/rad, while S in tactile hairs is greater by three to four orders of magnitude (Barth, 2004; Humphrey and Barth, 2007). The Young's modulus, E , of rat vibrissae, is typically within 3-11 GPa (Hartmann et al., 2003; Neimark et al., 2003; Birdwell et al., 2007; Quist et al., 2011; Kan et al., 2013; Yu et al., 2016b), is not very different from arthropods hairs within 0.65-18 GPa (Blickhan and Barth, 1985; Dechant et al., 2001). The area moment of inertia, I , which is proportional to the fourth power of diameter, however, results in a large difference in bending stiffness – the product of Young's modulus and area moment of inertia, EI – between these two hair-like structures due to their disparity of shaft diameter: rat vibrissae base diameter is within 40-250 μm (Belli et al., 2017) and arthropod hair diameter is around 10 μm (Barth, 2004).

5.3.2 Arthropod hair shaft-socket *versus* rat vibrissae shaft-follicle

The way that hairs are embedded in arthropods differs from rat vibrissae. The arthropod hair shaft forms a simple lever with its long arm exposed to the fluid flow receiving mechanical input and its short arm coupled to the sensory cells transforming mechanical input into neural signal. The

length relation between the outer and inner lever arm is large, reaching ratios of more than 1000:1 (Humphrey and Barth, 2007). This ratio will lead quite small displacement of the inner shaft: a displacement of the outer hair shaft of 1 deg can cause the inner end of the short lever arm to move by 30 nm in the cercal hairs of the cricket *Gryllus bimaculatus* (Gnatzy and Tautz, 1980). The inner shaft of cricket (*Gryllus bimaculatus*) cercal filiform hair is embedded in a socket, and the inner shaft of spider (*Cupiennius salei*) trichobothrium is within a cuticular cup – both are held loosely (Gnatzy and Tautz, 1980; Barth, 2002, 2004), being another reason why flow-sensing hairs rotate, instead of bend, in response to the airflow. In contrast, each vibrissa is held tightly at its follicle – whisker and follicle might form a rigid joint, different from the non-rigid external part of the vibrissae (Bagdasarian et al., 2013). The vibrissal shaft inside the follicle is much longer than the inner shaft of arthropod hair, and the vibrissal-follicle complex has much more receptors than the arthropod hair-socket complex, which allows the vibrissae to receive much richer mechanical input of the airflow or touch than arthropod hairs (Rice et al., 1993; Hartmann, 2001; Hartmann et al., 2003; Barth, 2004; Humphrey and Barth, 2007; Huet et al., 2015b; Hobbs et al., 2016; Huet and Hartmann, 2016). In addition, the follicles were wrapped by papillary muscles (Rice et al., 1993), allowing rats to move their vibrissae, *a.k.a.* whisking, to actively sense the environments, by which rat vibrissae stand out from arthropod hairs in another aspect.

Like rat vibrissae, intrinsic curvature is seen in arthropod hairs, and it leads to mechanical directionality (Barth et al., 1993; Yu et al., 2016b). Hollowness, namely medulla for vibrissae, were found both in arthropod hairs and rat vibrissae, which leads to little effects on their mechanical responses to stimuli but reduces mass (Fletcher, 1978; Barth et al., 1993; Humphrey

et al., 1993; Belli et al., 2017). In rats, the shape of the vibrissae can be modelled as parabola with rostral vibrissae concaving forward and caudal vibrissae concaving downward. The surface of the rat vibrissae looks smooth, and these vibrissae are sparsely and orderly distributed, with about 30 macrovibrissae on each side of the face (Towal et al., 2011; Belli et al., 2017). However, in the case of the spider *Cupiennius salei*, trichobothria are commonly curved along, approximately, the distal third of their length towards the proximal end of the leg (Barth et al., 1993), which are very much like hooks (Fig. 2.1). The surface of the trichobothria are densely packed short branches along the entire hair shaft (Barth et al., 1993; Barth, 2002). On each leg, the spider has about 90-100 trichobothria (Barth et al., 1993; Barth, 2004), much denser than rat vibrissae. Such a high density of hair distribution significantly reduced flow speed and increased the phase difference between the far-field flow and the flow between hairs (Casas et al., 2010). In other subfamily of spiders, non-hook curvatures, smooth surface, and other spacing were seen in trichobothria (Guadanucci, 2012).

5.3.3 Rich mechanical responses give rise to a variety of functions between arthropod flow-sensing hairs and rat vibrissae

Because the vibrissae are long their mechanical response is unaffected by the boundary layer around the animal's face, and their large spacing precludes viscous coupling. Given that airflow speed between 0.5-5 m/s is ethologically relevant to rats (Yu et al., 2016a; Yu et al., 2016b), the Reynolds number (Re) for isolated rat macrovibrissae is between 10-100. In contrast, most flow-sensing hairs on arthropods are short and the airflow speed that the animal encounters is low,

leading to a quite low Reynolds number, below 1 (Casas and Dangles, 2010). This indicates a typical viscous flow and arthropod hairs, particularly those of 1 mm or shorter, will be completely immersed in the boundary layer, whose thickness depends on flow oscillation frequency generated by the prey or predator (Casas and Dangles, 2010). Thus the hairs will respond maximally to oscillating flow that generates a boundary layer thickness equal to the hair length, instead of responding directly to flow velocity (Humphrey and Barth, 2007). In addition, the mechanical response of some (though not all) arthropod hairs is subject to viscous coupling (Humphrey et al., 1993; Magal et al., 2006; Dangles et al., 2007; Humphrey and Barth, 2007; Bathellier et al., 2012), particularly among the more closely spaced shorter hairs on the cricket cercus (Cummins et al., 2007), further complicating the relationship between maximal response and flow speed. Finally, arthropod hairs do not simply vibrate at their resonance frequencies because of the weak restoring force of the socket and the driving frequency by the oscillated airflow, and their maximum deflections are restricted by the physical properties of the airflow and the hair (Humphrey and Barth, 2007; Bathellier et al., 2012).

These comparisons highlight the wide variety of functions for flow sensors. In both air and water, flow sensors are used in rapid detection behaviors (Barth et al., 1995; Barth, 2002; Shimozawa et al., 2003), oriented escape (Jacobs, 1995; Catania, 2009), directional navigation (Casas and Dangles, 2010; Reep et al., 2011), odor following (Reidenbach and Koehl, 2011) and complex perceptual investigation of flow profiles (Dehnhardt et al., 2001). The geometry of a flow sensor is expected to match its function and to exploit a tradeoff between response reliability and spatial specificity. For example, if hairs are viscously coupled, a larger number of hairs will respond to a

flow stimulus but at the expense of single hair precision. The morphology of arthropod flow-sensing hairs is well suited to facilitate rapid detection and escape. For rat vibrissae, vibration superposed on bending can provide cues about flow distinct from the sense of touch. Therefore, vibrissae are specifically involved in sensing complex flow profiles for anemotaxis (Yu et al., 2016a), similar to vibrissal-based hydrodynamic trail following in pinnipeds (Dehnhardt et al., 2001; Glaser et al., 2011; Miersch et al., 2011).

5.4 Comparison of vibrissae in pinniped and rodent

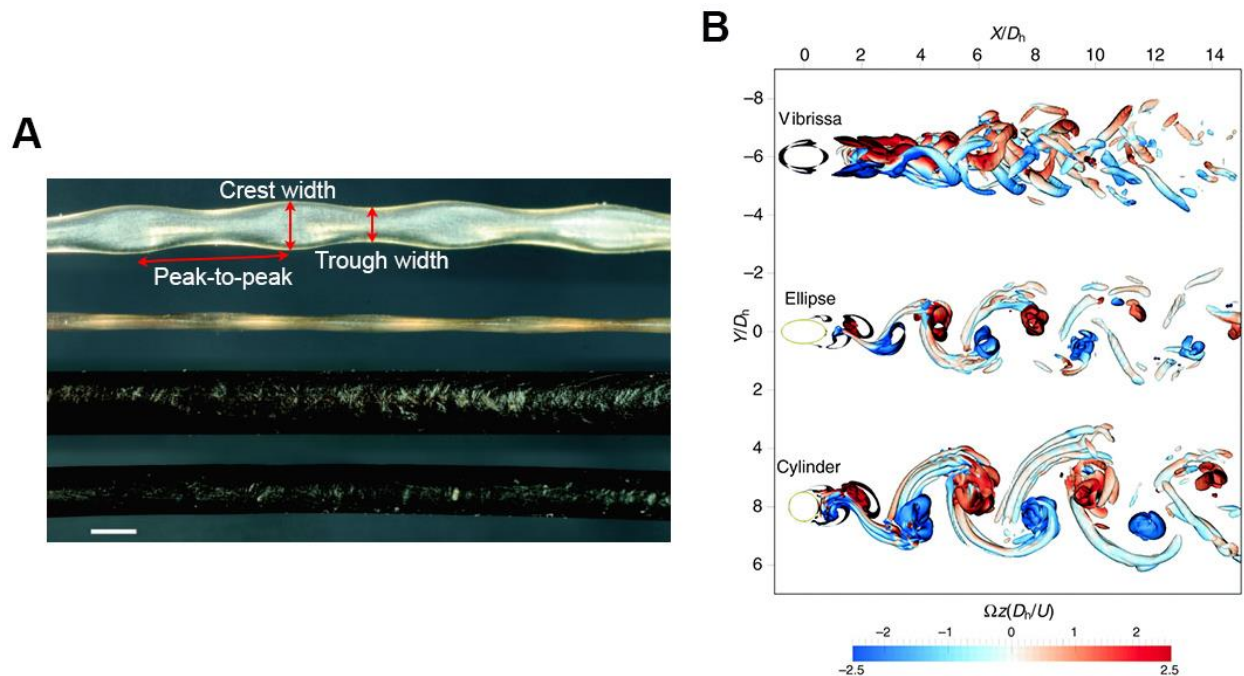


Figure 5.3 Undulated shape of vibrissae suppresses vortices. (A) Structure of a harbor seal vibrissa and a California sea lion vibrissa. From top to bottom: harbor seal vibrissa in dorsal view, and in frontal view, sea lion vibrissa in frontal view, and in dorsal view. Scale bar: 1 mm. (B) Simulated vortices behind three different cylinder bodies – an undulated vibrissa, a circular cylinder and an elliptic cylinder – at $Re = 500$ under the same hydrodynamic diameters, D_h , and the same velocity, U . Color indicates the magnitude of cross-stream vorticity (Ω_z). Modified from Hanke et al., 2010.

Table 5.2 Comparison of vibrissae in pinniped and rodent

	Pinniped vibrissae in water	Rodent vibrissae in air
Length	Between 10-100 mm with mean value 30-40 mm, and increases from rostral to caudal for harp, hooded, gray and bearded seals (Marshall et al., 2006; Ginter et al., 2010; Ginter et al., 2012; Hanke et al., 2013).	Between 4 and 70 mm for rat vibrissae (Belli et al., 2017).
Base diameter	0.7-1.1 mm for bearded seal vibrissae (Marshall et al., 2006), ratio of base diameter to length is around 0.01 for harbor seal vibrissae (Hans et al., 2014).	Between 40-250 μm for rat vibrissae (Belli et al., 2017).
Taper, medulla and orientation	Vibrissae taper from base to tip (Hans et al., 2014; Ginter Summarell et al., 2015). Cavity in harbor seal vibrissae (Hans et al., 2014).	Radius slope (base radius divided by arc length) of rat vibrissae is $1.7\text{-}2.2 \times 10^{-3}$, conical shape of medulla (hollowness) in vibrissae (Belli et al., 2017). Concave forward and downward in the rat mystacial vibrissae pad (Towal et al., 2011).
Surface structure	Undulated for Phocidae such as harbor seal, smooth for most Otariidae such as California sea lion (Hanke et al., 2010; Ginter et al., 2012).	Smooth (Belli et al., 2017)
Density and Young's modulus	Young's modulus 4-30 GPa (Hans et al., 2014; Ginter Summarell et al., 2015).	Density 1.1-1.3 mg/mm^3 (Quist et al., 2014; Yu et al., 2016b), Young's modulus 2-15 GPa for rats (Quist et al., 2011; Carl et al., 2012).
Vibration frequency	Depends on both whisker's property and hydrodynamic conditions (Ginter et al., 2010; Hans et al., 2014; Beem and Triantafyllou, 2015; Ginter Summarell et al., 2015).	Mainly depends on whisker's property (Hartmann et al., 2003; Yan et al., 2013; Yu et al., 2016b). Natural frequency mostly ranges from 25-350 Hz.
Whisking	Pinnipeds do not whisk but their mystacial vibrissae are mobile. Protract vibrissae forward and keep them in position during touch or flow sensation (Miersch et al., 2011).	Rat whisk at 5-25 Hz (Welker, 1964; Carvell and Simons, 1990).
Follicle-sinus complex (F-SC)	In general, pinniped and rodent F-SCs are similar. But the structure of blood sinus and the way the deep vibrissal nerve of pinnipeds penetrating the follicle are different, and pinniped have larger number of myelinated axons per F-SCs than rodents (Marshall et al., 2006).	

Like rodent vibrissae, the functions of fluid flow sensation and direct touch has been found in pinniped vibrissae. The direct touch of vibrissae, i.e., size and shape discrimination, was largely studied in both rodents and pinnipeds. Pinnipeds are mostly marine mammals, and their vibrissae play a crucial role in sensing water movements generated by prey fish or by conspecifics (Dehnhardt et al., 1998; Dehnhardt et al., 2001; Hanke et al., 2010). In contrast, most rodents live on land and their vibrissae partake in airflow perception. The similar functions of touch and flow-sensing, in different dwelling environments, i.e. water *versus* air, are likely contributed by the vibrissae morphologies and mechanical properties in these two mammals. This section aims to compare the vibrissae in pinniped with the vibrissae in rodent. Several comparisons of vibrissae in pinniped *versus* rodent are summarized in Table 5.2.

5.4.1 Morphology and properties of vibrissae in pinniped *versus* rodent

Pinniped vibrissae that emerge from the snout are called mystacial vibrissae, from above the eyes are called supraorbital vibrissae, and from above the nares (nostrils) called rhinal vibrissae (Ginter et al., 2010; Miersch et al., 2011; Hanke et al., 2013; Ginter Summarell et al., 2015). Like rodent vibrissae, pinniped vibrissae are organized in rows and columns, and are generally symmetrical on each side (Dehnhardt, 1994; Dehnhardt and Kaminski, 1995; Knutsen et al., 2008; Towal et al., 2011). The number of mystacial vibrissae varies in species: the average numbers of mystacial vibrissae per side are 122 for bearded seals (*Erignathus barbatus*), 38 for harp seals (*Pagophilus groenlandicus*), 32 for hooded seals (*Cystophora cristata*), 25 for gray seals (*Halichoerus grypus*) (Marshall et al., 2006; Ginter et al., 2010; Hanke et al., 2013). Pinniped vibrissae are generally

larger than rodent vibrissae. Overall length of pinniped vibrissae is between 10-100 mm with mean \pm SD values as: 39.3 ± 17.3 mm for harp seals, 33.4 ± 16.8 mm for hooded seals, and 37.8 ± 13.1 mm for gray seals (Ginter et al., 2010; Ginter et al., 2012; Hanke et al., 2013). Length of pinniped vibrissae increases from rostral to caudal – for example, mean \pm SD values of bearded seals at rostral, middle and caudal are 8.2 ± 3.92 mm, 30.3 ± 9.69 mm, and 81.8 ± 31.5 mm, respectively (Marshall et al., 2006).

An important key difference between rodent and pinniped vibrissae is in their surface structure, or shape. The cross section of rodent vibrissae is generally round, and its area smoothly reduces from base to tip. Like rodent vibrissae, pinniped vibrissae have intrinsic curvature and taper from base to tip, which results in a decrease of moment of inertia from base to tip allowing the tip to bend more easily than the base (Hans et al., 2014; Ginter Summarell et al., 2015). Some pinniped vibrissae, such as bearded seal, fur seal and sea lion, have a nearly round cross section and smooth taper from base to tip. The maximal and minimal diameters of the pinniped vibrissae shaft are on average at 1.1 mm and 0.7 mm for bearded seals (Marshall et al., 2006), and the ratio of base diameter to length are mostly around 0.01 (up to 0.05 for short vibrissae) for harbor seal (*Phoca vitulina*) vibrissae (Hans et al., 2014). However, many pinniped vibrissae, such as harp, harbor, ringed, spotted and gray seals, possess an undulated shape (Fig. 5.3A), also sometimes called a “beaded,” or “waved” shape, with an elliptic cross section and bead density at ~ 2 beads/cm along the length (Ginter et al., 2010; Hanke et al., 2010; Ginter et al., 2012; Murphy et al., 2013; Ginter Summarell et al., 2015). The peak-to-peak distance, the crest width, the trough width (Fig. 5.3A)

and the ratio of crest width to trough width of the undulated vibrissae, are on average between 3.2-4.1 mm, 0.7-1.1 mm, 0.4-0.9 mm, and 1.21-1.44, respectively (Ginter et al., 2012).

Models of vibrissal dynamics are often based on the assumption that each vibrissa is a solid conical frustum (Hartmann et al., 2003; Neimark et al., 2003; Boubenec et al., 2012; Yan et al., 2013; Quist et al., 2014; Lucianna et al., 2016; Yu et al., 2016b). The medulla of rat vibrissae, however, will affect the vibrissae dynamics (Carl et al., 2012; Belli et al., 2017). The Young's modulus of rat vibrissae changes along the length (Quist et al., 2011; Carl et al., 2012). A similar cavity was observed in harbor seal vibrissae. Immersing vibrissae in various solutions, such as water, saline water and balanced salt solution, will change the modulus of elasticity and the damping (Hans et al., 2014). The modulus of elasticity (Young's modulus) of harbor seal vibrissae varies along their lengths from base to tip, and depends on solutions immersed (Hans et al., 2014). Because of the elliptic cross section, the pinniped vibrissae exhibit a variation of Young's modulus with major-minor axis of the ellipse, and the flexural stiffness, EI , are found larger in major axis than minor axis (Ginter Summarell et al., 2015). The Young's modulus of pinniped vibrissae between 4-30 GPa (Hans et al., 2014; Ginter Summarell et al., 2015) is comparable to rat vibrissae ranging from 2-15 GPa (Quist et al., 2011; Carl et al., 2012). But due to their larger diameter, the EI of pinniped vibrissae is nearly 10^3 greater than rat vibrissae (Carl et al., 2012; Ginter Summarell et al., 2015). This difference would be ethologically explained by the large difference of fluid viscosity – pinniped vibrissae in water need to overcome larger fluid friction than rodent vibrissae in air.

In response to airflow, rat vibrissae vibrate at frequencies close to their natural (resonant) modes which are determined by their mechanical properties including Young's modulus, geometry and density (Yu et al., 2016b). This vibration at resonances was also found after touching an object in free air but damped quickly (Hartmann et al., 2003; Quist et al., 2014). In water, however, the pinniped vibrissae vibration frequency not only depends on vibrissae properties, but is also affected by the hydrodynamic condition such as flow speed, Reynolds number and cross-flow diameter (Ginter et al., 2010; Hans et al., 2014; Beem and Triantafyllou, 2015; Ginter Summarell et al., 2015). The natural frequency of a water-wetted harbor seal vibrissa will be different from that of a dry vibrissa resulting from the cavity (Hans et al., 2014). In addition, because pinniped vibrissae exhibited higher flexural stiffness in the major axis of the elliptic cross section than in minor axis, the orientation of the vibrissae will affect the frequency (Murphy et al., 2013; Ginter Summarell et al., 2015).

5.4.2 Active touch of vibrissae in pinniped *versus* rodent

It is well known that both pinniped and rodent vibrissae serve as tactile sensor, by which animals are able to perceive objects. Many studies on pinniped show that pinniped are able to use their vibrissae to discriminate shape and size by direct touch: a California sea lion (*Zalophus californianus*) can distinguish five objects with different shapes (semicircle, hexagon, sandglass, rectangle and square) by means of its vibrissae, and this ability did not differ much from its capability of visual discrimination (Dehnhardt, 1990); the sea lion can discriminate the size of the circular discs and the accuracy was determined by the mechanosensitivity of vibrissae follicle

receptors as well as kinaesthesia (Dehnhardt, 1994); the size difference threshold for equilateral triangles indicated that the sea lion was capable of discriminating size difference as low as 20% (Dehnhardt and Kaminski, 1995; Dehnhardt and Ducker, 1996); a Pacific walrus (*Odobenus rosmarus divergens*) spent more touch time on discriminating smaller shapes (Kastelein and van Gaalen, 1988). The haptic sensation of rat vibrissae on discriminating the object shape, size and even texture discrimination, was also studied widely (Kleinfeld et al., 2006; Jadhav and Feldman, 2010): blinded rats with intact vibrissae can sense wide gaps and leap across them, but the rats with trimmed vibrissae did not cross those wide gaps (Hutson and Masterton, 1986); rats using vibrissae can discern between a sphere and a cube differing in size and texture (Harvey et al., 2001); mystacial macrovibrissae at caudal were mainly involved in spatial tasks, while microvibrissae at rostral were mainly involved in object recognition, particularly for texture discrimination (Brecht et al., 1997; Kuruppath et al., 2014).

Mammals used a variety of strategies to perform vibrissae-associated active touches, such as protracting their vibrissae and adjusting their body's and head's position and orientation by pitch, yawing and rotation (Dehnhardt, 1990; Dehnhardt and Ducker, 1996). One major difference using vibrissae to active touch between pinniped and rodent lies in whisking behavior. Many rodents sweep their macrovibrissae back and forth with amplitudes ranging from 10 to ~50 degrees at rates between 5-25 whisks per second, with a dominant frequency of 8 Hz (Welker, 1964; Carvell and Simons, 1990; Gao et al., 2001; Jin et al., 2004). Rats heavily use this whisking behavior during locomotion and exploration (Knutsen et al., 2008; Quist et al., 2014; Huet et al., 2015b; Huet and Hartmann, 2016). In contrast, pinnipeds do not exhibit clear whisking behavior, although

their vibrissae can move slightly (Kastelein and van Gaalen, 1988; Dehnhardt, 1990). Their head movements thus are very important in active touch. In the shape discrimination task, a California sea lion erected her vibrissae such that the “lateral parts of her snout vaulted, and the long posterior vibrissae of the snout always made the first contact with the object” (Dehnhardt, 1990). To explore the shape, the sea lion performed “gyratory and lateral head movements” (Dehnhardt and Ducker, 1996). Similar touching behaviors were found for harbor seals (Dehnhardt and Kaminski, 1995).

5.4.3 Fluid flow sensation of vibrissae in pinniped *versus* rodent

It has been unclear how pinniped seek food in deep and murky water until twenty years ago when Dehnhardt et al. first found that head-fixed blindfolded harbor seals use their undulated vibrissae to detect water movements (Dehnhardt et al., 1998), like the fish lateral line (Coombs et al., 1989; Bleckmann and Zelick, 2009). After that, the research focus of pinniped vibrissae was then shifted from direct touch, which was mostly conducted ashore, to sensing water movements in the water. This sensation was further tested in free moving blindfolded harbor seals, which used their vibrissae to accurately track hydrodynamic trails generated by a miniature submarine mimicking a goldfish, even after the submarine passed by up to 20 seconds (Dechant et al., 2001). This flow sensing capacity of harbor seal was confirmed in tracking biogenic hydrodynamic trails generated by marine animals rather than artificial trails (Schulte-Pelkum et al., 2007). California sea lions were also able to perform hydrodynamic trail using their vibrissae (Glaser et al., 2011). Furthermore, in water, harbor seals can discriminate paddles of different size or shape by their hydrodynamic characteristics, and particle image velocimetry (PIV) measurements demonstrated

that the seal could take advantage of the flow parameters such as velocities, the gradients, and the spatial extension of a wake to complete the task (Wieskotten et al., 2011).

Two types of hydrodynamic stimuli were often used to investigate the hydrodynamic perception in pinnipeds – dipole stimuli and hydrodynamic trails. Dipole stimuli are generated by a stationary vibrating sphere, of which water movements can be easily obtained and analytically calculated, whereas hydrodynamic trail describe collective water movements generated by a moving object, that contains complex patterns of water movements (Miersch et al., 2011; Hanke et al., 2013). It has been found that California sea lions exhibited a higher sensitivity to dipole stimuli than harbor seals, but harbor seals were better in tracking hydrodynamic trails (Dehnhardt et al., 1998; Dehnhardt et al., 2001; Dehnhardt and Mauck, 2008; Glaser et al., 2011). The difference of hydrodynamic perception in these two species mainly results from their vibrissae's different surface structure – smooth for California sea lion and undulated for harbor seal (Fig. 5.3A). The surprising function of the undulated shape is that it suppresses self-generated noise, or vortex-induced vibrations (VIV), during swimming (Hanke et al., 2010; Witte et al., 2012). The numerical simulation of flow vorticity (Fig. 5.3B) shows that at the same Reynolds number the size of the vortices generated by circular and elliptic cylinders are much bigger than those generated by an undulated vibrissa, and this comparison is observed by a recent work using dye in water flow (Beem and Triantafyllou, 2015). The force measurements on vibrissae in water flow indicate that dynamic forces on harbor seal vibrissae are much lower than those on California sea lion vibrissae (Hanke et al., 2010), and flow measurements on vibrissae's VIV showed a higher signal-to-noise ratio (SNR) for harbor seals than sea lions (Miersch et al., 2011).

In rodents, systematic studies on vibrissae's role of airflow sensing were recently started. Though unlike pinniped whose vibrissae are the crucial organs in flow sensing, rat vibrissae were involved partially, but still significantly, in detecting and following airflow (Yu et al., 2016a). Responses of individual vibrissae to airflow indicate that the mechanics of rat vibrissae encode the airflow speed and direction (Yu et al., 2016b). Just as pinnipeds can sense water wakes and distinguish the shape and size of a remote object, we hypothesize that rodent vibrissae could also discriminate fine airflow structure such as small eddies and trails, other than just the average speed and direction. Although fluid vortices dissipate rapidly in air, differential responses across the vibrissal array could allow a rat to remotely perceive the surrounding geomorphology and distant obstacles without direct touch. Moreover, air puffs were commonly used to stimulate rodent vibrissae when investigating the neural basis of the vibrissae-trigeminal system, which also indicates that airflow information will be taken by the rat brain (Kleinfeld et al., 2002; Ganguly and Kleinfeld, 2004; Ollerenshaw et al., 2012). In contrast, the neurophysiological investigations on pinniped vibrissae system were very limited (Dykes, 1975; Ladygina et al., 1985) and studies simply focus on the morphology of follicle-sinus complexes (F-SCs) (Stephens et al., 1973; Hyvarinen, 1989; Marshall et al., 2006; Ling, 2012). The general vibrissal F-SC form is similar among mammals, but evident differences were found between pinniped and terrestrial taxa (see (Marshall et al., 2006)).

Just as they do for direct touch, pinnipeds protract their vibrissae and often keep them in the most forward position during hydrodynamic perception, no matter whether the water movements are generated by dipole stimuli or hydrodynamic trails (Dehnhardt et al., 1998; Dehnhardt et al., 2001;

Glaser et al., 2011; Miersch et al., 2011). Sometimes, pinnipeds will add some lateral head movements to detect water movements generated by hydrodynamic trails (Dehnhardt et al., 2001; Glaser et al., 2011). Whether rats whisk or not during airflow localization task is unclear (Yu et al., 2016a), but my own unpublished observations suggest that rats would minimize whisking or even hold their vibrissae still when running towards the airflow source, which might increase the signal-to-noise ratio. Like pinnipeds, rats would also protract their vibrissae forward to sense airflow by which the bending magnitude will be higher compared with vibrissae oriented downwards or backwards (Yu et al., 2016b).

5.5 Role in olfactory search

Flow sensors such as the antennae of arthropods, the sensory hairs of insects and bats, and the whiskers (vibrissae) of pinnipeds are used in mediating flight maneuvers (Budick et al., 2007; Sane et al., 2007; Casas and Dangles, 2010; Marshall et al., 2015), escape responses (Casas and Dangles, 2010), wake tracking (Dehnhardt et al., 1998; Dehnhardt et al., 2001) and contributing anemotaxic or rheotaxic information during olfactory search (Rust and Bell, 1976; Baker and Kuenen, 1982; Zimmerfaust et al., 1995; Vickers, 2000; Koehl, 2006; van Breugel and Dickinson, 2014). Like many other animals, rodents present freezing or fleeing (*a.k.a.* fight or flight) defensive behavior triggered by visual or sound stimuli of a presence of aerial predator such as owl or hawk (Hendrie et al., 1998; Edut and Eilam, 2003; Yilmaz and Meister, 2013; Rabi et al., 2017). We think this behavior might also be stimulated by airflow because an aerial predator approaching a rodent will create a downdraft (Thomas and Taylor, 2001; Taylor and Thomas, 2002; Gillies et al., 2011;

Reynolds et al., 2014) that can be detected by vibrissae or other airflow sensing cues. Another important role of vibrissae sensing airflow, we hypothesize, involves in olfactory search that we will discuss below.

5.5.1 Sensing airflow aid olfactory search in a patchy odor plume

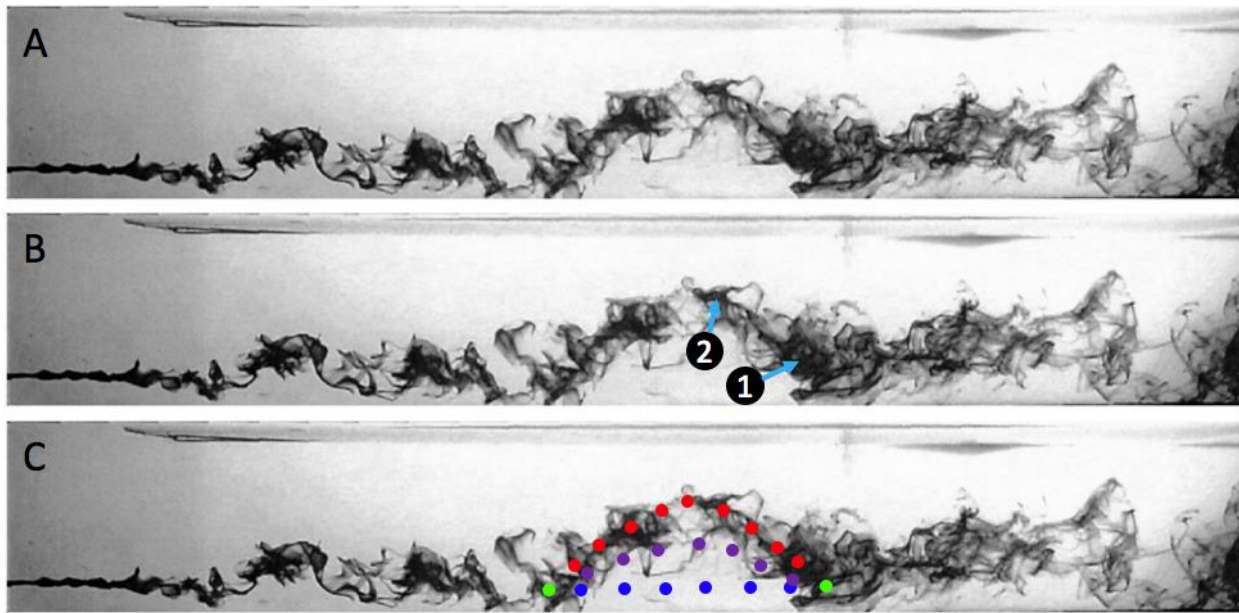


Figure 5.4 Photograph of a patchy odor plume in water. (A) Odor plume in a fully developed turbulent open channel flow. Flow is directed from left to right. Neutrally buoyant red dye is released to obtain the flow visualization. (B) By only sampling the odor concentration, animal in Location 1 would run downstream, and in Location 2 would run cross-stream. (C) Three presumed trajectories animal would take to pass the odor gap (between two green dots): a straight-line (blue dots) against the fluid flow if animal can use flow information to predict the odor source; a curve (red dots) along the highest odor concentration trail if olfaction dominates the search; an optimal or compromised curve (purple dots) between the straight-line and the odor trail by which animal take both odor and flow information into account. Modified from Webster and Weissburg, 2001.

Unlike water movements generated by animals or a miniature submarine that can generate wakes which last for many seconds or even up to minutes (Dechant et al., 2001; Schulte-Pelkum et al.,

2007; Glaser et al., 2011), air movements will not last long because vortices in air dissipate faster than in water. Rats might not be able to track airflow trails left by animals very well. However, given that airflow carries odor (Uchida and Mainen, 2003; Bhattacharyya and Bhalla, 2015), the primary role of rats using vibrissae to sense airflow likely lies in olfactory search. Instead of tracking an airflow trail, rats may use both airflow and chemical information to track an airborne odor plume, like insects, for seeking food and mates, or keeping distance from predator.

Odor plumes are patchy (Fig. 5.4) (Atema, 1996; Weissburg, 2000; Zimmer and Butman, 2000; Webster and Weissburg, 2001). Odor molecular diffusion is the main force driving the distribution of molecules in an ideal case that fluid is immobile, and its mechanism follows Brownian motion. The rate of molecular diffusion, i.e., diffusivity, of a gas is inversely proportional to the square root of its molecular weight and depends on temperature and pressure (Graham's law and Fick's laws). However, it seems impossible to have situations that fluids are completely static, and molecular diffusion in most cases is not the predominant force contributing to the odor distribution. Instead, a better term to describe the odor distribution is dispersion which is closely relevant to fluid motion, and its rate usually is of magnitudes much bigger compared to diffusion. The fluid dynamics impinge directly upon the distribution of odorant molecules spatiotemporally, and the transport of substances in natural fluid is generally dictated by the fluid flow turbulence (Murlis et al., 1992; Nakamoto et al., 1999; Vickers, 2000). In turbulent plumes, the particles are transported in turbulent eddies, so that odor is patchy with its patchiness depending on the size of eddies: small scale eddies can result in fine-scale intermittency whereas larger ones give rise to plume meandering (Murlis et al., 1992; Vickers, 2000). Moreover, the odor plume dynamics strongly

affect the neural activities in moth antennal lobe, which, in turn, can predict very fine-scale temporal dynamics and intensity of the odor (Vickers, 2000).

Fluid flow helps animals to track odors. A cockroach moves downwind when facing an air current, but it will move upwind if sex pheromone is carried by air current (Rust and Bell, 1976). Fluid flow with a higher speed, compared with slow motion, will shorten the duration of odor-free gaps, that will reduce the sampling cost of the animal in tracking an odor source (Reidenbach and Koehl, 2011). Casting, a “reiterative zigzag motion,” is a very common strategy to locate an odor source seen in many animals (Baker and Kuenen, 1982; Murlis et al., 1992; Zimmerfaust et al., 1995; Vickers, 2000; Reidenbach and Koehl, 2011; van Breugel and Dickinson, 2014). Under airflow, a fruit moth at downwind can locate the pheromone source much easier and will take a narrower casting route than that without airflow (Baker and Kuenen, 1982). Casting behavior was also seen in rats during olfactory task (Khan et al., 2012), and importantly, for trained rats in a familiar arena to locate an air-borne odor source, a run-and-scan strategy is faster than casting though the route could be longer (Bhattacharyya and Bhalla, 2015). Knowing fluid flow information can allow animal to predict the odor source since it must originate from upstream, not downstream, so as to minimize the cost of tracking such as the spatial range of casting. If fluid flow information is not perceived, animal would lose the odor trail easily when encountering a big odor gap, such as Locations 1 and 2 in Fig. 5.4B, and it must resample and would take a route toward higher odor concentration, further from the odor source. Ideally, a straight-path going upstream is the fastest way to pass the odor gap though animal will miss odor trail temporally, and the most conservative way is to trace the odor trail exactly (Fig 5.4C). Animal might integrate the chemical and the

airflow information, i.e. chemoanemotaxis (Zimmerfaust et al., 1995; Vickers, 2000; Koehl, 2006), to conceive an optimal path (Fig. 5.4C). Thus, a position vector from animal *per se* to the odor source computed from flow, chemical and other sensations, such as vision (Murlis et al., 1992; Zimmerfaust et al., 1995; Vickers, 2000), will be superior to scalar sampling of odor concentration in olfactory search.

5.5.2 Whisking and sniffing

Whether animal makes use of airflow sensation to assist tracking odor trail is unclear. To test this in rats, blocking or removing the airflow sensation from vibrissae and others is needed but difficult, given that airflow sensing cues are not well understood. However, recent findings that whisking and sniffing (or high-frequency breathing) behaviors are synchronized by activity from the same central pattern generator – preBötzing nucleus (Moore et al., 2013), conferring a degree of temporal precision that could align anemotaxic information from the vibrissae with odorant information during olfactory search.

The synchrony between whisking and sniffing behaviors was first observed in Welker's work on analyzing a characteristic pattern of sniffing of the albino rat when animal is exploring novel stimuli, which includes four behaviors – polypnea, vibrissae, nose and head movements (Welker, 1964). A series of anatomical, behavioral, electrophysiological and pharmacological investigations demonstrated that the coordination of whisking and sniffing is from the respiratory centers of the ventral medulla, where a distinct region provides rhythmic input to drive the movement of

vibrissae, and this cycle will be reset at each inspiration by direct input from the pre-Botzinger complex. (Moore et al., 2013). Although whisking and breathing can occur independently from each other, the synchronization of whisking and sniffing happens in rodents during active exploration (Moore et al., 2013; Ranade et al., 2013; Kleinfeld et al., 2016). Both rhythmic whisking and sniffing are within the theta frequency range (4-12 Hz) and are phase locked in multiple modes, such as two whisks in each sniff, one whisk in each sniff, and one whisk in two sniffs (Ranade et al., 2013). Though sniffing is not strictly necessary for smell, and touch can occur without whisking, the fast sampling of the environment by sniffing and whisking are valuable in animal's survival, locomotion, and interests (Deschenes et al., 2012). The phase-locking of whisking and sniffing could allow the animal to obtain the smell and the location information, simultaneously or at a fixed temporal interval, of a nearby object (Kleinfeld et al., 2014). Similarly, in airflow, the vibrissae's dynamics, either whisking or being held still, and the nostril activities, either sniffing or at basal respiration, could bring the odor and the direction information of a distant object to the animal.

The cross-modal nature of this proposed vibrissotactile-olfactory information stream underscores the need for rodents to continuously adjust the relationship between whisking and sniffing, as reflected in the dynamic relationship between the coupled neural oscillators known to drive these rhythmic behaviors (Moore et al., 2013; Ranade et al., 2013; Kleinfeld et al., 2014). Passive displacements due to airflow will likely be easiest to sense if the vibrissae are held relatively immobile to avoid contamination with a peripheral reafferent signal (Fee et al., 1997; Leiser and Moxon, 2007; Khatri et al., 2009; Wallach et al., 2016). Thus, at times when anemotaxis is

paramount, the rat may minimize whisking, whereas at other times, the animal may exploit bilateral nostril comparisons (Rajan et al., 2006; Khan et al., 2012; Catania, 2013) and is likely to generate synchronized ~8-Hz sniffing and whisking (Smear et al., 2011; Moore et al., 2013; Ranade et al., 2013; Kleinfeld et al., 2014; Bhattacharyya and Bhalla, 2015). Future studies that directly assess involvement of the macrovibrissae in olfactory search would help to elucidate characteristics of the mechanotactile information that vibrissal-responsive regions of the nervous system evolved to process.

5.6 Future work

Directions for future study include (1) investigating the airflow structure around the whisker and the rat's head, (2) understanding the strategies that the rat uses to sense airflow, and (3) recording from more neurons in the Vg and other regions of the whisker-trigeminal pathway to explore the encoding of airflow information.

References

- [1]. **Albert, J. T., Friedrich, O. C., Dechant, H. E. and Barth, F. G.** (2001). Arthropod touch reception: Spider hair sensilla as rapid touch detectors. *Journal of Comparative Physiology A* **187**, 303-312.
- [2]. **Andermann, M. L., Ritt, J., Neimark, M. A. and Moore, C. I.** (2004). Neural correlates of vibrissa resonance: Band-pass and somatotopic representation of high-frequency stimuli. *Neuron* **42**, 451-463.
- [3]. **Arkley, K., Grant, R. A., Mitchinson, B. and Prescott, T. J.** (2014). Strategy change in vibrissal active sensing during rat locomotion. *Current Biology* **24**, 1507-1512.
- [4]. **Atema, J.** (1996). Eddy chemotaxis and odor landscapes: Exploration of nature with animal sensors. *Biological Bulletin* **191**, 129-138.
- [5]. **Bagdasarian, K., Szwed, M., Knutsen, P. M., Deutsch, D., Derdikman, D., Pietr, M., Simony, E. and Ahissar, E.** (2013). Pre-neuronal morphological processing of object location by individual whiskers. *Nature Neuroscience* **16**, 622-631.
- [6]. **Baker, T. C. and Kuenen, L. P.** (1982). Pheromone source location by flying moths: A supplementary non-anemotactic mechanism. *Science* **216**, 424-427.
- [7]. **Barth, F. G., Wastl, U., Humphrey, J. A. C. and Devarakonda, R.** (1993). Dynamics of arthropod filiform hairs. 2. Mechanical-properties of spider trichobothria (*cupiennius-salei* keys). *Philosophical Transactions of the Royal Society B: Biological Sciences* **340**, 445-461.

- [8]. **Barth, F. G., Humphrey, J. A. C., Wastl, U., Halbritter, J. and Brittinger, W.** (1995). Dynamics of arthropod filiform hairs. 3. Flow patterns related to air movement detection in a spider (*Cupiennius-salei* keys). *Philosophical Transactions of the Royal Society B: Biological Sciences* **347**, 397-412.
- [9]. **Barth, F. G.** (2002). Spider senses - technical perfection and biology. *Zoology* **105**, 271-285.
- [10]. **Barth, F. G.** (2004). Spider mechanoreceptors. *Current Opinion in Neurobiology* **14**, 415-422.
- [11]. **Bathellier, B., Steinmann, T., Barth, F. G. and Casas, J.** (2012). Air motion sensing hairs of arthropods detect high frequencies at near-maximal mechanical efficiency. *Journal of The Royal Society Interface* **9**, 1131-1143.
- [12]. **Beem, H. R. and Triantafyllou, M. S.** (2015). Wake-induced 'slaloming' response explains exquisite sensitivity of seal whisker-like sensors. *Journal of Fluid Mechanics* **783**, 306-322.
- [13]. **Bellavance, M. A., Takatoh, J., Lu, J., Demers, M., Kleinfeld, D., Wang, F. and Deschenes, M.** (2017). Parallel inhibitory and excitatory trigemino-facial feedback circuitry for reflexive vibrissa movement. *Neuron* **95**, 722-723.
- [14]. **Belli, H. M., Yang, A. E., Bresee, C. S. and Hartmann, M. J. Z.** (2017). Variations in vibrissal geometry across the rat mystacial pad: base diameter, medulla, and taper. *Journal of Neurophysiology* **117**, 1807-1820.
- [15]. **Bhattacharyya, U. and Bhalla, U. S.** (2015). Robust and rapid air-borne odor tracking without casting. *eNeuro* **2**, e0102.

- [16]. Birdwell, J. A., Solomon, J. H., Thajchayapong, M., Taylor, M. A., Cheely, M., Towal, R. B., Conratt, J. and Hartmann, M. J. Z. (2007). Biomechanical models for radial distance determination by the rat vibrissal system. *Journal of Neurophysiology* 98, 2439-2455.
- [17]. **Bleckmann, H. and Zelick, R.** (2009). Lateral line system of fish. *Integrative Zoology* 4, 13-25.
- [18]. **Blickhan, R. and Barth, F. G.** (1985). Strains in the exoskeleton of spiders. *Journal of Comparative Physiology A* 157, 115-147.
- [19]. Bosman, L. W. J., Houweling, A. R., Owens, C. B., Tanke, N., Shevchouk, O. T., Rahmati, N., Teunissen, W. H. T., Ju, C., Gong, W., Koekkoek, S. K. E. et al. (2011). Anatomical pathways involved in generating and sensing rhythmic whisker movements. *Frontiers in integrative neuroscience* 5, 53.
- [20]. **Boubenec, Y., Shulz, D. E. and Debregeas, G.** (2012). Whisker encoding of mechanical events during active tactile exploration. *Frontiers in Behavioral Neuroscience* 6.
- [21]. **Bouquet, J. Y.** (2013). Camera calibration toolbox for Matlab, http://www.vision.caltech.edu/bouquetj/calib_doc/.
- [22]. **Brecht, M., Preilowski, B. and Merzenich, M. M.** (1997). Functional architecture of the mystacial vibrissae. *Behavioural Brain Research* 84, 81-97.
- [23]. **Budick, S. A., Reiser, M. B. and Dickinson, M. H.** (2007). The role of visual and mechanosensory cues in structuring forward flight in *Drosophila melanogaster*. *Journal of Experimental Biology* 210, 4092-4103.

- [24]. **Burda, H., Sumbera, R. and Begall, S.** (2007). Microclimate in burrows of subterranean rodents - Revisited. *Subterranean Rodents: News from Underground*, 21-+.
- [25]. **Carl, K., Hild, W., Mampel, J., Schilling, C., Uhlig, R. and Witte, H.** (2012). Characterization of statical properties of rat's whisker system. *Ieee Sensors Journal* **12**, 340-349.
- [26]. **Carvell, G. E. and Simons, D. J.** (1990). Biometric analyses of vibrissal tactile discrimination in the rat. *Journal of Neuroscience* **10**, 2638-2648.
- [27]. **Casas, J. and Dangles, O.** (2010). Physical ecology of fluid flow sensing in arthropods. *Annual Review of Entomology* **55**, 505-520.
- [28]. **Casas, J., Steinmann, T. and Krijnen, G.** (2010). Why do insects have such a high density of flow-sensing hairs? Insights from the hydromechanics of biomimetic MEMS sensors. *Journal of The Royal Society Interface* **7**, 1487-95.
- [29]. **Catania, K. C.** (2009). Tentacled snakes turn C-starts to their advantage and predict future prey behavior. *PNAS* **106**, 11183-11187.
- [30]. **Catania, K. C.** (2013). Stereo and serial sniffing guide navigation to an odour source in a mammal. *Nature Communications* **4**, 1441.
- [31]. **Coombs, S., Görner, P. and Münz, H.** (1989). *The Mechanosensory lateral line: neurobiology and evolution*. New York: Springer-Verlag.
- [32]. **Crissman, R. S., Warden, R. J., Siciliano, D. A., Klein, B. G., Renehan, W. E., Jacquin, M. F. and Rhoades, R. W.** (1991). Numbers of axons innervating mystacial vibrissa follicles in newborn and adult rats. *Somatosensory & Motor Research* **8**, 103-109.

- [33]. **Cummins, B., Gedeon, T., Klapper, I. and Cortez, R.** (2007). Interaction between arthropod filiform hairs in a fluid environment. *Journal of Theoretical Biology* **247**, 266-280.
- [34]. **Dangles, O., Pierre, D., Christides, J. P. and Casas, J.** (2007). Escape performance decreases during ontogeny in wild crickets. *Journal of Experimental Biology* **210**, 3165-3170.
- [35]. **Dechant, H.-E., Hoessl, B., Rammerstorfer, F. G. and Barth, F. G.** (2006). Arthropod mechanoreceptive hairs: modeling the directionality of the joint. *Journal of Comparative Physiology A* **192**, 1271-1278.
- [36]. **Dechant, H. E., Rammerstorfer, F. G. and Barth, F. G.** (2001). Arthropod touch reception: stimulus transformation and finite element model of spider tactile hairs (vol 187, pg 313, 2001). *Journal of Comparative Physiology A* **187**, 313-322.
- [37]. **Dehnhardt, G.** (1990). Preliminary-results from psychophysical studies on the tactile sensitivity in marine mammals. *Sensory Abilities of Cetaceans* **196**, 435-446.
- [38]. **Dehnhardt, G.** (1994). Tactile size discrimination by a California sea lion (*Zalophus californianus*) using its mystacial vibrissae. *Journal of Comparative Physiology A* **175**, 791-800.
- [39]. **Dehnhardt, G. and Kaminski, A.** (1995). Sensitivity of the mystacial vibrissae of harbour seals (*Phoca vitulina*) for size differences of actively touched objects. *Journal of Experimental Biology* **198**, 2317-2323.
- [40]. **Dehnhardt, G. and Ducker, G.** (1996). Tactual discrimination of size and shape by a California sea lion (*Zalophus californianus*). *Animal Learning & Behavior* **24**, 366-374.

- [41]. **Dehnhardt, G., Mauck, B. and Bleckmann, H.** (1998). Seal whiskers detect water movements. *Nature* **394**, 235-236.
- [42]. **Dehnhardt, G., Mauck, B., Hanke, W. and Bleckmann, H.** (2001). Hydrodynamic trail-following in harbor seals (*Phoca vitulina*). *Science* **293**, 102-104.
- [43]. **Dehnhardt, G. and Mauck, B.** (2008). Mechanoreception in secondarily aquatic vertebrates: University of California Press.
- [44]. **Deschenes, M., Moore, J. and Kleinfeld, D.** (2012). Sniffing and whisking in rodents. *Current Opinion in Neurobiology* **22**, 243-250.
- [45]. **Diamond, M. E., von Heimendahl, M., Knutsen, P. M., Kleinfeld, D. and Ahissar, E.** (2008). 'Where' and 'what' in the whisker sensorimotor system. *Nature Reviews Neuroscience* **9**, 601-612.
- [46]. **Dowell, E. H.** (1970). Panel flutter - A review of the aeroelastic stability of plates and shells. *AIAA Journal* **8**, 385-399.
- [47]. **Dykes, R. W.** (1975). Afferent-fibers from mystacial vibrissae of cats and seals. *Journal of Neurophysiology* **38**, 650-662.
- [48]. **Edut, S. and Eilam, D.** (2003). Rodents in open space adjust their behavioral response to the different risk levels during barn-owl attack. *BMC Ecology* **3**.
- [49]. **Fee, M. S., Mitra, P. P. and Kleinfeld, D.** (1997). Central versus peripheral determinants of patterned spike activity in rat vibrissa cortex during whisking. *Journal of Neurophysiology* **78**, 1144-1149.
- [50]. **Fletcher, N. H.** (1978). Acoustical Response of Hair Receptors in Insects. *Journal of Comparative Physiology A* **127**, 185-189.

- [51]. **Fourcaud-Trocme, N., Hansel, D., van Vreeswijk, C. and Brunel, N.** (2003). How spike generation mechanisms determine the neuronal response to fluctuating inputs. *Journal of Neuroscience* **23**, 11628-11640.
- [52]. **Ganguly, K. and Kleinfeld, D.** (2004). Goal-directed whisking increases phase-locking between vibrissa movement and electrical activity in primary sensory cortex in rat. *PNAS* **101**, 12348-12353.
- [53]. **Gao, P., Bermejo, R. and Zeigler, H. P.** (2001). Whisker deafferentation and rodent whisking patterns: behavioral evidence for a central pattern generator. *Journal of Neuroscience* **21**, 5374-5380.
- [54]. **Georgian, J.** (1965). Vibration frequencies of tapered bars and circular plates. *Journal of Applied Mechanics* **32**, 234–235.
- [55]. **Gillies, J. A., Thomas, A. L. R. and Taylor, G. K.** (2011). Soaring and manoeuvring flight of a steppe eagle *Aquila nipalensis*. *Journal of Avian Biology* **42**, 377-386.
- [56]. **Ginter, C. C., Fish, F. E. and Marshall, C. D.** (2010). Morphological analysis of the bumpy profile of phocid vibrissae. *Marine Mammal Science* **26**, 733-743.
- [57]. **Ginter, C. C., DeWitt, T. J., Fish, F. E. and Marshall, C. D.** (2012). Fused traditional and geometric morphometrics demonstrate pinniped whisker diversity. *Plos One* **7**, e34481.
- [58]. **Ginter Summarell, C. C., Ingle, S., Fish, F. E. and Marshall, C. D.** (2015). Comparative analysis of the flexural stiffness of pinniped vibrissae. *Plos One* **10**, e0127941.

- [59]. **Glaser, N., Wieskotten, S., Otter, C., Dehnhardt, G. and Hanke, W.** (2011). Hydrodynamic trail following in a California sea lion (*Zalophus californianus*). *Journal of Comparative Physiology A* **197**, 141-151.
- [60]. **Gnatzy, W. and Tautz, J.** (1980). Ultrastructure and mechanical properties of an insect mechanoreceptor: stimulus-transmitting structures and sensory apparatus of the cercal filiform hairs of *Gryllus*. *Cell and Tissue Research* **213**, 441-63.
- [61]. **Grant, R., Wieskotten, S., Wengst, N., Prescott, T. and Dehnhardt, G.** (2013a). Vibrissal touch sensing in the harbor seal (*Phoca vitulina*): How do seals judge size? *Journal of Comparative Physiology A* **199**, 521-533.
- [62]. **Grant, R. A., Haidarliu, S., Kennerley, N. J. and Prescott, T. J.** (2013b). The evolution of active vibrissal sensing in mammals: evidence from vibrissal musculature and function in the marsupial opossum *Monodelphis domestica*. *Journal of Experimental Biology* **216**, 3483-3494.
- [63]. **Grasso, F. W. and Basil, J. A.** (2002). How lobsters, crayfishes, and crabs locate sources of odor: current perspectives and future directions. *Current Opinion in Neurobiology* **12**, 721-727.
- [64]. **Guadanucci, J. P. L.** (2012). Trichobothrial morphology of theraphosidae and barychelidae spiders (Araneae, Mygalomorphae). *Zootaxa*, 1-42.
- [65]. **Hanke, W., Witte, M., Miersch, L., Brede, M., Oeffner, J., Michael, M., Hanke, F., Leder, A. and Dehnhardt, G.** (2010). Harbor seal vibrissa morphology suppresses vortex-induced vibrations. *Journal of Experimental Biology* **213**, 2665-2672.

- [66]. **Hanke, W., Wieskotten, S., Marshall, C. and Dehnhardt, G.** (2013). Hydrodynamic perception in true seals (Phocidae) and eared seals (Otariidae). *Journal of Comparative Physiology A* **199**, 421-440.
- [67]. **Hans, H., Miao, J. M. and Triantafyllou, M. S.** (2014). Mechanical characteristics of harbor seal (*Phoca vitulina*) vibrissae under different circumstances and their implications on its sensing methodology. *Bioinspiration & Biomimetics* **9**.
- [68]. **Hartmann, M. J. Z.** (2001). Active sensing capabilities of the rat whisker system. *Autonomous Robots* **11**, 249-254.
- [69]. **Hartmann, M. J. Z., Johnson, N. J., Towal, R. B. and Assad, C.** (2003). Mechanical characteristics of rat vibrissae: Resonant frequencies and damping in isolated whiskers and in the awake behaving animal. *Journal of Neuroscience* **23**, 6510-6519.
- [70]. **Harvey, M. A., Bermejo, R. and Zeigler, H. P.** (2001). Discriminative whisking in the head-fixed rat: optoelectronic monitoring during tactile detection and discrimination tasks. *Somatosensory & Motor Research* **18**, 211-22.
- [71]. **Hendrie, C. A., Weiss, S. M. and Eilam, D.** (1998). Behavioural response of wild rodents to the calls of an owl: a comparative study. *Journal of Zoology* **245**, 439-446.
- [72]. **Hires, S. A., Pammer, L., Svoboda, K. and Golomb, D.** (2013). Tapered whiskers are required for active tactile sensation. *Elife* **2**, 10.7554/eLife.01350.
- [73]. **Hobbs, J. A., Towal, R. B. and Hartmann, M. J. Z.** (2015). Spatiotemporal patterns of contact across the rat vibrissal array during exploratory behavior. *Frontiers in Behavioral Neuroscience* **in revision**.

- [74]. **Hobbs, J. A., Towal, R. B. and Hartmann, M. J. Z.** (2016). Spatiotemporal patterns of contact across the rat vibrissal array during exploratory behavior. *Frontiers in Behavioral Neuroscience* **9**, 356.
- [75]. **Huet, L., CL, S. and Hartmann, M.** (2015a). Tactile signals transmitted by the vibrissa during active whisking behavior. *J. Neurophysiol.* **in press**.
- [76]. **Huet, L. A., Schroeder, C. L. and Hartmann, M. J. Z.** (2015b). Tactile signals transmitted by the vibrissa during active whisking behavior. *Journal of Neurophysiology* **113**, 3511-3518.
- [77]. **Huet, L. A. and Hartmann, M. J. Z.** (2016). Simulations of a vibrissa slipping along a straight edge and an analysis of frictional effects during whisking. *IEEE Transactions on Haptics* **9**, 158-169.
- [78]. **Humphrey, J. A. C., Devarakonda, R., Iglesias, I. and Barth, F. G.** (1993). Dynamics of arthropod filiform hairs. 1. Mathematical-modeling of the hair and air motions. *Philosophical Transactions of the Royal Society B: Biological Sciences* **340**, 423-444.
- [79]. **Humphrey, J. A. C. and Barth, F. G.** (2007). Medium flow-sensing hairs: Biomechanics and models. In *Advances in Insect Physiology: Insect Mechanics and Control*, vol. 34 (ed. J. Casas), pp. 1-80. San Diego: Elsevier Academic Press Inc.
- [80]. **Hutcheon, B. and Yarom, Y.** (2000). Resonance, oscillation and the intrinsic frequency preferences of neurons. *Trends in Neuroscience* **23**, 216-222.
- [81]. **Hutson, K. A. and Masterton, R. B.** (1986). The sensory contribution of a single vibrissa's cortical barrel. *Journal of Neurophysiology* **56**, 1196-1223.

- [82]. **Hyvarinen, H.** (1989). Diving in darkness - whiskers as sense-organs of the ringed seal (*Phoca hispida saimensis*). *Journal of Zoology* **218**, 663-678.
- [83]. **Ibrahim, L. and Wright, E. A.** (1975). Growth of rats and mice vibrissae under normal and some abnormal conditions. *Journal of Embryology and Experimental Morphology* **33**, 831-844.
- [84]. **Jacobs, G. A.** (1995). Detection and analysis of air currents by crickets - a special insect sense. *Bioscience* **45**, 776-785.
- [85]. **Jadhav, S. P. and Feldman, D. E.** (2010). Texture coding in the whisker system. *Current Opinion in Neurobiology* **20**, 313-318.
- [86]. **Jin, T. E., Witzemann, V. and Brecht, M.** (2004). Fiber types of the intrinsic whisker muscle and whisking behavior. *Journal of Neuroscience* **24**, 3386-3393.
- [87]. **Kan, Q. H., Rajan, R., Fu, J., Kang, G. Z. and Yan, W. Y.** (2013). Elastic modulus of rat whiskers-A key biomaterial in the rat whisker sensory system. *Materials Research Bulletin* **48**, 5026-5032.
- [88]. **Kaneko, S., Inada, F., Nakamura, T. and Kato, M.** (2008). Vibration Induced by Cross-Flow. *Flow Induced Vibrations: Classifications and Lessons from Practical Experiences*, 29-106.
- [89]. **Kastelein, R. A. and van Gaalen, M. A.** (1988). The sensitivity of the vibrissae of a Pacific walrus (*Odobenus rosmarus divergens*) Part 1. *Aquatic Mammals* **14**, 123-133.
- [90]. **Khalak, A. and Williamson, C. H. K.** (1999). Motions, forces and mode transitions in vortex-induced vibrations at low mass-damping. *Journal of Fluids and Structures* **13**, 813-851.

- [91]. **Khan, A. G., Sarangi, M. and Bhalla, U. S.** (2012). Rats track odour trails accurately using a multi-layered strategy with near-optimal sampling. *Nature Communications* **3**, 703.
- [92]. **Khatri, V., Bermejo, R., Brumberg, J. C., Keller, A. and Zeigler, H. P.** (2009). Whisking in air: encoding of kinematics by trigeminal ganglion neurons in awake rats. *Journal of Neurophysiology* **101**, 1836-1846.
- [93]. **Kleinfeld, D., Sachdev, R. N., Merchant, L. M., Jarvis, M. R. and Ebner, F. F.** (2002). Adaptive filtering of vibrissa input in motor cortex of rat. *Neuron* **34**, 1021-1034.
- [94]. **Kleinfeld, D., Ahissar, E. and Diamond, M. E.** (2006). Active sensation: insights from the rodent vibrissa sensorimotor system. *Current Opinion in Neurobiology* **16**, 435-444.
- [95]. **Kleinfeld, D., Deschenes, M., Wang, F. and Moore, J. D.** (2014). More than a rhythm of life: breathing as a binder of orofacial sensation. *Nature Neuroscience* **17**, 647-651.
- [96]. **Kleinfeld, D., Deschenes, M. and Ulanovsky, N.** (2016). Whisking, sniffing, and the hippocampal theta-rhythm: A tale of two oscillators. *Plos Biology* **14**, e1002385.
- [97]. **Knutsen, P. M., Biess, A. and Ahissar, E.** (2008). Vibrissal kinematics in 3D: Tight coupling of azimuth, elevation, and torsion across different whisking modes. *Neuron* **59**, 35-42.
- [98]. **Koehl, M. A.** (2006). The fluid mechanics of arthropod sniffing in turbulent odor plumes. *Chemical Senses* **31**, 93-105.
- [99]. **Kuruppath, P., Gugig, E. and Azouz, R.** (2014). Microvibrissae-based texture discrimination. *Journal of Neuroscience* **34**, 5115-5120.

- [100]. **Kwegyir-Afful, E. E., Marella, S. and Simons, D. J.** (2008). Response properties of mouse trigeminal ganglion neurons. *Somatosensory & Motor Research* **25**, 209-221.
- [101]. **Ladygina, T. F., Popov, V. V. and Supin, A. Y.** (1985). Topical organization of somatic projections in the fur-seal cerebral-cortex. *Neurophysiology* **17**, 246-252.
- [102]. **Lee, B. H. K., Price, S. J. and Wong, Y. S.** (1999). Nonlinear aeroelastic analysis of airfoils: bifurcation and chaos. *Progress in Aerospace Sciences* **35**, 205-334.
- [103]. **Leiser, S. C. and Moxon, K. A.** (2007). Responses of trigeminal ganglion neurons during natural whisking behaviors in the awake rat. *Neuron* **53**, 117-133.
- [104]. **Lichtenstein, S. H., Carvell, G. E. and Simons, D. J.** (1990). Responses of rat trigeminal ganglion neurons to movements of vibrissae in different directions. *Somatosensory & Motor Research* **7**, 47-65.
- [105]. **Ling, J. K.** (2012). The skin and hair of the southern elephant seal, *Mirounga leonina* (Linn.). IV. Annual cycle of pelage follicle activity and moult. *Australian Journal of Zoology* **60**, 259-271.
- [106]. **Lucia, D. J., Beran, P. S. and Silva, W. A.** (2004). Reduced-order modeling: new approaches for computational physics. *Progress in Aerospace Sciences* **40**, 51-117.
- [107]. **Lucianna, F. A., Albarracin, A. L., Vrech, S. M., Farfan, F. D. and Felice, C. J.** (2016). The mathematical whisker: A review of numerical models of the rat's vibrissa biomechanics. *Journal of Biomechanics* **49**, 2007-2014.
- [108]. **Magal, C., Dangles, O., Caparroy, P. and Casas, J.** (2006). Hair canopy of cricket sensory system tuned to predator signals. *Journal of Theoretical Biology* **241**, 459-466.

- [109]. **Marshall, C. D., Amin, H., Kovacs, K. M. and Lydersen, C.** (2006). Microstructure and innervation of the mystacial vibrissal follicle-sinus complex in bearded seals, *Erignathus barbatus* (Pinnipedia: Phocidae). *The Anatomical Record* **288**, 13-25.
- [110]. Marshall, K. L., Chadha, M., Desouza, L. A., Sterbing-D'Angelo, S. J., Moss, C. F. and Lumpkin, E. A. (2015). Somatosensory substrates of flight control in bats. *Cell Reports* **11**, 851-858.
- [111]. **McElvain, L. E., Friedman, B., Karten, H. J., Svoboda, K., Wang, F., Deschênes, M. and Kleinfeld, D.** (2017). Circuits in the rodent brainstem that control whisking in concert with other orofacial motor actions. *Neuroscience*.
- [112]. **Miersch, L., Hanke, W., Wieskotten, S., Hanke, F. D., Oeffner, J., Leder, A., Brede, M., Witte, M. and Dehnhardt, G.** (2011). Flow sensing by pinniped whiskers. *Philosophical Transactions of the Royal Society B: Biological Sciences* **366**, 3077-3084.
- [113]. **Monahan, A. H., He, Y. P., McFarlane, N. and Dai, A. G.** (2011). The probability distribution of land surface wind speeds. *Journal of Climate* **24**, 3892-3909.
- [114]. **Moore, J. D., Deschenes, M., Furuta, T., Huber, D., Smear, M. C., Demers, M. and Kleinfeld, D.** (2013). Hierarchy of orofacial rhythms revealed through whisking and breathing. *Nature* **497**, 205-212.
- [115]. **Muchlinski, M. N.** (2010). A comparative analysis of vibrissa count and infraorbital foramen area in primates and other mammals. *Journal of Human Evolution* **58**, 447-473.
- [116]. **Murlis, J., Elkinton, J. S. and Carde, R. T.** (1992). Odor plumes and how insects use them. *Annual Review of Entomology* **37**, 505-532.

- [117]. **Murphy, C. T., Eberhardt, W. C., Calhoun, B. H., Mann, K. A. and Mann, D. A.** (2013). Effect of angle on flow-induced vibrations of pinniped vibrissae. *Plos One* **8**, e69872.
- [118]. **Nakamoto, T., Ishida, H. and Moriizumi, T.** (1999). A sensing system for odor plumes. *Analytical Chemistry News & Features* **71**, 531-537.
- [119]. **Neimark, M. A., Andermann, M. L., Hopfield, J. J. and Moore, C. I.** (2003). Vibrissa resonance as a transduction mechanism for tactile encoding. *Journal of Neuroscience* **23**, 6499–6509.
- [120]. **Ollerenshaw, D. R., Bari, B. A., Millard, D. C., Orr, L. E., Wang, Q. and Stanley, G. B.** (2012). Detection of tactile inputs in the rat vibrissa pathway. *Journal of Neurophysiology* **108**, 479-490.
- [121]. **Prescott, S. A., De Koninck, Y. and Sejnowski, T. J.** (2008). Biophysical basis for three distinct dynamical mechanisms of action potential initiation. *Plos Computational Biology* **4**, e1000198.
- [122]. **Quist, B. W., Faruqi, R. A. and Hartmann, M. J. Z.** (2011). Variation in Young's modulus along the length of a rat vibrissa. *Journal of Biomechanics* **44**, 2775-2781.
- [123]. **Quist, B. W. and Hartmann, M. J. Z.** (2012). Mechanical signals at the base of a rat vibrissa: the effect of intrinsic vibrissa curvature and implications for tactile exploration. *Journal of Neurophysiology* **107**, 2298-2312.
- [124]. **Quist, B. W., Seghete, V., Huet, L. A., Murphey, T. D. and Hartmann, M. J. Z.** (2014). Modeling Forces and Moments at the Base of a Rat Vibrissa during Noncontact Whisking and Whisking against an Object. *Journal of Neuroscience* **34**, 9828-9844.

- [125]. **Rabi, C., Zadicario, P., Mazon, Y., Wagner, N. and Eilam, D.** (2017). The response of social and non-social rodents to owl attack. *Behavioral Ecology and Sociobiology* **71**, 131.
- [126]. **Rajan, R., Clement, J. P. and Bhalla, U. S.** (2006). Rats smell in stereo. *Science* **311**, 666-670.
- [127]. **Ranade, S., Hangya, B. and Kepecs, A.** (2013). Multiple modes of phase locking between sniffing and whisking during active exploration. *Journal of Neuroscience* **33**, 8250-8256.
- [128]. **Reep, R. L., Gaspard, J. C., Sarko, D., Rice, F. L., Mann, D. A. and Bauer, G. B.** (2011). Manatee vibrissae: evidence for a "lateral line" function. *Annals of The New York Academy of Sciences* **1225**, 101-109.
- [129]. **Reidenbach, M. A. and Koehl, M. A. R.** (2011). The spatial and temporal patterns of odors sampled by lobsters and crabs in a turbulent plume. *Journal of Experimental Biology* **214**, 3138-3153.
- [130]. **Reynolds, K. V., Thomas, A. L. and Taylor, G. K.** (2014). Wing tucks are a response to atmospheric turbulence in the soaring flight of the steppe eagle *Aquila nipalensis*. *Journal of The Royal Society Interface* **11**, 20140645.
- [131]. **Rice, F. L., Kinnman, E., Aldskogius, H., Johansson, O. and Arvidsson, J.** (1993). The innervation of the mystacial pad of the rat as revealed by PGP 9.5 immunofluorescence. *Journal of Comparative Neurology* **337**, 366-385.

- [132]. **Ritt, J. T., Andermann, M. L. and Moore, C. I.** (2008). Embodied information processing: Vibrissa mechanics and texture features shape micromotions in actively sensing rats. *Neuron* **57**, 599-613.
- [133]. Rossant, C., Kadir, S. N., Goodman, D. F. M., Schulman, J., Hunter, M. L. D., Saleem, A. B., Grosmark, A., Belluscio, M., Denfield, G. H., Ecker, A. S. et al. (2016). Spike sorting for large, dense electrode arrays. *Nature Neuroscience* **19**, 634-641.
- [134]. **Rust, M. K. and Bell, W. J.** (1976). Chemo-anemotaxis: a behavioral response to sex pheromone in nonflying insects. *PNAS* **73**, 2524-2526.
- [135]. **Sainsbury, R. N.** (1971). Oscillation of piles-some marine experience. *Ground Engineering*, 44-51.
- [136]. **Salinas, E., Hernandez, A., Zainos, A. and Romo, R.** (2000). Periodicity and firing rate as candidate neural codes for the frequency of vibrotactile stimuli. *Journal of Neuroscience* **20**, 5503-5515.
- [137]. **Sane, S. P., Dieudonne, A., Willis, M. A. and Daniel, T. L.** (2007). Antennal mechanosensors mediate flight control in moths. *Science* **315**, 863-866.
- [138]. **Sarpkaya, T.** (2004). A critical review of the intrinsic nature of vortex-induced vibrations. *Journal of Fluids and Structures* **19**, 389-447.
- [139]. **Schooley, R. L. and Branch, L. C.** (2005). Limited perceptual range and anemotaxis in marsh rice rats *Oryzomys palustris*. *Acta Theriologica* **50**, 59-66.
- [140]. **Schulte-Pelkum, N., Wieskotten, S., Hanke, W., Dehnhardt, G. and Mauck, B.** (2007). Tracking of biogenic hydrodynamic trails in harbour seals (*Phoca vitulina*). *Journal of Experimental Biology* **210**, 781-787.

- [141]. **Sherman, D., Oram, T., Deutsch, D., Gordon, G., Ahissar, E. and Harel, D.** (2013). Tactile modulation of whisking via the brainstem loop: statechart modeling and experimental validation. *Plos One* **8**, e79831.
- [142]. **Shimozawa, T., Murakami, J. and Kumagai, T.** (2003). Cricket wind receptors: Thermal noise for the highest sensitivity known. *Sensors and Sensing in Biology and Engineering*, 145-157.
- [143]. **Smear, M., Shusterman, R., O'Connor, R., Bozza, T. and Rinberg, D.** (2011). Perception of sniff phase in mouse olfaction. *Nature* **479**, 397-400.
- [144]. **Solomon, J. H. and Hartmann, M. J. Z.** (2008). Artificial whiskers suitable for array implementation: Accounting for lateral slip and surface friction. *Ieee Transactions on Robotics* **24**, 1157-1167.
- [145]. **Solomon, J. H. and Hartmann, M. J. Z.** (2010). Extracting object contours with the sweep of a robotic whisker using torque information. *International Journal of Robotics Research* **29**, 1233-1245.
- [146]. **Solomon, J. H. and Hartmann, M. J.** (2011). Radial distance determination in the rat vibrissal system and the effects of Weber's law. *Philos Trans R Soc Lond B Biol Sci* **366**, 3049-57.
- [147]. **Stephens, R. J., Beebe, I. J. and Poulter, T. C.** (1973). Innervation of the vibrissae of the California sea lion, *Zalophus californianus*. *The Anatomical Record* **176**, 421-441.
- [148]. **Taylor, G. K. and Thomas, A. L.** (2002). Animal flight dynamics II. Longitudinal stability in flapping flight. *Journal of Theoretical Biology* **214**, 351-370.

- [149]. **Thomas, A. L. and Taylor, G. K.** (2001). Animal flight dynamics I. Stability in gliding flight. *Journal of Theoretical Biology* **212**, 399-424.
- [150]. **Towal, R. B., Quist, B. W., Gopal, V., Solomon, J. H. and Hartmann, M. J. Z.** (2011). The morphology of the rat vibrissal array: A model for quantifying spatiotemporal patterns of whisker-object contact. *Plos Computational Biology* **7**, e1001120.
- [151]. **Uchida, N. and Mainen, Z. F.** (2003). Speed and accuracy of olfactory discrimination in the rat. *Nature Neuroscience* **6**, 1224-1229.
- [152]. **van Breugel, F. and Dickinson, M. H.** (2014). Plume-tracking behavior of flying *Drosophila* emerges from a set of distinct sensory-motor reflexes. *Current Biology* **24**, 274-286.
- [153]. **Vickers, N. J.** (2000). Mechanisms of animal navigation in odor plumes. *Biological Bulletin* **198**, 203-212.
- [154]. **Vincent, S. B.** (1912). The function of the vibrissae in the behavior of the white rats. *Behavior Monographs* **1, 5**, 1-82.
- [155]. **Wallach, A., Bagdasarian, K. and Ahissar, E.** (2016). On-going computation of whisking phase by mechanoreceptors. *Nature Neuroscience* **19**, 487-493.
- [156]. **Webster, D. R. and Weissburg, M. J.** (2001). Chemosensory guidance cues in a turbulent chemical odor plume. *Limnology and Oceanography* **46**, 1034-1047.
- [157]. **Weissburg, M. J.** (2000). The fluid dynamical context of chemosensory behavior. *Biological Bulletin* **198**, 188-202.
- [158]. **Welker, W. I.** (1964). Analysis of sniffing of the albino rat. *Behaviour*, 223-244.

- [159]. **Wieskotten, S., Mauck, B., Miersch, L., Dehnhardt, G. and Hanke, W.** (2011). Hydrodynamic discrimination of wakes caused by objects of different size or shape in a harbour seal (*Phoca vitulina*). *Journal of Experimental Biology* **214**, 1922-1930.
- [160]. **Williams, C. M. and Kramer, E. M.** (2010). The advantages of a tapered whisker. *Plos One* **5**, e8806.
- [161]. **Williamson, C. H. K. and Govardhan, R.** (2004). Vortex-induced vibrations. *Annual Review of Fluid Mechanics* **36**, 413-455.
- [162]. **Witte, M., Hanke, W., Wieskotten, S., Miersch, L., Brede, M., Dehnhardt, G. and Leder, A.** (2012). On the wake flow dynamics behind harbor seal vibrissae - A fluid mechanical explanation for an extraordinary capability. Berlin Heidelberg: Springer-Verlag.
- [163]. **Wolfe, J., Hill, D. N., Pahlavan, S., Drew, P. J., Kleinfeld, D. and Feldman, D. E.** (2008a). Texture coding in the rat whisker system: Slip-stick versus differential resonance. *Plos Biology* **6**, 1161-1177.
- [164]. **Wolfe, J., Hill, D. N., Pahlavan, S., Drew, P. J., Kleinfeld, D. and Feldman, D. E.** (2008b). Texture coding in the rat whisker system: Slip-stick versus differential resonance. *Plos Biology* **6**, 1661-1677.
- [165]. **Yan, W. Y., Kan, Q. H., Kergrene, K., Kang, G. Z., Feng, X. Q. and Rajan, R.** (2013). A truncated conical beam model for analysis of the vibration of rat whiskers. *Journal of Biomechanics* **46**, 1987-1995.
- [166]. **Yilmaz, M. and Meister, M.** (2013). Rapid innate defensive responses of mice to looming visual stimuli. *Current Biology* **23**, 2011-2015.

- [167]. Yu, Y. S. W., Graff, M. M., Bresee, C. S., Man, Y. B. and Hartmann, M. J. Z. (2016a). Whiskers aid anemotaxis in rats. *Science Advances* 2, e1600716.
- [168]. **Yu, Y. S. W., Graff, M. M. and Hartmann, M. J. Z.** (2016b). Mechanical responses of rat vibrissae to airflow. *Journal of Experimental Biology* **219**, 937-948.
- [169]. **Zimmer, R. K. and Butman, C. A.** (2000). Chemical signaling processes in the marine environment. *Biological Bulletin* **198**, 168-187.
- [170]. **Zimmerfaust, R. K., Finelli, C. M., Pentcheff, N. D. and Wethey, D. S.** (1995). Odor plumes and animal navigation in turbulent water flow - a field study. *Biological Bulletin* **188**, 111-116.

Appendices

Supplemental information for Chapter 2

Table S2.1 Descriptive statistics for locomotion. No significant changes by group were observed in locomotor speed, number of pauses, or duration of pauses as the rats traversed the arena before and after whisker removal. A 0.075 m/s lower bound was imposed to exclude pauses from the locomotor speed analysis. Similarly, the minimum measurable duration of 50 ms (determined by the camera frame rate) imposed a *de facto* lower bound for the pause duration analysis.

	Group	Min.	Lower quartile	Median	Upper quartile	Max.	Skewness	Kurtosis
Locomotor speed (m/s)								
Before removal	Airflow	0.075	0.3450	0.8583	1.5405	5.3155	1.0428	3.6063
	Light	0.075	0.2510	0.7450	1.4405	5.2457	1.1565	3.8733
After removal	Airflow	0.075	0.3593	0.8347	1.4753	4.5891	1.052	3.6672
	Light	0.075	0.2454	0.6957	1.3971	4.8058	1.2167	4.0061
Number of pauses								
Before removal	Airflow	1	9	20	34	48	0.3868	1.8570
	Light	7	18	23.5	44	52	0.2166	1.6614
After removal	Airflow	3	8	12.5	36	48	0.5863	1.6860
	Light	16	21	32	46	57	0.3588	1.8714
Duration of pauses (s)								
Before removal	Airflow	0.05	0.25	0.55	1.10	18.1	5.1178	47.8660
	Light	0.05	0.4	0.75	1.5	29.7	6.5809	72.5227
After removal	Airflow	0.05	0.3	0.55	1.1	19.95	6.5353	64.3533
	Light	0.05	0.3	0.65	1.55	32.55	5.9915	61.8888

Table S2.2 Median values of the performance and deviation data. The Wilcoxon rank-sum test checks for differences in the median values. The trends in seen in the median values are similar to those expressed by the mean values shown in Figs. 2.5A and 2.6B.

Median performance values (%)		
	Before vibrissal removal	After vibrissal removal
Rat 1	61.17	60.98
Rat 2	67.44	46.50
Rat 3	62.50	55.60
Rat 4	56.32	46.02
Rat 5	57.67	43.18
Rat 6	82.68	79.33
Rat 7	72.08	69.60
Rat 8	82.89	84.87
Median deviation values (cm)		
	Before vibrissal removal	After vibrissal removal
Rat 1	111.31	119.37
Rat 2	106.31	133.73
Rat 3	101.17	126.54
Rat 4	106.09	126.01
Rat 5	133.91	147.76
Rat 6	145.41	170.81
Rat 7	116.09	125.71
Rat 8	139.04	100.84

Table S2.3 Completion criteria for the localization threshold experiment vary by rat. For rat 2, only the shaded (red) days were used in the analysis.

Rat 1				
	Before vibrissal removal		After vibrissal removal	
Day	Number of reversals at 10% + number of reversals at 2%	Total number of trials	Number of reversals at 10% + number of reversals at 2%	Total number of trials
1	6+7	93	6+6	66
2	6+3	106	6+6	67
3	6+5	64	6+6	63
4	6+6	87	6+6	72
5	6+6	87	6+5	93
6	6+6	76	6+5	83
Rat 2				
	Before vibrissal removal		After vibrissal removal	
Day	Number of reversals at 10% + number of reversals at 2%	Total number of trials	Number of reversals at 10% + number of reversals at 2%	Total number of trials
1	6+3	61	6+6	50
2	6+7	68	6+5	82
3	6+5	88	2+0	25
4	5+0	47	6+5	80
5	6+6	63	6+4	75
6	6+0	57	6+7	78
7	6+7	69	3+0	35
8	6+6	61	2+0	41
9	6+1	64	6+6	69
10	6+6	54	6+1	91
Rat 3				
	Before vibrissal removal		After vibrissal removal	
Day	Number of reversals at 10% + number of reversals at 2%	Total number of trials	Number of reversals at 10% + number of reversals at 2%	Total number of trials
1	6+6	64	6+6	87
2	6+6	82	6+6	63
3	6+6	92	6+6	96
4	6+6	67	6+6	82
5	6+6	93	6+6	101
6	6+6	81	6+6	80

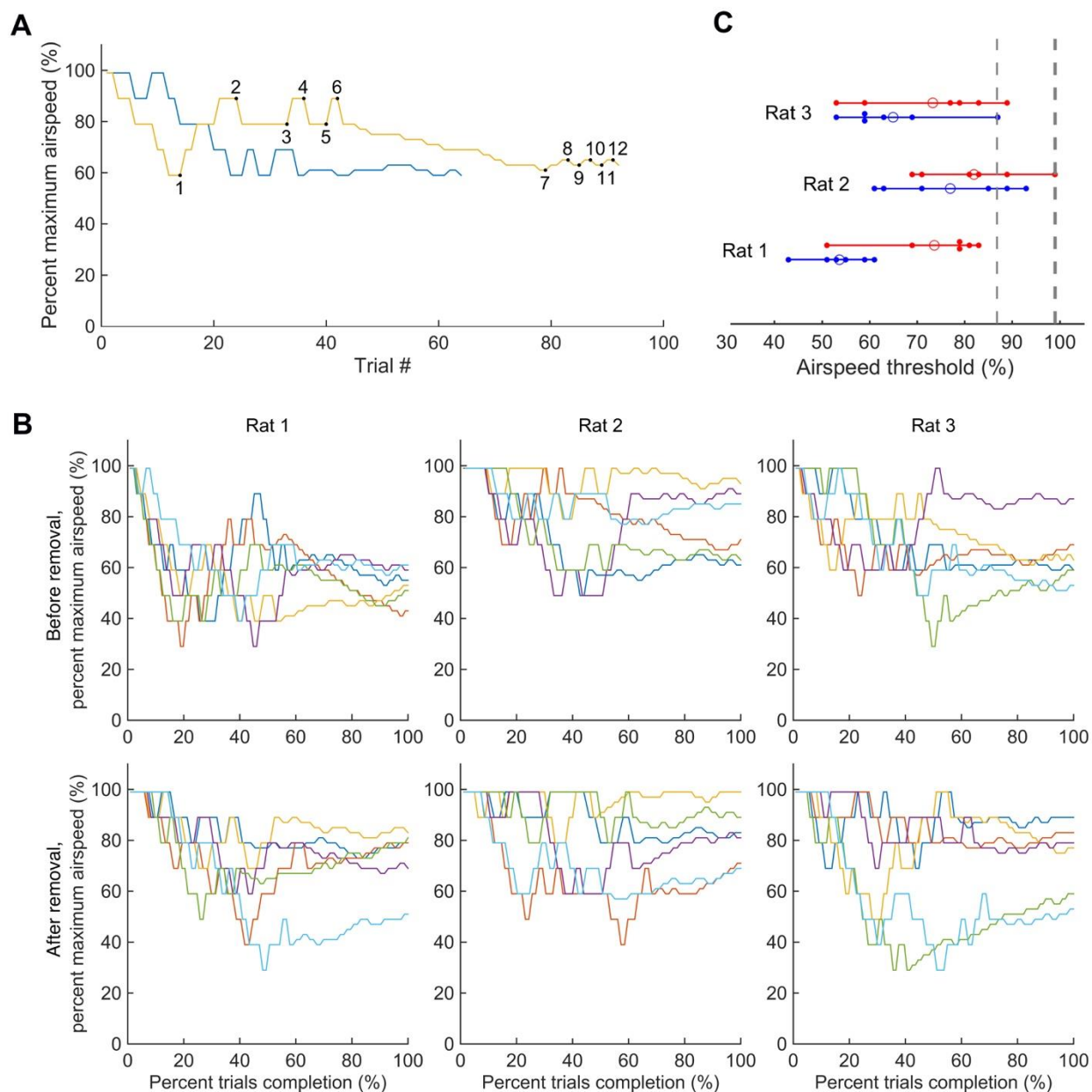


Figure S2.1 Fan speed was adjusted to determine rat localization thresholds. **(A)** Two days of typical performance of Rat 3 on the 2-up/2-down threshold experiment. Reversals for one day are labeled (black dots). Percent of maximum fan speed is shown as a function of trial number. **(B)** Performances of Rats 1, 2, and 3 six days before and six days after vibrissal removal are shown. Percent of maximum fan speed is shown as a function of percent trial completed. Days used are listed in Table S2.3. Sequential days are color coded: blue; red; yellow; purple; green; cyan. **(C)** Airspeed threshold of Rats 1, 2, and 3 six days before (blue dots) and six days after (red dots) vibrissae removal. Circles indicate mean airspeed thresholds before (blue) and after (red) vibrissae removal. Airspeed (87%) used in the original experiment and the maximum value (99%) of

airspeed are highlighted in gray dashed line. Wilcoxon rank sum test results indicate that airspeed threshold before is significantly lower than after vibrissae removal for Rat 1 ($p=0.03$).

Movie S2.1 The video shows thirteen trials in which a rat localizes airflow emanating from one of five fans, arranged around the circumference of a table. The trials are not sequential; they were chosen to give examples of typical behaviors. All trials are from the same rat on the same day. The left video shows the view obtained from the overhead camera (20 fps). The activated fan is labeled “ON.” The right video shows an interpolated airspeed colormap projected onto the table, with the trajectory of the tracked rat overlaid. Airspeed is in m/s.

Supplemental information for Chapter 3

Movie S3.1 Response of the E2 whisker response to airflow at 2.3 m/s. The whisker is oriented 45° relative to the airflow. The video plays ten times slower than real time.